Investigation of biomarker-targeted SERS nanoparticles for multiplexed molecular imaging of fresh tissue specimens

Soyoung Kang

A dissertation
submitted in partial fulfillment of the
requirements for the degree of

Doctor of Philosophy

University of Washington
2018

Reading Committee:

Jonathan T.C. Liu, Chair
Eric J. Seibel
Kenneth M. Tichauer

Program authorized to offer degree:
Mechanical Engineering

UNIVERSITY OF WASHINGTON

Abstract

Investigation of biomarker-targeted SERS nanoparticles for multiplexed molecular imaging of fresh tissue specimens

by Soyoung KANG

Chair of the Supervisory Committee:

Jonathan T.C. Liu

Mechanical Engineering

Biomarker-targeted surface-enhanced Raman scattering (SERS) nanoparticles (NPs) have been explored as a viable option for targeting and imaging multiple cell-surface protein biomarkers of cancer. A previously-developed Raman-encoded molecular imaging (REMI) technique utilizes such targeted NPs for topical application onto excised tissues to enable rapid visualization of a multiplexed panel of cell surface biomarkers at surgical margin surfaces. While it has been demonstrated that REMI may potentially be used to guide tumor-resection procedures, the strategy would benefit from improvements described in this thesis. First, an investigation into channel-compressed spectrometry revealed that up to 64 times fewer spectral channels may be used to accurately demultiplex up to five SERS NP flavors (compared to our previous methods). This strategy offers the potential for improved imaging speed and/or detection sensitivity with a low-channel count detector in future REMI systems. Next, the complexities in nonspecific accumulation, diffusion, and chemical binding of targeted NPs in fresh tissues were explored in a microscopic investigation quantifying the specific vs. nonspecific accumulation of topically-applied NPs as they diffuse into fresh tissue. The findings from this study led us to hypothesize and later demonstrate that by reducing NP diffusion, nonspecific accumulations of NPs in tissue is reduced, thereby allowing for molecular imaging of fresh tissue surfaces with higher NP ratios (targeted vs. untargeted), and that the staining can be achieved more rapidly than before (6-min topical application). A third, and final, study is presented, to help establish optimized protocols for the staining and rinsing of

fresh tissue specimens for REMI using a mathematical model that incorporates multi-layer diffusion in addition to binding and nonspecific retention compartments. The goal of this final study is for this forward model to ultimately be used to enable quantitative methods of evaluating molecular expression, which could enable improved assessments of tumor margins (*e.g.*, the use of multi-stage staining/rinsing processes to allow kinetic model fitting of data). In summary, the first two studies enable the design of more rapid molecular imaging systems, and NP agents with improved sensitivity and contrast, respectively, for rapid molecular imaging of fresh tissues suitable for intraoperative clinical settings. The mathematical model study is valuable for accurately quantifying biomarker expression levels to potentially increase the sensitivity and specificity of tumor detection at surgical margins.

Acknowledgements

I would like to express the deepest gratitude to all those that have provided support and guidance throughout my Ph.D. First, I would like to thank my advisor, Professor Jonathan Liu, for the patience and time that he devotes to carefully training each of his students. I am grateful for his mentorship, being a role model, and the opportunities in education and professional development he has provided. I would also like to thank the members of my thesis committee, Professors Kenneth Tichauer, Eric Seibel, and Ruikang Wang, not only for their insightful comments and encouragement, but also for their challenging questions that motivated me to consider my research from various perspectives. I would like to acknowledge the roles of Professors Liu and Seibel outside my thesis committee, as members of the Engineering Innovation in Health teaching team, along with Professor Jonathan Posner. As a teaching assistant for this outstanding team the past two years, I have been exposed to the tremendous and exciting role of teaching engineering innovation in healthcare and medicine. I am grateful for the support, mentorship, and opportunities that this teaching team has provided.

My time in Seattle was made enjoyable in large part due to the many friends that became a part of my life. I would like to thank the students and post-docs in the Molecular Biophotonics Lab, fellow officers in the Mechanical Engineering Graduate Student Association, and the wonderful staff in the Mechanical Engineering department, all of whom provided moral and emotional support through numerous lengthy and often failed experiments, indulged me with longer coffee breaks than is appropriate, shared countless meals over stimulating conversations, and altogether made coming to UW everyday an exciting and joyful occasion. I am especially grateful to Dr. Yu "Winston" Wang, who carefully trained me in experimental methods and mentored me throughout my Ph.D.

Finally, none of this would have been possible without the love and support of my family. I am fortunate to have such warm and encouraging parents whose only concern is that I do what makes me happy, which is asking hard questions and solving hard problems. I am grateful for my brother, who taught me to be fearless; for my dad, who challenged me to ask the tough questions; and for my mom, for everything. And lastly, I would like to thank Martin, for challenging me, for encouraging me, and for believing in me.

Contents

List of Figures

List of Tables

Chapter 1

Introduction

1.1 Clinical problem

Approximately 200,000 patients are diagnosed with early-stage breast carcinoma each year in the United States, for which breastconserving surgery (*a.k.a.* partial mastectomy or lumpectomy) is a standard intervention [1]. Unfortunately, amongst various institutions, between 20% and 50% of these patients require additional surgery if post-operative histology reveals that the resection margins, which are rolled in ink, are positive for carcinoma (Figure 1.1) [2]. In the past, the existence of a close margin, in which post-operative paraffin-embedded histology revealed the presence of tumor cells within 2 or 3 mm of the surgical margin surface (the "inked" surface), was often used as a criterion to warrant re-excision. However, recent studies and consensus guidelines advocate defining a negative margin as "no tumor at the inked surface" (*i.e.*, no tumor at the most superficial surface of the surgical excision), especially for invasive carcinoma [3]. Regardless of an institution's criterion for re-excision, there is no debate that the presence of any subtype of breast tumor at the surgical margin surface ("tumor on ink") is unacceptable and that there would be value in an intraoperative technology to comprehensively assess these surfaces for the presence of residual tumor at the final stages of lumpectomy.

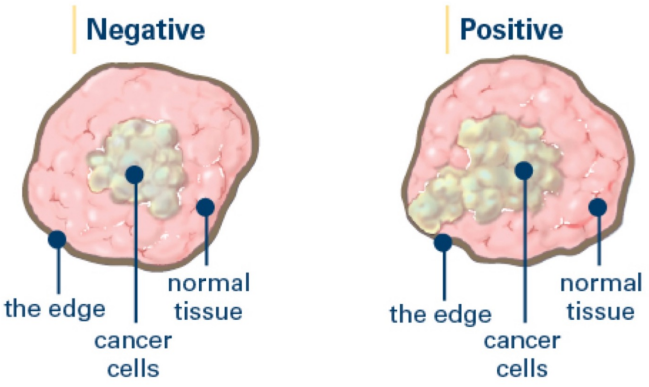

FIGURE 1.1: The margin of an excised tissue specimen is said to be positive when the tumor cells are seen at the inked margin and negative when they are absent or present away from the "inked margin."

1.2 Current solutions

The current gold-standard for assessing surgical margins, post-operative formalin-fixed paraffin-embedded (FFPE) histology, suffers from long fixation and processing times (∼16 hr) and limited sampling of the inked margin (<1%). On the other hand, frozen-section analysis (FSA), a procedure in which small portions of resected tissue specimens are rapidly frozen, sectioned, and stained for microscopic evaluation during a surgical procedure, offers faster processing times (∼20 min per section), enabling intraoperative feedback and the potential to reduce re-excision surgeries. However, FSA prolongs surgical time and suffers from severe sampling errors since only small numbers of tissue sections (typically 5-μm thick) can be rapidly prepared on slides and visualized under a microscope. As a result, FSA can yield significant false-negative rates (*e.g.*, low sensitivities of <70% have been reported) [4, 5]. Moreover, FSA is particularly difficult to perform for breast tissues due to their high lipid content, and freezing artifacts make subsequent diagnosis on paraffin-embedded sections more difficult [6, 7].

Touch-prep cytology relies on the sloughing of tumor cells from the surgical margin, which are then collected on glass microscope slides for staining and microscopic evaluation [8]. As a point-sampling approach, comprehensive sampling of the surgical margin is difficult, and adherent or subsurface tumor cells are not identified. Furthermore, studies on touch-prep cytology have been inconsistent in demonstrating value for the intraoperative assessment of breast cancer margins [9, 10, 11, 12].

Intraoperative specimen X-ray imaging of lumpectomy specimens helps guide the surgeon in detecting grossly positive margins (*i.e.*, calcifications or tumor present at the radiographic margins) [13, 14]. However, specimen X-ray (as with mammography) is diagnostically inaccurate due to the inability to identify diffuse microscopic processes, especially where the tumor boundary is poorly-defined.

It is worth noting one commercial product recently made available for the intraoperative assessment of breast tumor margins: the MarginProbe® sold by Dune Medical Devices, Inc. This device uses RF spectroscopy to differentiate between tumor and normal tissues based on an "electromagnetic signature." This device contains a disposable probe ($1000 per probe) that is manually placed in contact with the tissue to interrogate an area with a diameter of 7 mm at an integration time of 1.5 sec. The large interrogation "spot size" of the device (7 mm) severely limits its sensitivity to detect smaller residual tumors. For example, if a residual tumor of 1 mm in diameter is encountered, each MarginProbe measurement provides a spatially averaged reading over a tissue area that is $7^2 = 49$ times larger than the tumor, which will result in extremely poor sensitivity to detect such small (but significant) tumors [15, 16, 17]. In addition, RF spectroscopy is sensitive to a number of biological alterations such as vascularity, membrane depolarization, cell-to-cell connectivity, and nuclear atypia. The ambiguous and complex nature of these electromagnetic signatures makes RF spectroscopy prone to false-positive readings (poor specificity) from benign conditions such as inflammation, hyperplasia, intraductal papillomas, fibrosis, and simple cysts.

The above discussion (summarized in Table 1.1) points to the fact that surgeons do not have adequate intra-operative assessment tools to accurately ensure that the cancer has been completely removed at the time of first surgery [18, 19]. This represents a significant unmet clinical need for rapid intraoperative margin assessment.

1.3 Optical imaging techniques for breast tumor margin assessment

Optical imaging of excised tissue margins is an attractive solution for screening for residual tumors because it is relatively fast and non-destructive. Table 1.2 provides a breakdown of the different optical tools in various stages of preclinical and/or clinical

TABLE 1.1: Existing breast tissue margin assessment techniques. *Note that the reported sensitivity and specificity listed in the table are not entirely representative of the accuracy of the imaging technique, as these values depend on the study design, including the type and number of specimens examined, which may vary significantly from one study to another.

Technology	Advantage(s)	Disadvantage(s)	*Sens. & Spec.	Ref(s)
Frozen-section analysis (FSA)	• ~20-min per section	• Significant false-negative rates since only a small number of thin sections evaluated • Difficult to perform on fatty breast tissue • Freezing artifacts compromise post-operative pathology	<70% sens., 99.6% spec.	[6,7]
Touch-prep cytology	• Evaluation of whole specimen surface	• Requires cytologist expertise • Comprehensive sampling of the surgical margin is difficult	38-100% sens., 83-100% spec.	[9-12]
MarginProbe	• Real-time assessment with a handheld probe	• Limited sensitivity due to large spot size (7 mm) • Prone to false-positive readings from benign conditions (inflammation, hyperplasia, cysts, etc.)	71% sens., 68% spec.	[15-17]
Intraoperative specimen X-ray imaging	• Rapidly detecting grossly positive margins (*e.g.* calcifications)	• Inability to identify small tumor regions at the tissue surface	47-72% sens., 52-75% spec.	[13-14]

development that have been reported for *ex vivo* assessment of excised breast tissue surfaces for residual cancer, and are described in further detail below.

1.3.1 Microscopy

Optical-sectioning (rejection of out-of-focus light) microscopy techniques, such as confocal microscopy and nonlinear microscopy, can obtain high-resolution and high-contrast images of freshly resected tissues [20, 21, 22, 23, 24, 25, 26]. Confocal mosaicing microscopy is a method to obtain pathology-like microscopic images over large fields-of-view with freshly resected tissues, either in reflectance mode [27, 28, 20, 26] or in fluorescence mode through the topical application of passive or targeted fluorophores [29, 30, 31, 32]. Nonlinear (*i.e.* multiphoton, harmonic generation, autofluorescence lifetime, coherent anti-Stokes Raman scattering - CARS, stimulated Raman scattering - SRS) microscopy enables high-resolution imaging in optically scattering tissues with improved imaging depths over fluorescence and confocal microscopy [33, 34, 35, 23, 24, 25]. However, applying these techniques for intraoperative imaging of large tissue surfaces is challenging

due to the relatively slow speed of these point-by-point imaging techniques. In addition, these techniques suffer from an extremely limited depth-of-focus, necessitating labor-intensive and time-consuming tissue-flattening or volumetric imaging strategies to visualize a large tissue surface with topological irregularities [20, 23].

Camera-based optical-sectioning microscopy techniques, such as microscopy with UV surface excitation (MUSE) [36, 37, 38, 39] and structured illumination microscopy (SIM) [40, 41] are advantageous for clinical applications due to their faster imaging speeds and reduced complexity, but are not intended for deep volumetric microscopy. For example, MUSE relies on the limited penetration depth of UV light to obtain a selective image of the tissue surface, thereby precluding subsurface imaging. SIM illuminates tissue surfaces with a high-frequency spatial pattern that is only well-resolved at the focal plane of the microscope. Therefore, the out-of-focus background light (primarily lower spatial frequencies) may be computationally removed. Since the background light is not physically blocked from the detector, contrast and imaging depth is limited due to limitations in detector dynamic range and the large amount of shot noise introduced by the background light [42, 43].

Finally, light-sheet microscopy has been demonstrated for volumetric imaging of fresh slices of breast tissue immersed in silicone oil [44, 45, 46]. This method acheives optical sectioning by using a thin 'selective' illumination plane, which generates fluorescence signal that is imaged in the orthogonal direction. However, with the image detection plane being oriented at 45-deg relative to the specimen surface, extracting images of the tissue surface requires the collection and processing of a significantly large amount of data that is computationally intensive, especially compared to *en face* approaches.

1.3.2 Deeper microscopy

Absorption- and reflectance-based microscopy approaches, such as photoacoustic microscopy (PAM) and optical coherence tomography (OCT), take advantage of the intrinsic optical contrast of breast tissue to enable label-free imaging to a depth of up to 2 mm [47, 48, 49, 50, 51, 52, 53, 54, 55]. Synergistically combining light and sound, PAM delivers a pulsed laser beam into the tissue to generate ultrasonic waves, which are then detected with a focused ultrasonic transducer. However, to acquire a single image requires raster scanning of a tightly focused laser beam in three dimensions and could

take several hours to obtain, which is not feasible for use in an intraoperative setting. OCT is referred to as the optical counterpart of ultrasound because of the similarity of the acquired grayscale images, but uses light instead of sound to extract sub-surface information. While OCT has been successfully translated into clinical settings for label-free imaging of human tissues [53, 54, 52, 55], it is not typically designed to achieve sub-cellular resolution and is not suited for probing multiplexed and molecular targets as desired for standard-of-care clinical pathology.

1.3.3 Spectra-based imaging approaches

Spectroscopic methods reveal the relative concentrations of chemical constituents such as hydrocarbons, lipids, nucleic acids, and/or the size distribution of photon-scattering objects in tissues based on intrinsic Raman [56, 57, 58] or reflectance [59, 60]. While high sensitivities and/or specificities have been reported, these methods are limited to performing single point measurements and would require numerous sequential spot measurements to evaluate the entire tumor surface, making the procedure time-consuming and laborious, especially ones that are as large as 10-20 cm^2 in a timeframe suitable for intraoperative margin assessment.

1.3.4 Other wide-area and multimodal optical imaging

Recently, several groups have been developing technologies for wide-area optical imaging of tissued surfaces [59, 61, 62, 63]. Kong et al. developed an integrated optical technique that utilizes automated segmentation of autofluorescence images to select and prioritize the sampling points for point-based Raman spectroscopy to achieve high sensitivity and specificity [62]. Bydlon et al. and Brown et al. utilized quantitative diffuse reflectance spectral imaging to determine contrast in entire breast tissue specimens based on chemical constituents [59, 61]. Recently, Thomas et al. demonstrated the feasibility of Raman spectroscopy using a 3-dimensional scanner to assess the entire margins of resected specimens within a clinically feasible time [63]. However, the ability to image the expression of molecular biomarkers, which plays a prominent role in recent advances in precision medicine [64, 65], would offer complementary information that could further improve the sensitivity and specificity of detection.

TABLE 1.2: A list of reported *ex vivo* optical imaging techniques in various stages of preclinical and/or clinical development for assessing margins of resected breast tissue for residual cancer. *Note that the reported sensitivity and specificity listed in the table are not entirely representative of the accuracy of the imaging technique, as these values depend on the study design, including the type and number of specimens examined, which may vary significantly from one study to another.

Type	Technique	Contrast	Resolution (Low) mm (High) µm	Speed (Low) hr/cm² min/cm² (High) sec/cm²	Depth (Superficial) N/A µm (Deep) mm	Complexity/cost (Complex/$$$) (Simple/$)	Notes	*Sens./ Spec.	Ref(s).
Microscopy	**Confocal microscopy**	Fluorescent labels, label-free reflectance					Multiplexing capability with fluorescent contrast agents	91-93% / 93%	[20-22, 26, 29-32]
	Nonlinear microscopy	Mostly label-free					Multiphoton, harmonic generation, autofluorescence lifetime, CARS, SRS, etc.	90-95% / 93-94%	[23,-26, 33-35]
	Structured illumination microscopy (SIM)	Fluorescent labels					Multiplexing capability with fluorescent contrast agents	-	[36-39]
	Microscopy with UV surface excitation (MUSE)	Fluorescent labels					Multiplexing capability with fluorescent contrast agents	-	[40-41]
	Light-sheet microscopy (LSM)	Fluorescent labels					Multiplexing capability with fluorescent contrast agents	-	[44-46]
Deeper microscopy	**Photoacoustic microscopy (PAM)**	Label-free absorption					Limited contrast-agent options	-	[47-50]
	Optical coherence tomography (OCT)	Label-free reflectance					Limited contrast-agent options	55-100% / 68-82%	[51-55]
Spectra-based imaging	**Intrinsic Raman spectroscopy (RS)**	Label-free inelastic scattering					Spectral info has ambiguous connection to biological or histological info	93-7% / 85-100%	[56-58, 63]
	Diffuse reflectance spectroscopy (DRS)	Label-free diffuse scattering						74-89% / 67-86%	[59-61]
	Raman-encoded molecular imaging (REMI)	Biomarker-targeted SERS NPs					Multiplexed molecular imaging with biomarker-targeted SERS NPs	89.3% / 92%	[83-86, 92-93, 125]

1.4 Benefits of molecular imaging approaches

Over the past few decades, there has been increasing confidence in the presumption that molecular imaging approaches – namely, the imaging of protein biomarkers of cancer – can identify tumors with a high degree of sensitivity (true positive rate) and specificity (true negative rate) [66]. High specificity would be valuable for intraoperative cancer detection to minimize over-excision and to optimize patient cosmesis (a major goal of breast-conserving surgeries). However, in order to achieve high detection *sensitivity*, multiple biomarkers should be evaluated since the molecular profiles of most cancers, including breast carcinoma, vary greatly between patients as well as spatially and temporally within a single tumor mass [67, 68]. Most optical molecular imaging systems have utilized small-molecule fluorescent contrast agents, but there has been recent interest in both fluorescent and Raman nanoparticle (NP) contrast agents as well, as described next.

1.4.1 Optical molecular contrast agents

Numerous molecular probes are being developed to label disease biomarkers [69, 70, 66, 71, 72, 73], however, their utility for cancer detection is often limited by various factors. For example, conventional small-molecule fluorescent dyes are easily photobleached, have a wide emission spectrum, and must often be excited at disparate wavelengths when combined, thus limiting their multiplexing capability [74]. Nanoparticle quantum dots (QDs) offer a narrower emission bandwidth, higher sensitivity and higher photostability than fluorescent dyes [75], and have been used for multiplexed imaging of 3-5 biomarkers in breast cancer cells and formalin-fixed tissue sections [76]. However, their potential toxicity has thus far precluded their *in vivo* use in humans and no clinical studies have been reported to evaluate the efficacy of QD-based imaging technologies for guiding lumpectomy. Recently, surface-enhanced Raman scattering (SERS) NPs have attracted interest due to their excellent multiplexing capability [77, 72]. These SERS NPs are available in many "flavors," each of which emits a characteristic Raman fingerprint spectrum when illuminated at a common wavelength [78, 79]. By functionalizing various flavors of SERS NPs with different targeting moieties (*i.e.*, antibodies, oligonucleotides, aptamers, peptides, and other small molecules), the NPs can be multiplexed to simultaneously target and image a large panel of protein biomarkers [80, 81, 82, 83].

1.5 Introduction to Raman-encoded molecular imaging (REMI)

We have recently demonstrated that a Raman-encoded molecular imaging (REMI) technique, which utilizes the topical application of multiplexed SERS NPs, enables the rapid visualization of multiple cell-surface biomarkers at the surfaces of fresh tissues [84, 83, 85, 86]. In our REMI approach, toxicity and sterility concerns are circumvented by staining and imaging fresh surgical specimens *ex vivo*, with the potential to allow for expedited regulatory approval and rapid clinical translation. A critical component of REMI is the use of a ratiometric imaging strategy that enables accurate quantification of biomarker expression levels by utilizing one untargeted NP flavor to normalize for the nonspecific accumulation exhibited by all NPs (including both targeted and untargeted NPs), as for example due to off-target binding, uneven topical delivery and washout, and variations in tissue permeability and retention [87, 88, 89, 90, 91, 92, 93]. The SERS NPs used for REMI are particularly well-suited for accurate ratiometric quantification due to the fact that they are all excited at a single wavelength (785 nm) and emit Raman spectra within the same narrow spectral range (approximately 850–900 nm), which ensures that all NPs are irradiated identically and are affected by the same tissue optical properties.

Figure 1.2 shows a schematic of REMI for intraoperative use. In a clinical implementation of REMI, freshly resected human breast tissues from lumpectomy procedures are immediately transferred to a pathology suite for intraoperative consultation. Each specimen is topically stained with a mixture of SERS NPs (multiple biomarker-targeted NPs and at least one untargeted control NP), followed by spectroscopic imaging of the surgical margin surface. The acquired SERS spectra are demultiplexed to determine the ratio of the targeted vs. untargeted NPs, which enables the quantification of various biomarker targets (*e.g.* EGFR, HER2, ER, CD44, etc.). REMI images of the individual biomarkers are combined to detect the presence of residual tumors at the surgical margin surfaces of the specimens. In terms of clinical translation, it is important to note that the application of bioconjugated SERS NPs does not interfere with downstream IHC, and that the standard post-operative histopathology can still be performed on tissues after intraoperative REMI imaging. Consequently, REMI is not required to be a gold-standard diagnostic technique. Rather, the purpose of REMI is to greatly reduce the number of re-excision surgeries for breast cancer lumpectomy patients by helping

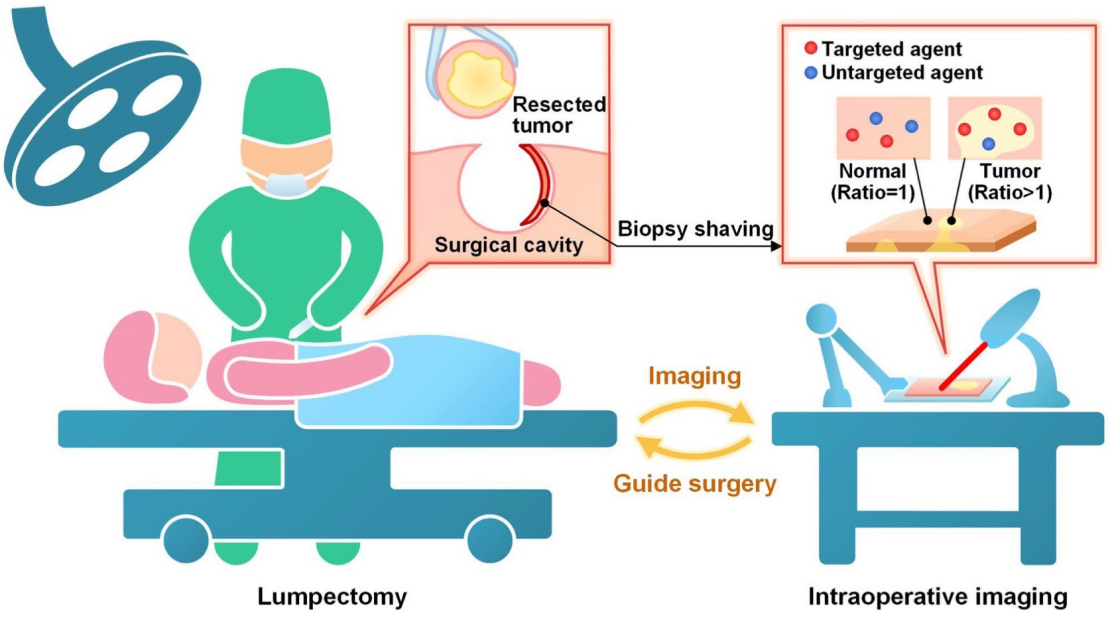

FIGURE 1.2: **Schematic of an intraoperative imaging technique (*e.g.*, REMI) to rapidly identify residual tumors at the margins of freshly resected tissues for guiding breast-conserving surgeries.** A ratiometric strategy (right inset) quantifies biomarker expression by comparing the signal from targeted NPs and untargeted NPs. This figure was originally published in [85].

surgeons to intraoperatively identify surgical margins that are positive for carcinoma in which there is an unequivocal need for additional resection. Conventional post-operative pathologic examination of tissue may still be performed as a gold standard to identify microscopic tumor burden or close margins (for institutions that continue to maintain a conservative criterion for re-excision).

While it has been demonstrated that REMI may potentially be used to guide tumor-resection procedures, there are clear opportunities to further improve the strategy for clinical translation (*e.g.*, speed, accuracy, imaging contrast, biomarker detection sensitivity, and quantitative analysis). Chapter 2 of this thesis (a) delves into the background information on the REMI technique, (b) provides detailed experimental methods and previously-published results, and (c) concludes with a discussion of limitations and technical needs of the REMI technique, which provides a framework for the thesis. Chapters 3, 4, and 5 explore ways to overcome the limitations described in Chapter 2. This thesis culminates in the future work proposed in Chapter 6.

Chapter 2

Background

In this chapter, a more detailed description of the Raman-encoded molecular imaging (REMI) technology is provided (section 2.1), followed by the experimental methods (section 2.2) and some experimental results from previously-published work (section 2.3). This chapter will conclude by describing some limitations and challenges of the REMI technology (section 2.4), which provides a framework for the remainder of this thesis.

2.1 Principles of Raman-encoded molecular imaging (REMI)

2.1.1 Surface-enhanced Raman scattering nanoparticles (SERS NPs)

The Raman scattering signal of molecules can be enhanced by more than ten orders of magnitude when adsorbed on metal nanostructures due to the excitation of localized surface plasmons [94, 95]. Based on this effect, SERS NPs have been developed since the late 1990s, acting as extrinsic Raman labels for the optical detection of biomolecules [96, 97, 98, 99, 100, 101, 102, 103]. Typical SERS NPs have a sandwich structure: a layer of Raman reporter molecules is permanently adsorbed onto the surface of a metal core to trigger the SERS effect, generating a characteristic Raman spectrum upon laser excitation at a specified wavelength. This characteristic SERS spectrum serves as a barcode or fingerprint for the identification of that particular "flavor" of NP, where different flavors of SERS NPs utilize different reporter molecules to generate specific

spectral signatures. A biocompatible coating is generally used to surround the NP core and to stabilize the SERS NP signal, such that the SERS spectrum is constant for each NP flavor and is not influenced by the surrounding environment. For biomolecule detection, SERS NPs can be conjugated to a molecule such as an antibody or affibody to a specifically target a biomolecule of interest [104, 88, 105, 93].

2.1.2 Topical application and challenges motivates ratiometric strategy

The topical administration of such targeted SERS NPs has been extensively employed to image the expression of protein biomarkers at the surface of *ex vivo* animal tissues and resected human tissues [106, 88, 107, 92, 93, 79]. A key advantage of topical application, for eventual clinical translation, is that toxicity issues are reduced, especially since the large size of the SERS NPs (120-nm in diameter) inhibits the penetration of topically applied NPs through deep tissue [108]. It should be noted that the topical staining of real tissues using SERS NPs is more challenging than the topical staining of cultured cell lines due to considerable nonspecific accumulation in tissues as well as reduced access to cell-surface targets (compared to cultured cells in a dish). Therefore, it is important to optimize targeted SERS NPs to exhibit extremely high binding affinity/avidity to receptor-positive cell lines before tackling the greater challenge of detecting biomarkers in tissues.

We have found that adding 1% BSA to the NP staining solution can reduce the nonspecific accumulation of NPs within tissues [85]. However, nonspecific accumulation is still high and can be extremely variable due to non-uniform tissue structures. In addition, uneven NP delivery/rinse removal at different tissue locations often results in misleading imaging contrast [92, 93]. One method that has been utilized to mitigate these nonspecific effects, and to accurately visualize the molecularly specific accumulation of NP concentrations is to introduce an untargeted (control) NP flavor simultaneously with the targeted NP during imaging experiments in order to normalize for nonspecific effects. This method allows one to calculate the ratio of biomarker-specific NP accumulation exhibited by targeted NPs alone versus the nonspecific accumulation exhibited by all NPs, as revealed by the control NP.

For tumor imaging, the topical application of biomarker-targeted and untargeted control NPs onto tissues, followed by the rinse removal of unbound NPs has been shown to yield molecular imaging contrast between tumor and normal tissues in 5–60 min [104, 107, 93]. The efficient washout of unbound NPs is key to maximizing the contrast between tumor and normal tissue regions. Note that since SERS NPs typically are not internalized by cells during the short incubation times utilized in our experiments ($<$ 1-hr), SERS NPs are generally limited to the targeting of exposed cell-surface receptors.

2.1.3 Raman imaging system

Raman spectroscopy is typically performed by collecting a spectrum from an area that is illuminated at a precise wavelength in order to determine the relative concentration of various molecules or chemical constituents (*e.g.*, hydrocarbons, nucleic acids, etc.) of interest within the illuminated area. The size of the illumination spot therefore determines the spatial resolution of detection. Although commercial or custom Raman microscopes have been employed to image tissues at micron-level spatial resolution [69, 105], a sub-millimeter- or millimeter-level resolution is preferred for imaging (scanning) a large tissue area [78, 106, 92] due to the relatively long acquisition times required for Raman imaging (typically 1–100 sec for unenhanced Raman spectroscopy and 1–100 ms for surface-enhanced Raman scattered spectroscopy). Furtheremore, the detection of sub-millimeter-sized tumors is considered to be an acceptable size threshold for many clinical applications such as early cancer detection and surgical guidance.

A standard optical system for macroscopic-resolution ($>$100-μm spatial resolution) imaging of SERS NPs includes an imaging probe and a spectrometer [106, 109, 93, 79]. The light source is typically a NIR laser, which is delivered to the sample through a fiber-optic probe. The optical signals (*e.g.*, reflectance, scattering, and fluorescence) from the SERS NPs and tissue (background) are collected by multiple fibers in the imaging probe and are delivered through a fiber bundle to a spectrometer, where the collected light is dispersed by a diffraction grating onto a spectroscopic imaging array, such as a cooled deep-depletion CCD detector. In our macroscopic optical setup, the imaging probe remains fixed while the NP-stained specimen surface (surgical margin) is raster-scanned with a two-axis stage until the imaging of the entire specimen surface is complete.

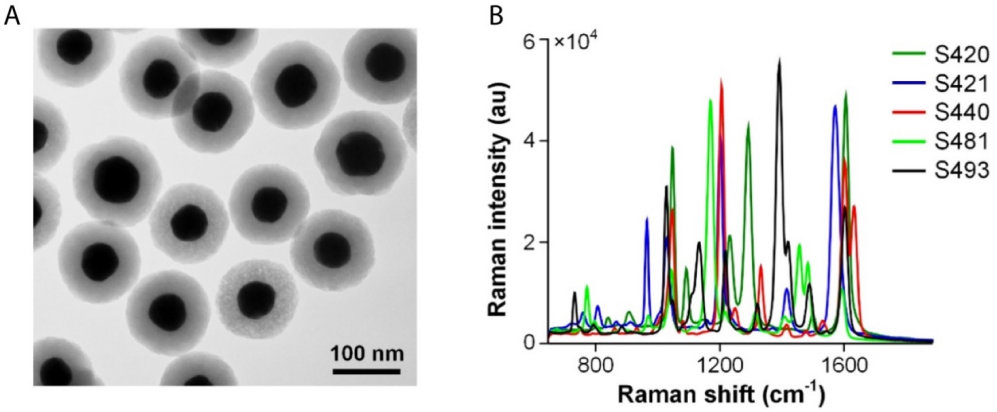

FIGURE 2.1: **Structure and spectra of SERS NPs.** (**A**) Transmission electron microscopy (TEM) image of SERS NPs. The gold core of the NP appears black, and is encapsulated by a silica shell that isolates the NP core from the environment, as well as from other NPs. This allows the SERS signal to be highly stable as a unique spectral fingerprint to identify each NP flavor. (**B**) The reference spectra of the five NP flavors used in our previous studies. This figure was originally published in the supplementary information of [86].

2.2 Materials and methods

2.2.1 Functionalization of SERS NPs

Commercial SERS NPs were purchased from BD (Becton, Dickinson and Company). These NPs consist of a 60-nm diameter gold core, a unique layer of Raman reporters adsorbed onto the surface of the gold cores, surrounded by a 60-nm thick silica coating, resulting in an overall diameter of ∼120-nm (Figure 2.1A). Previously we have used five "flavors" of NPs, identified as S420, S421, S440, S481, and S493, each of which emits a characteristic Raman spectrum due to chemical differences in the Raman reporter layer (Figure 2.1B).

The silica surface of the commercial NPs are functionalized with thiols to allow conjugation to a variety of targeting molecules (Figure 2.2A). Stock concentrations of SERS NPs (800 pM in water) were diluted in 10 mM MOPS (Sigma-Aldrich, part No. M1254) buffer, pH 7.25, at a volume ratio of 1:1 (*e.g.*, 200-μL buffer to 200-μL NPs in water), and then reacted with DyLight 650 Maleimide (Thermo Scientific, 62295), at 4.5×10^5 molar equivalents per NP, at room temperature for 1 hr to conjugate DyLight 650 fluorophores to the NP surface (Figure 2.2A). Two different monoclonal antibodies (mAb) targeting epidermal growth factor receptor (EGFR; Thermo Scientific, MS378PABX) or human epidermal growth factor receptor 2 (HER2; Thermo Scientific, MS229PABX)

were used to functionalize NPs. For studies imaging a larger panel of biomarkers, NPs were conjugated to additional targets: anti-CD44 (Abcam plc., ab6124) or anti-CD24 (Abcam plc., ab31622) mAbs. In addition, negative-control NPs were prepared by conjugating one NP flavor with an isotype control antibody (mouse IgG1; Thermo Scientific, MA110407). All mAbs were purchased free of protein stabilizers such as BSA or gelatin, and free of preservatives such as sodium azide. Antibodies were added to fluorescent NPs at 500 molar equivalents per NP, along with the heterobifunctional PEG cross linker $SM(PEG)_{12}$ (Thermo Scientific, 22112) at 1.5×10^4 molar equivalents per NP, and incubated at room temperature for 3 hr. Following the primary conjugation reaction, $MM(PEG)_{12}$ (Thermo Scientific, 22711) at 6×10^5 molar equivalents per NP, was then added to the NPs and reacted overnight at 4-deg C to block residual thiols on the NPs. Note that all reagents were degassed with dry argon gas prior to use and all reactions were conducted under anhydrous conditions in light-protected amber vials (Fisher Scientific, 03-391-36&03-391-17) on a vortex mixer (Fisher Scientific, Microplate Vortex Mixers, 02-216-101) set at 800 rpm. Finally, the NPs were reacted at room temperature with 2-mercaptoethanesulfonate (MESA; Sigma-Aldrich, M1511) for 30 min at 9×10^5 molar equivalents per NP, and the reaction mixture was then diluted at a volume ratio of 1:1 with storage buffer (20 mM MOPS at pH 7.5) containing 0.1% BSA (Jackson Immuno, 001-000-162) and 0.05% sodium azide (Sigma-Aldrich, S2002). The diluted reaction mixture was purified four times via centrifugation (1000 g for 10 min), in which the supernatant was removed and replaced with storage buffer after each round of centrifugation. The conjugated NPs were stored at 4-deg C and protected from light. UV-Vis spectrophotometry was used to measure the concentration of the SERS NP conjugates by comparing the absorbance of NP conjugates with the absorbance of stock NPs whose concentration is known (Figure 2.3).

2.2.2 Cell culture and flow cytometry

The cell lines employed in these studies were A431 (ATCC, CRL-1555), U251 (Krackeler Scientific, 45-09063001), 3T3 (ATCC, CRL-1658), and SkBr3 (ATCC, HTB-30D). A431, U251, and 3T3 cells were cultured in DMEM medium (Lonza, 12-604F), while SkBr3 cells were cultured in Mccoy's 5A medium (Lonza, 12-688F), both of which were supplemented with 10% fetal bovine serum (FBS; Thermo Scientific, SH3008803) and

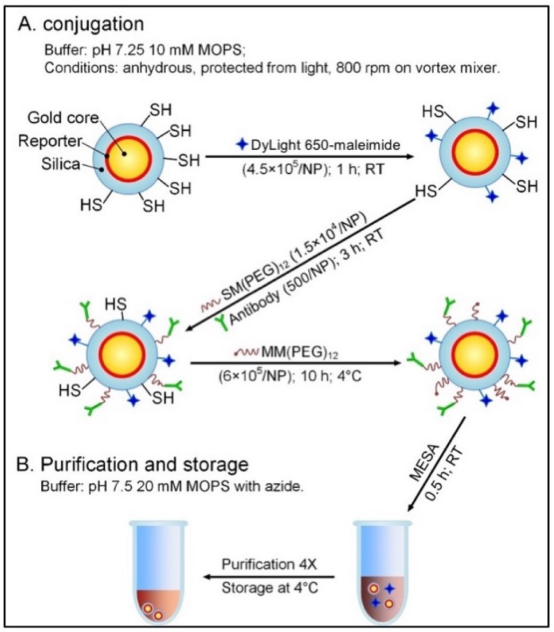

FIGURE 2.2: **Schematic illustration of the preparation of SERS NPs conjugated to monoclonal antibodies and fluorophores for flow cytometry.** (**A**) Conjugation and (**B**) purification. This figure was originally published in [93].

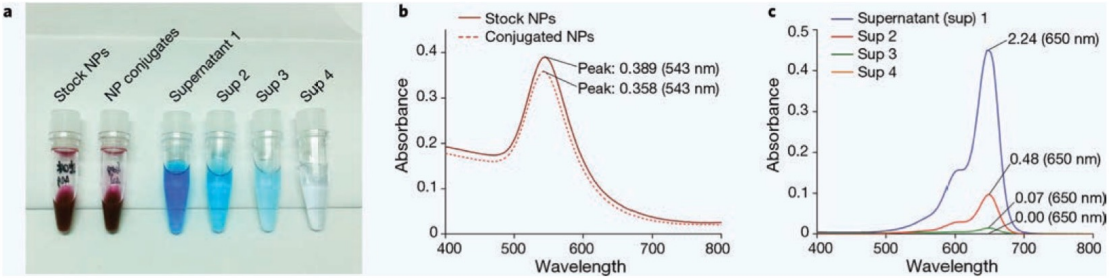

FIGURE 2.3: **UV-Vis spectrophotometry for purifying and calculating the concentration of NP conjugates.** (**A**) The color of NPs and supernatants during purification; (**B**) absorbance spectra of stock NPs and conjugated NPs for calculation of NP concentration (50× dilution); (**C**) absorbance spectra of supernatant (3× dilution; the main component is DyLight 650) from 4 rounds of purification. This figure was originally published in [93].

1% penicillin-streptomycin (Lonza, 17-602E). All cells were cultured at 37-deg C with 5% CO_2. Trypsin EDTA 1X (Mediatech, MT25051CI) was used to detach cells.

Flow cytometry samples were prepared by mixing 25 μL cell suspensions (0.2 million cells) with 25 μL of individual NP conjugates (300 pM) for 15 min at 20-deg C protected from light under gentle agitation with a vortex mixer at 300 rpm. After staining, the cells were purified three times via centrifugation (400 g for 5 min) and supernatant-replacement (500 μL per rinse) with FACS buffer (1% BSA in PBS). Figure 2.4 shows results of flow cytometry.

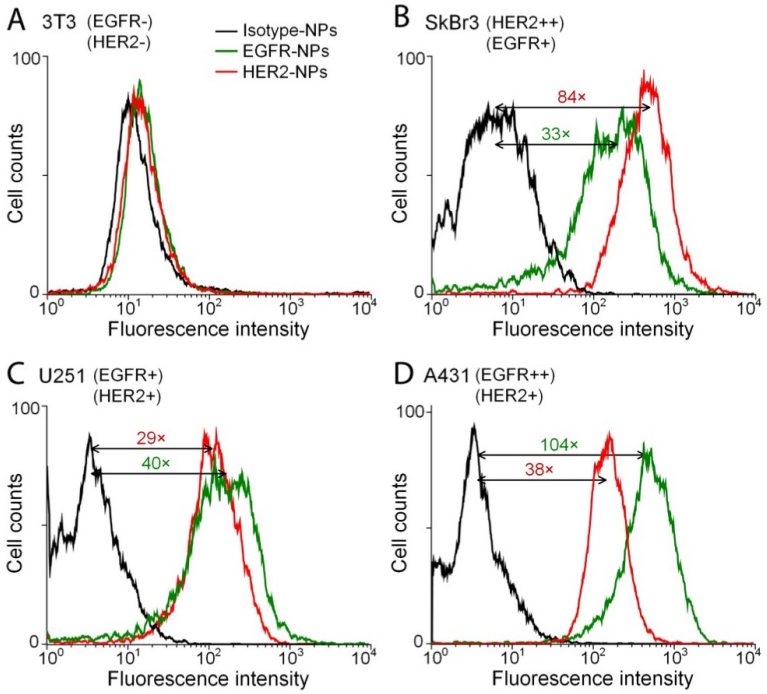

FIGURE 2.4: **Flow cytometry validation of conjugated NPs with various biomarker-positive cell lines.** EGFR-HPs, HER2-NPs and isotype-NPs were individually used to stain (**A**) 3T3 (EGFR- and HER2-negative), (**B**) SkBr3 (HER2++, EGFR+), (**C**) U251 (EGFR+, HER2+), or (**D**) A431 (EGFR++, HER2+) cell lines. The colored numbers represent the ratio of the mean fluorescence intensity between a targeted NP (EGFR-NP or HER2-NP) vs. an untargeted NP (isotype-NP). This figure was originally published in [84].

2.2.3 Mouse xenograft model and human breast tissues

Nude mice (Taconic Farms Inc, model NCRNU-F) were used to develop A431 and U251 tumor xenografts. All animal procedures were approved by the Institutional Animal Care and Use Committee (IACUC) at the University of Washington IACUC (#4345-01). The cancer cells, A431 (1×10^6), U251 (3×10^6), or SkBr3 (5×10^6), were individually suspended in matrigel (BD biosciences, 354234) at a 1:1 volume ratio to form a 100 μL mixture. Nude mice (5-8 weeks) were subcutaneously implanted in their flanks with the cell/matrigel mixture. The mice were euthanized by CO_2 inhalation when tumors reached a size of 10 mm, followed by the surgical removal of the implanted tumors.

De-identified human breast tissue specimens were obtained from consenting patients and imaged within 1–2 hr after lumpectomy or mastectomy at the University of Washington Medical Center. Tissue collection was managed by the Northwest BioTrust (NWBT) under an IRB exemption for these de-identified tissues. After imaging, the tissues were fixed with 10% formalin and submitted for histopathology (IHC and H&E staining).

2.2.4 Tissue staining and rinsing

Unstained specimens were first imaged to acquire a set of background spectra (to account for background variations during least-squares demultiplexing described in the following sub-sections). The specimen surfaces (surgical margins) were stained with NP mixtures of approximately 20 μL per 1 cm^2 of tissue area (150 pM per flavor) and contained 1% BSA to minimize nonspecific binding (an optimal staining condition found in our previous studies [85]). The staining was performed according to an optimized protocol described in [83], which prescribes a short dipping interval (5-sec) paired with high-frequency (∼270 Hz) mechanical vibration to maximize NP-staining efficiencies. The high-frequency mechanical vibration was implemented by positioning two vibration motors (Yuesui, B1034.FL45-00-015) under the glass slide used for staining to introduce a high-frequency vibration to the staining solution and tissue. After staining the tissue surface, the specimen was rinsed by submerging the entire specimen into a beaker containing approximately 50-mL PBS, and gently agitated for 10 sec.

2.2.5 Raman imaging system

A customized spectral-imaging system was developed to measure the concentration and concentration ratio of SERS NPs that were topically applied on tissue specimens (Figure 2.5) [85]. The NP-stained surface (surgical margin) of the tissue specimen was raster-scanned with a two-axis stage (Newmark systems Inc., ET-50-11) and imaged using a fixed spectral-imaging probe (FiberTech Optica Inc.). The imaging probe utilized a multimode fiber (100-μm core, 0.10 NA) at the center of the probe for illumination, and 27 surrounding multimode fibers (200-μm core, 0.22 NA) for collection of Raman, autofluorescence, and backscattered laser light. A 785-nm diode laser was first filtered with a narrow-bandpass filter (Semrock, LD01-785) prior to being coupled into the illumination fiber at the center of the fiber bundle. This removed off-resonant laser noise (including amplified spontaneous emission) that may be collected by the multimode collection fibers and contributed background signal and shot noise to the Raman spectra. The illumination fiber created a laser spot at the tissue (∼15 mW, well below ANSI safety limits) with a diameter of 0.5 mm (imaging resolution). The multimode fibers that surround the illumination fiber collected light from the illuminated spot and were reconfigured into a linear array at the proximal end of the bundle, which served as the

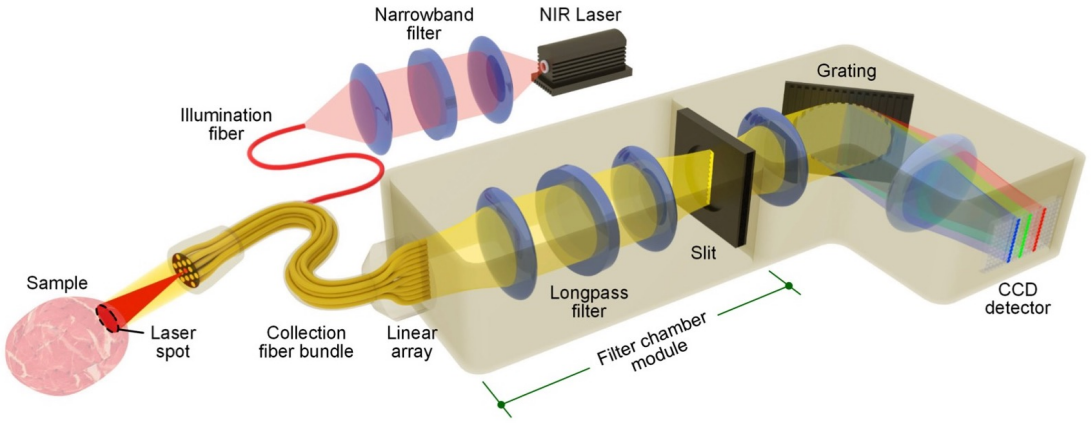

FIGURE 2.5: A common optical configuration for the imaging of SERS NPs in tissues. A 785-laser is used to illuminate the NP-stained tissue, creating a submillimeter-diameter laser spot. Raman-scattered photons from illuminated NPs are collected by 27 multimode fibers and transmitted to a customized spectrometer, where they are dispersed onto a cooled deep-depletion spectroscopic CCD. This figure was originally published in [86].

entrance slit into the spectrometer. Since a large amount of the laser light (785-nm illumination wavelength) was collected by our multimode collection fibers, a longpass interference filter (Semrock LP02-830RU-25) was used to reject illumination light at 785-nm, as well as any autofluorescence background at shorter wavelengths than the Raman peaks ($<$ 830-nm). A 150-μm slit was used to filter out the diffuse stray light in the filter chamber module from photons that were rejected by the longpass filter. A volume phase grating dispersed the collected light onto a cooled deep-depletion spectroscopic CCD (Andor, Newton DU920P-BR-DD). Note that the spatial filter was not perfect and still allowed a significant amount of stray laser light into the spectrometer, which contributed to the broadband background seen by the CCD.

2.2.6 Demultiplexing SERS spectra using direct classical least squares (DCLS)

This study employed a demultiplexing method described previously [84, 85]. In a realistic spectral measurement, pure spectra from single- or multi-flavor particle mixtures are mixed with varying magnitudes of broadband background signals (mainly due to laser background and autofluorescence background) and zero-mean Gaussian-distributed white noise (includes shot noise and other stochastic noise sources such as detector readout noise and dark counts). Other than sources of noise, it was assumed

that each measured spectrum (S) consisted of a weighted sum of fixed NP spectra (F_n) and broadband background signals (B). Based on the assumption that the combination was linear, a linear least-squares algorithm was employed in MATLAB (MathWorks, R2017a) to compute the relative NP weights (w_n). A third-order polynomial (P_m) was included to account for broadband background signals that were not captured by the broadband noise reference spectrum (B). The reference spectra and the background reference were background-corrected to remove detector offset due to readout noise. Spectra were acquired through full-vertical binning of the pixels in each column of the CCD using the full dynamic range of the CCD sensor to minimize digitization noise. The linear least-squares fitting minimized the residual, R, in the following equation:

$$\boldsymbol{S} = \sum_n w_n F_n + kB + \sum_m a_m \boldsymbol{P}_m + \boldsymbol{R} \tag{2.1}$$

where:

$\boldsymbol{S}$ = measured spectral data

w_n = weight of SERS flavor$n$

F_n = known reference spectrum of SERS NP flavor n

k = scaling factor for background signal magnitude

B = known reference spectrum of broadband backgound

a_m = weight of mth-order polynomial term

$\boldsymbol{P}_m$ = mth-order polynomial term (for baseline correction)

$\mathbf{R}$ = residual (minimized by least-squares algorithm)

2.3 Experimental REMI results

The custom raster-scanned imaging system (Figure 2.5) was utilized to demonstrate the ability to image and accurately quantify relative biomarker expression levels in fresh tissues with topically applied SERS NPs. An imaging rate of 2 mm/s was utilized with an illumination spot size (resolution) of 0.5 mm and a sampling pitch of 0.5 mm/pixel. To validate this system, tumor xenografts that were stained with an equimolar mixture of EGFR-NPs and isotype-NPs were imaged (Figure 2.6). As shown in Figure 2.6B, the

ratiometric images provides a quantitative representation of EGFR expression that is consistent with IHC and flow cytometry results (Figures 2.4 and 2.6C).

To demonstrate the ability to image multiple biomarkers simultaneously, various tumor xenografts were stained with an equimolar mixture of three NP flavors: EGFR-NPs, HER2-NPs, and isotype-NPs (Figure 2.7). As shown in Figures 2.7B-D, the REMI images of EGFR and HER2 expression in various tumor xenografts show excellent quantitative agreement with corresponding flow-cytometry results ($R > 0.98$).

To further demonstrate the feasibility of REMI for intraoperative assessment of surgical margins, eight fresh human breast tissue specimens resected from five patients were imaged (Figure 2.8). Each tissue specimen was stained with a 5-flavor NP mixture (EGFR-NPs, HER2-NPs, CD44-NPs, CD24-NPs, and isotype-NPs for 10 min, followed by a 20-sec rinse step in PBS. The entire staining-and-imaging procedure was performed in less than 15 min. Ratiometric REMI quantifies HER2, EGFR, CD44, and CD24 expression levels in agreement with IHC validation data (Figure 2.8B-C). The concentration ratios of biomarker-targeted NPs vs. isotype-NPs on IHC-validated biomarker-positive regions are significantly elevated (Figure 2.8D), indicating preferential binding of targeted NPs to their biomarker targets with sufficient tumor-to-normal contrast.

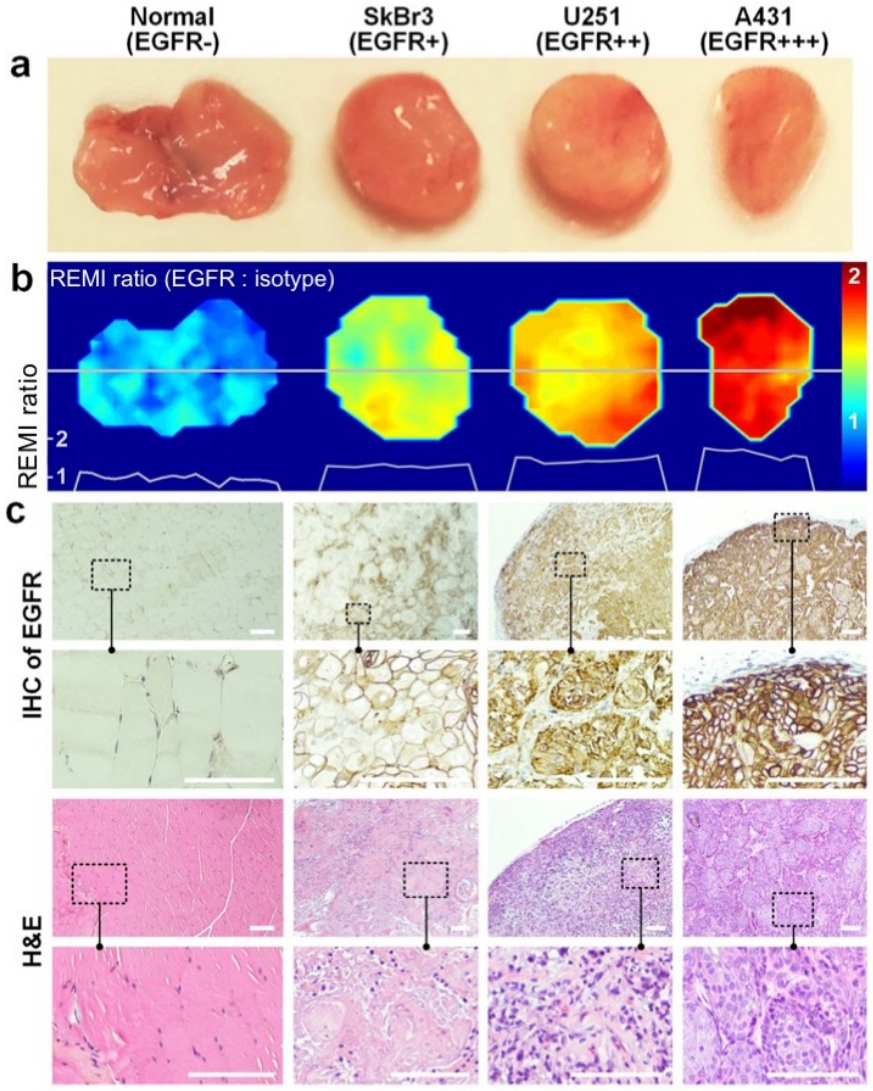

FIGURE 2.6: **REMI of normal tissue (EGFR-negative) and tumor xenografts (SkBr3, U251, and A431) that express various levels of EGFR.** The tissues were stained with a two-flavor NP mixture (EGFR-NPs and isotype-NPs) and the staining-and-imaging procedure was achieved in less than 15 min. (**A**) Photographs of resected normal tissue (muscle) and tumor xenografts. (**B**) REMI images of the concentration ratio of EGFR-NPs vs. isotype-NPs. The line profiles at the bottom of the image indicate the REMI ratios along the gray line through the center of each tissue specimen. (**C**) Validation data: IHC for EGFR (10× and 40× views), and H&E staining (10× and 40× views). The scale bars represents 100 μm. This figure was originally published in [85].

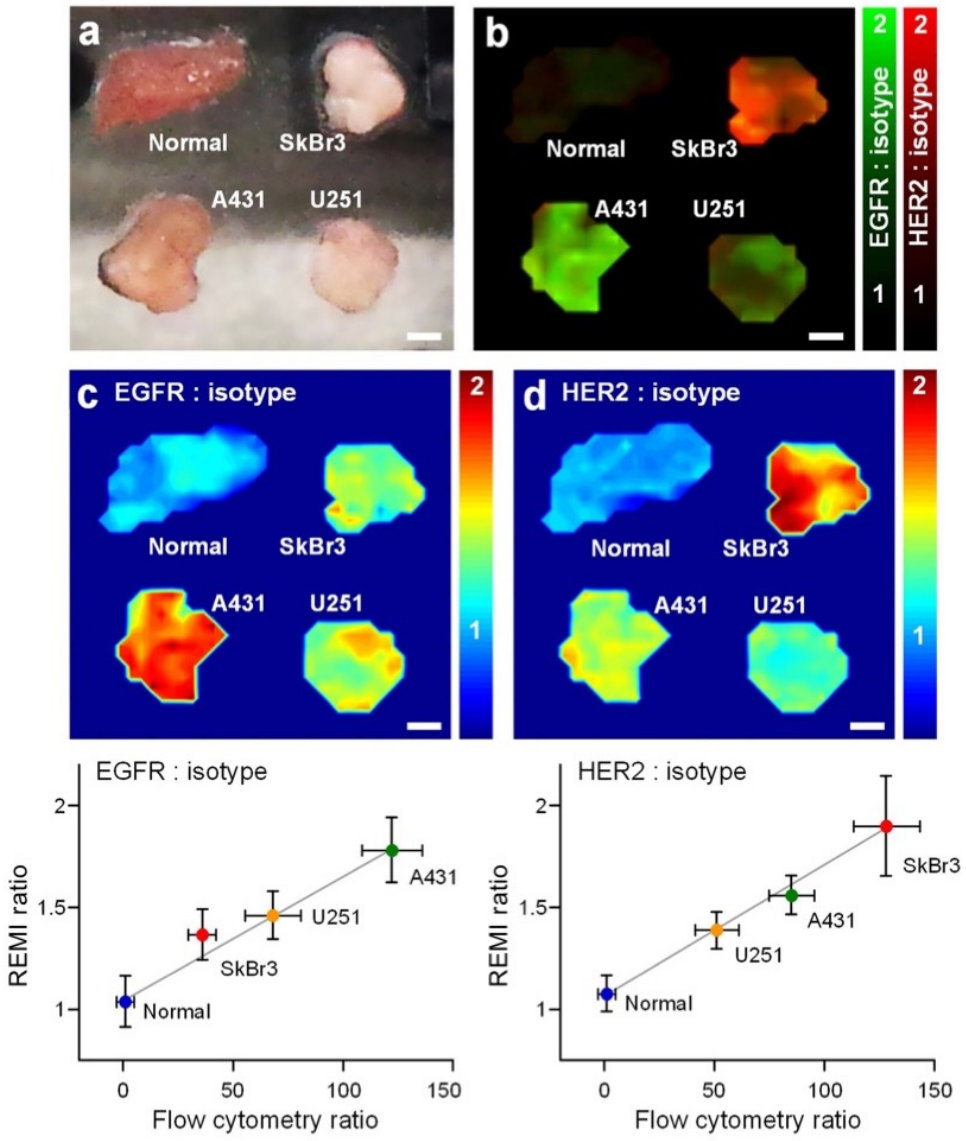

FIGURE 2.7: **REMI of tumor-xenograft specimens stained with a 3-flavor NP mixture (EGFR-NPs, HER2-NPs, and isotype-NPs).** (**A**) Photograph of resected tumor xenografts and normal tissue. (**B**) A multiplexed REMI image generated by overlaying the ratiometric images of EGFR-NPs/isotype-NPs (plotted with a green colormap) and HER2-NPs/isotype-NPs (plotted with a red colormap). Images showing the concentration ratio of (**C**) EGFR-NPs/isotype-NPs and (**D**) HER2-NPs/isotype-NPs. REMI images were obtained with a spatial resolution of 0.5 mm. The bottom plots show the correlation between the REMI ratio of a particular tissue specimen (in C, D) and the corresponding fluorescence ratio (targeted-NP vs. isotype-NP) from flow-cytometry experiments with the cell lines used to generate the various tumor xenografts. $R < 0.98$. Scale bars represent 2 mm. This figure was originally published in [85].

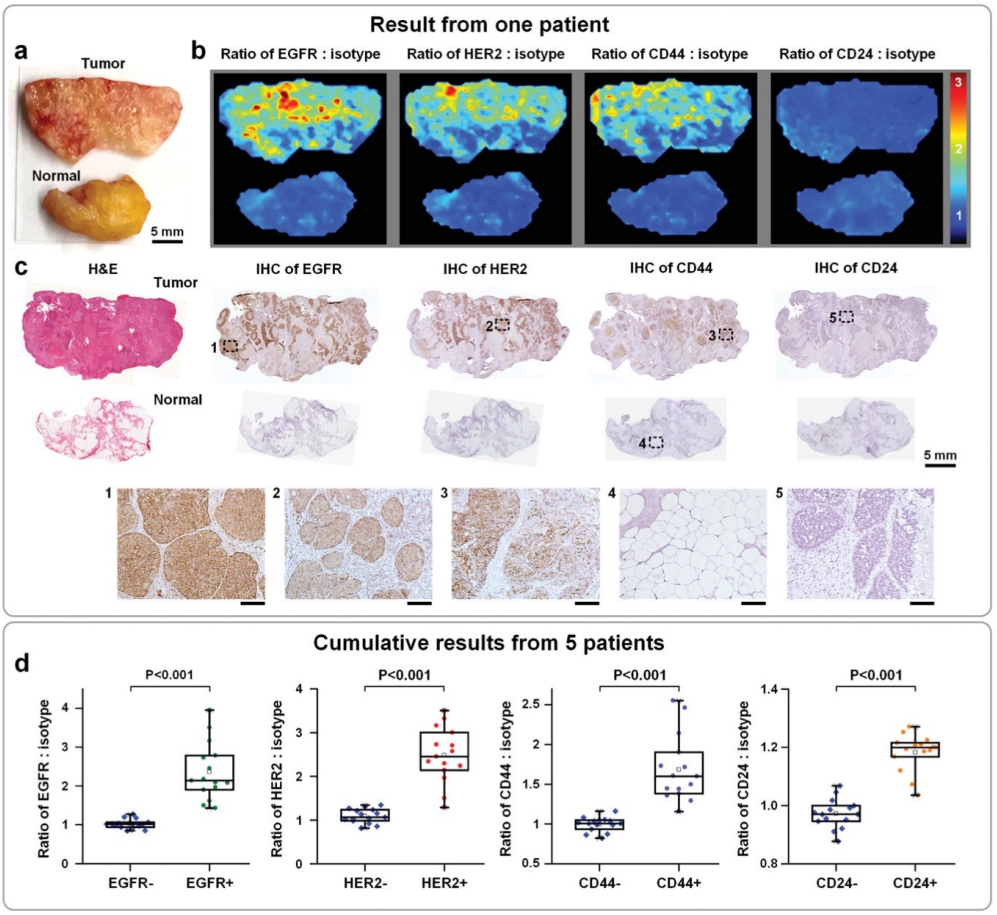

FIGURE 2.8: **Multiplexed molecular imaging of freshly excised human breast tissues stained with a five-flavor mixture of NPs.** Each tissue specimen was stained with an equimolar mixture of HER2-NPs, EGFR-NPs, CD44-44 NPs, CD24-NPs, and isotype-NPs (5-min), followed by a quick rinse in PBS (10-sec) and raster-scanned imaging ($\sim$ 3-min) to simultaneously quantify the expression of four biomarkers: EGFR, HER2, CD44, and CD24. (**A**) Photograph of a human breast tumor and a normal tissue specimen from one patient. (**B**) Ratiometric images of EGFR-NPs vs. isotype-NPs, HER2-NPs vs. isotype-NPs, CD44-NPs vs. isotype-NPs, and CD24-NPs vs. isotype-NPs. (**C**) Validation data: H&E and IHC for EGFR, HER2, CD44, and CD24. Unlabeled scale bars represent 200 μm. (**D**) Cumulative results from multiple regions of interest from a total of five patient specimens: measured NP ratios on IHC-validated biomarker-negative and biomarker-positive tissue regions. Each data point in teh plot is the average ratio from one region of interest. This figure was originally published in [83]

2.4 Limitations and technical needs

While it has been demonstrated that REMI may potentially be used to guide tumor-resection procedures (Figures 2.6, 2.7, and 2.8), additional work is necessary to further improve the REMI technique for clinical translation into intraoperative settings. For example, due to the narrow window of time that is allowed for intraoperative assessment

of surgical margins, reducing the imaging speed without compromising image quality is of critical importance. The current REMI system utilizes 1024 spectral channels and is capable of imaging a 2×2 cm^2 area of fresh tissue in approximately five minutes [93, 85]. Exploring methods to improve the speed of REMI is an intuitive step towards the clinical translation of REMI into time-limited intraoperative settings. Chapter 3 will explore the feasibility of channel-compressed spectrometry to potentially improve the speed and/or sensitivity of REMI.

We have previously shown that the co-administration of an untargeted control NP can mitigate nonspecific effects that arise as a result of uneven NP delivery, retention, and washout at different tissue locations, all of which contribute to misleading image contrast. By calculating the ratio of the concentration of targeted NP(s) to the untargeted control NP, the effects of nonspecific accumulation may seemingly be normalized away. However, despite the strengths of this ratiometric approach, we find that nonspecific accumulation and passive retention of NPs is often quite high, which can limit the sensitivity and accuracy of biomarker detection/quantification (*i.e.*, the ratios are lower than we would like). The development of a tool to better understand and quantify the specific vs. nonspecific accumulation of NPs in tissue would provide great value in understanding how to minimize nonspecific accumulation of topically applied NPs in fresh tissues. Such a tool will be developed in Chapter 4 and used to explore the diffusion and chemical binding of NPs topically applied onto the surfaces of fresh tissues.

Finally, we find that the optimization of staining, rinsing, imaging, and analysis protocols for REMI is costly in terms of time and resources [93, 83]. To help establish optimized protocols, a mathematical compartmental model is presented in Chapter 5 that can accurately simulate realistic tumor contrast during defined tissue staining and rinsing protocols. This "forward" model will be of particular value in helping to improve tumor-to-healthy tissue contrast in cancer molecular imaging with topically applied imaging agents, such as guiding the developing of imaging agents, uncovering the fastest means of staining and rinsing to achieve sufficient tumor-to-healthy tissue contrast within a time-frame feasible for intra-operative applications, and helping to select and compare data analysis approaches. Lastly, this forward model may be used in testing more quantitative methods of evaluating tumor margins (*e.g.*, the use of multi-stage staining/rinsing processes to allow kinetic model fitting of data) so that a kinetic model developed in

a later study can ultimately provide clinical value in accurately quantifying biomarker expression levels at surgical margin surfaces.

Chapter 3

Channel-compressed spectrometry for improved optical detection sensitivity

Here, we explore the feasibility of channel-compressed spectrometry for the detection of up to 5 multiplexed flavors of SERS NPs. Initial characterization and optimization of the channel-compression strategy is performed by analyzing the linearity of detection for 5 multiplexed flavors of SERS NPs over a range of concentrations. After determining the minimum number of spectral channels that are required for accurate detection of clinically relevant concentrations of NPs, this compression method is validated by acquiring realistic multiplexed molecular images of tumor xenografts and freshly excised human breast tumor specimens. It should be noted that the work presented in this chapter has been published in [110].

3.1 Spectral binning

In order to explore the feasibility of channel compression in this study, a spectral-binning strategy was employed, in which the full 1024 spectral pixels collected by the commercial CCD were divided into "bins," where the value of each bin was the mean of all pixel values within that bin (Figure 3.1). We explored the variability in the demultiplexing output when the relative positions of the bins were shifted ("phase-shifted"). While the

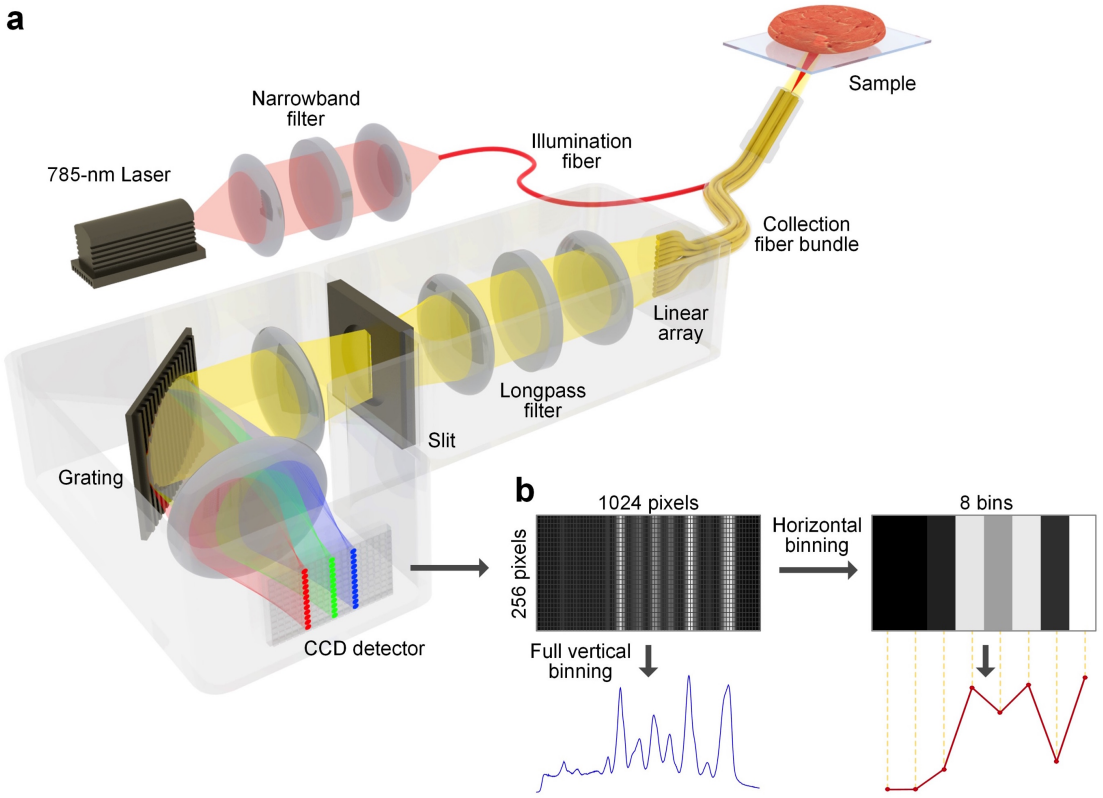

FIGURE 3.1: **(A) The REMI system and (B) the channel-compression strategy.** (**A**) Schematic of the spectral-imaging system. A 785-nm laser is used to illuminate the NP-stained tissue, creating a 1 mm-diameter laser spot. Raman-scattered photons from illuminated NPs are collected by 27 multimode fibers and transmitted to a customized spectrometer, where they are dispersed onto a cooled deep-depletion spectroscopic CCD. (**B**) The camera is used in full-vertical binning (FVB) mode, in which the signal from all 27 collection fibers are binned together by the camera, with 1024 pixels (spectral channels) used to resolve the grating-dispersed wavelength axis. In this study, the 1024-channel data set is further binned along the wavelength axis (horizontal binning) to examine the effects of spectral compression. This figure was originally published in [110]

shape of the spectra varies as a function of phase (bin locations), it was determined that in terms of the accuracy of demultiplexing, the effect of phase shifting did not dominate over random experimental noise. This is because using a larger number of bins, in which the spectral features are well-resolved, allows for accurate demultiplexing regardless of phase ($< 5\%$ error for 16 or more bins), while using a smaller number of bins, which causes significant blurring of the spectral features, results in low demultiplexing accuracy regardless of phase (*e.g.*, 90% error for 8 bins). These two extreme cases illustrate why, in general, the phase of the bins does not play a major role in the accuracy of demultiplexing (as observed in our experiments for 8, 16, and 32 bins). Therefore, we disregarded phase-shifting effects in this study.

3.2 Results

The linearity of the REMI system was measured using a mixture of 5 NP flavors prepared in a concentration ratio of 1:1:1:1:1 or 3:2:1:1:1 with droplets from each mixture placed on the surface of rat tissue at varying concentrations (0.5–100 pM). Figures 3.2A-D show the linearity of measured NP concentrations and concentration ratios for 5 NP flavors mixed in the 1:1:1:1:1 ratio (Figures 3.2A-B) or in the 3:2:1:1:1 ratio (Figures 3.2C-D). The concentration ratios are based on the concentration of NP flavors S420, S421, S481, and S493 against the concentration of NP flavor S440 (assumed to be the "negative-control" NP in this case). Figure 3.2B shows that the concentration ratios measured from the 1:1:1:1:1 NP mixtures remain near unity for NP concentrations ranging from 2–100 pM. However, for samples with NP concentrations below 1 pM, larger errors in the concentration ratio ($> 10\%$) appear. Similarly, Figure 3.2D shows that the measured ratios are accurate ($< 10\%$ error) when all NP concentrations are greater than 2 pM. The non-equimolar volume ratio of 3:2:1:1:1 represents a scenario in *ex vivo* tissue imaging in which the specimen greatly overexpresses a certain protein biomarker (3-fold enhanced binding compared to the control NP), while moderately overexpressing another protein biomarker (2-fold enhanced binding compared to a control NP), with two other biomarkers that are negligibly expressed (no enhanced binding, which yields a NP ratio of 1). This range of ratios is consistent with our previous REMI experiments with fresh tissues [92, 93, 86].

A limit-of-detection (LOD) analysis was conducted using the linearity data to determine the minimal number of spectral channels needed to ensure accurate measurement of NP concentrations. In this case, the LOD is defined as the NP concentration at which the error in the concentration ratio exceeds 10%. A plot of the LOD as a function of number of spectral bins is shown in Figures 3.2E-F. These plots show that the LOD gradually deteriorates as the number of spectral channels (or bins) decreases, with the shaded region indicating the experimental variability in the LOD measurements (standard deviation, $n = 5$). Based on Figures 3.2E-F, the LOD remains below 10 pM as long as a minimum of 16 bins is used. Note that in REMI experiments with fresh tissues, using an optimized topical staining protocol (150 pM/flavor, 10 min of staining), the measured NP concentrations are typically above 10 pM [107]. Therefore, even with only 16 spectral channels, we would expect accurate REMI measurements of tissues.

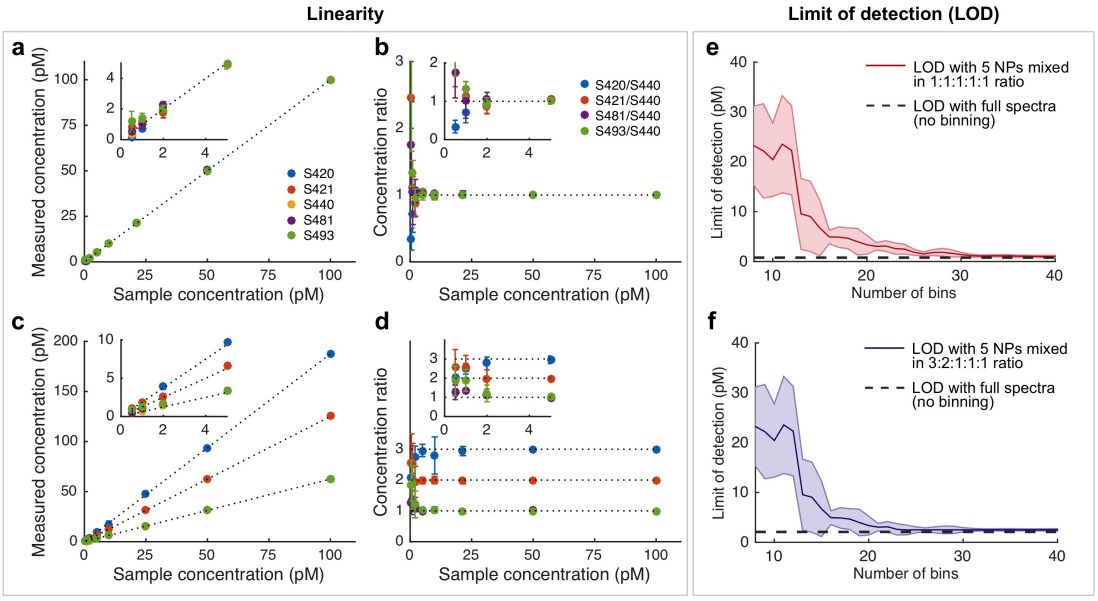

FIGURE 3.2: **(A-D) Linearity test for 5-flavor NP mixtures and (E, F) the limit of detection (LOD) as the number of bins (spectral channels) is reduced.** (**A-D**) Five NP flavors were mixed in an equimolar concentration ratio (1:1:1:1:1) or a concentration ratio of 3:2:1:1:1 (S420:S421:S440:S481:S493). Various dilutions of these NP mixtures were prepared in the range of 0.5—100 pM. The NP concentrations were measured with the REMI system to calculate their concentration ratios. (**A, B**) Linearity plots for the 1:1:1:1:1 NP mixture. (**C, D**) Linearity plots for the 3:2:1:1:1 NP mixture. Error bars represent the standard deviation across 5 repeated experiments. Note that the "sample concentration" refers to the concentration of the S440 NP (which serves as the negative-control NP). (**E, F**) The limit of detection (LOD) is defined as the concentration at which the error in the measured concentration ratio exceeds 10%. The shaded curves indicate the standard deviation in the LOD measurements from 5 repeated experiments.

To validate the spectral binning strategy, we first binned spectral data acquired from REMI experiments with A431 tumor xenografts (subcutaneously implanted in mice). These tissue specimens were stained for 10 min with an equimolar mixture of targeted-NPs, unconjugated NPs, and isotype-NP, in which the unconjugated NPs exhibit similar behavior to the isotype-NP [93]. Figure 3.3A shows the ratiometric images of targeted-NPs vs. isotype-NPs (EGFR-NP/isotype-NP and HER2-NP/isotype-NP) and unconjugated-NPs vs. isotype-NPs (unconjugated-S481-NP/isotype-NP and unconjugated-S493/isotype-NP) in each of the respective rows. The ratio of unconjugated-NPs vs. isotype-NPs is expected to lie near unity, since none of these NP flavors is targeted to a specific cell-surface molecular biomarker. The different columns in Figure 3.3A show ratiometric images obtained with a decreasing number of spectral channels. The first column shows the ratiometric image of an A431 tumor xenograft when no binning is performed (the 1024-channel "gold-standard" in this work), while columns 2–4 show the

ratiometric images obtained when the spectral data is compressed into 32 bins, 16 bins, and 8 bins, respectively. Figure 3.3A shows that the 32-bin and 16-bin spectral compression yields ratiometric images that are consistent with the gold-standard images, in which there is a high ratio of EGFR-NP vs. isotype-NP (∼3), a moderate ratio of HER2-NP vs. isotype-NP (∼2), and a ratio near unity for the unconjugated-S481-NP vs. isotype-NP and unconjugated-S493-NP vs. isotype-NP. Spectral compression down to 8 bins results in low-fidelity ratiometric images. Figure 3.3C shows an H&E-stained *en face* histology section from the same A431 tumor xenograft imaged with REMI, which confirms the relatively homogenous distribution of tumor cells throughout the tumor xenograft specimen.

To quantitatively evaluate the spectrally binned imaging data, we computed the pixel-by-pixel error of the binned images in comparison to the gold-standard (no binning) images. The results from all pixels (average and standard deviation) are displayed as bar plots in Figure 3.3D. With 16 bins, the errors are well below 20% (grey dashed line), and with 32 bins, the errors are below 10%. These results indicate that by using only 16 or 32 spectral channels, we can obtain ratiometric images with high fidelity to those obtained using the full 1024 spectral channels.

The spectral binning strategy was further validated for rapid molecular imaging of fresh human breast tissues. Figure 3.4A shows ratiometric images of targeted-NPs vs. isotype-NPs (EGFR-NP/isotype-NP, HER2-NP/isotype-NP, CD24-NP/isotype-NP, and CD44-NP/isotype-NP) in each of the respective rows, while the columns show ratiometric images obtained with a decreasing number of spectral channels. Unlike the tumor xenograft in Figure 3.3, the human specimen in Figure 3.4 exhibits a more heterogeneous tumor distribution. A high ratio of EGFR-NP vs. isotype-NP is observed (∼4), as well as a high HER2-NP vs. isotype-NP ratio (∼3.5), low CD24-NP vs. isotype-NP ratio (∼1), and a moderate CD44-NP vs. isotype-NP ratio (∼2). Qualitatively, the images obtained with 32-bin and 16-bin spectral compression exhibit image features comparable to those in the gold-standard images. The tissue was submitted for histopathology after imaging. Examination of H&E-stained sections of the tissue validated the heterogeneous distribution of the tumor cells. Figure 3.4D shows the error in the pixel values (average and standard deviation) between the spectrally compressed images and the gold-standard images. With only 16 bins, the errors in the ratio of EGFR-NP vs. isotype-NP, HER2-NP vs. isotype-NP, and CD44-NP vs. isotype-NP are below 20% (grey dashed line).

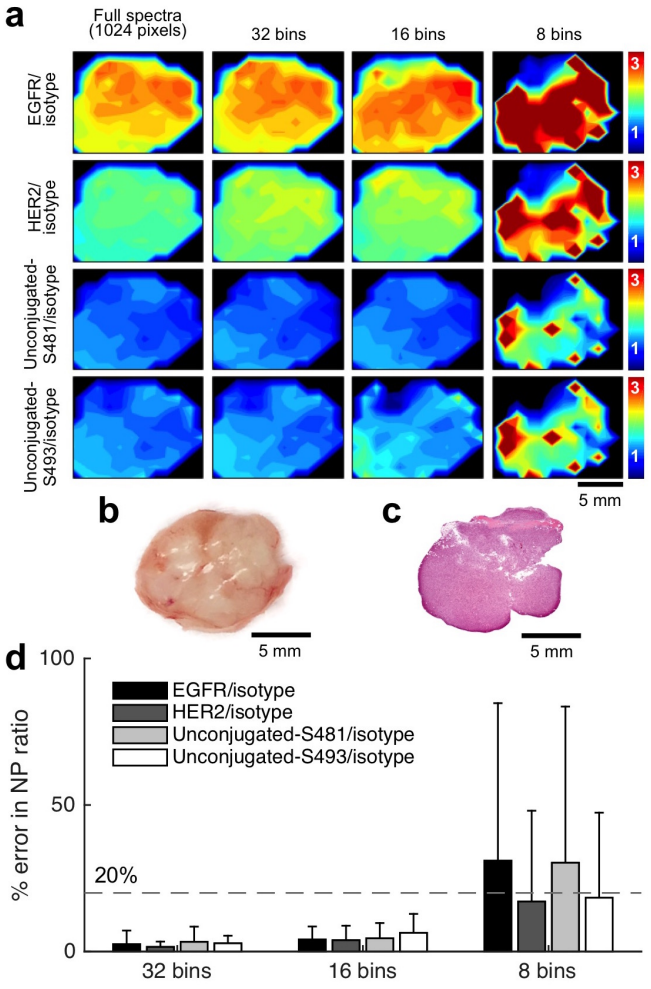

FIGURE 3.3: **REMI approach performed on an A431 tumor xenograft (EGFR++, HER2+) stained with a 5-flavor NP mixture (EGFR-, HER2-, Control-S481-, Control-S493-, and isotype-NPs, 150 pM/flavor).** (**A**) Ratiometric images of the tumor xenograft. From top to bottom, each row shows the ratio of EGFR/isotype-NP, HER2/isotype-NP, unconjugated-S481/isotype-NP, and unconjugated-S493/isotype-NP, respectively. From left to right, each column shows the ratiometric image obtained with a decreasing number of spectral channels. (**B**) A photograph of the A431 tumor xenograft. (**C**) H&E-stained pathology section of the tumor xenograft. (**D**) Average error (%) in the measurement NP ratios when using spectral compression in comparison with the gold-standard images (full 1024 channels).

Error bars represent the standard deviation amongst all pixels in the image.

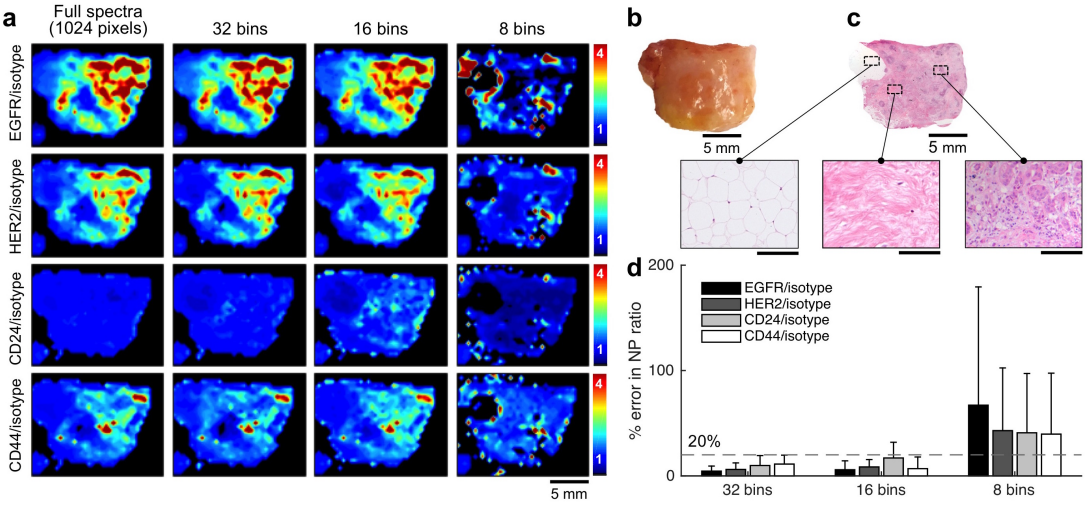

FIGURE 3.4: **REMI approach with channel-compressed spectrometry performed on a human breast tissue specimen stained with a 5-flavor NP mixture (EGFR-, HER2-, CD24-, CD44-, and isotype-NPs, 150 pM/flavor).** (**A**) Ratiometric images of a human breast tissue specimen. From top to bottom, the rows display ratiometric images of EGFR/isotype-NP, HER2/isotype-NP, CD24/isotype-NP, and CD44/isotype-NP. From left to right, the columns display ratiometric images obtained with a decreasing number of spectral channels. (**B**) A photograph of the tissue specimen. (**C**) H&E histology of the specimen, with higher magnification views of fat (left), normal breast tissue (middle), and tumor (right). Unlabeled scale bars represent 200 μm. (**D**) Average error (%) in the measured NP ratios when using spectral compression in comparison to the gold-standard images (full 1024 spectral channels). The error bars represent the standard deviation amongst all pixels in the image.

The error in the ratio of CD24-NP vs. isotype-NP is slightly worse due to the low measured concentration of CD24-NPs (∼5 pM from the poorly stained tissue regions) that was below the LOD with 16-bin spectral compression (Figures 3.2E-F). However, with 32-bin spectral compression, the errors for all NP ratios remain below 20%. While the use of 32 spectral channels may be more robust than the use of 16 spectral channels, utilizing brighter NPs and improved staining protocols may enable accurate imaging using 16 channels in the future.

3.3 Discussion

The study presented here aims to explore and improve a strategy for rapid molecular imaging of superficial tissue surfaces in order to guide tumor-resection procedures. The wide-area REMI system described in Chapter 2 uses 1024 spectral channels and is capable of imaging a 2×2 cm^2 area of fresh tissue in approximately five minutes [93, 85]. Due to the narrow window of time that is allowed for the intraoperative assessment of the

margins of excised tissue specimens, it is desired to further improve the imaging speed of REMI without compromising the accuracy in biomarker detection.

Here, we have investigated the feasibility of channel-compressed spectrometry to potentially improve the speed and/or sensitivity of REMI. We have developed and optimized a spectral binning strategy to determine the minimum number of spectral channels required to obtain ratiometric images with a desired level of accuracy when detecting low concentrations of SERS NPs. One of the primary benefits of binning is the improved signal-to-noise (SNR) ratio due to reduced read noise and increased photon counts per spectral channel/bin. The current imaging system, using a standard spectroscopic CCD, is capable of accurately demultiplexing five NP flavors at a concentration of 10 pM or above. The use of 32-channels offers a LOD that is more comparable to that of 1024 channels, as well as ratiometric images with fidelity comparable to the 1024-channel "gold-standard" (Figures 3.3 and 3.4). Note that more sophisticated spectral-compression strategies are also possible, such as utilizing a limited set of spectral-detection windows that coincide with specific Raman peaks emitted by various flavors of multiplexed SERS NPs [88]. However, this would require more complex detection optics such as non-grating-based spectral filter. On the other hand, as noted in the following paragraph, the use of uniformly spaced sequential spectral bins allows for easier adoption of certain advanced detector array technologies that are commercially available as a substitute for high-channel-count spectroscopic CCD arrays.

In summary, the results of this study are significant in showing that a very high degree of channel compression (nearly two orders of magnitude reduced from the original 1024 channels) can still allow for highly multiplexed ratiometric imaging of biomarkers with targeted SERS NPs. This opens up the possibility to use advanced detector arrays, such as a 16-channel or 32-channel photomultiplier tube (PMT) linear array or an avalanche photodiode (APD) array, which are much more sensitive and fast compared to a 1024×256 spectroscopic CCD array. For example, the current CCD used in our REMI system is only capable of acquiring up to 272 spectra per second in the FVB mode [111]. In comparison, PMT arrays can acquire up to 1.28 million spectra per second (4,700 times faster) due to their high cathode sensitivity and time-response, over a wide spectral range (300–920 nm) [112]. APD arrays feature comparable speed and even higher quantum efficiency compared to current PMT arrays in the 900-nm spectral range [113]. Improvements in spectral acquisition rate and SNR would not only be of

great clinical benefit (through faster imaging speeds), but could also enable improved spatial resolution for REMI through the use of a smaller illumination spot size coupled with a finer sampling pitch during raster-scanned imaging (*e.g.*, a 100-μm resolution for the identification of low numbers of tumor cells). Future studies will develop and assess the ability of a high-speed and high-resolution REMI system for a variety of clinical applications including intraoperative guidance of tumor resection and multiplexed molecular endoscopy of the gastrointestinal tract [106, 84, 93, 85, 114], in which imaging speed and imaging resolution are of importance.

Chapter 4

Microscopic investigation of topically applied NPs for improving contrast for accurate tumor detection

Previously, we have developed a Raman-encoded molecular imaging (REMI) strategy, with which we have demonstrated that rapid, multiplexed molecular detection is possible under time-limited staining and detection conditions, as encountered in point-of-care clinical settings [110, 84, 92, 93, 86, 85]. In our initial studies, fresh tissue specimens were topically stained with a panel of SERS and imaged after a brief rinse step to rapidly identify/quantify the presence of tumor-related biomarkers. Unfortunately, uneven NP delivery, retention, and washout at different tissue locations often result in misleading image contrast [92, 93]. For example, we have observed that increased diffusion and passive retention can often result in higher nonspecific accumulation of topically applied NPs in benign tissues in comparison to denser tumor tissues [93]. One method that has been utilized to mitigate these nonspecific effects is to co-administer an untargeted (control) NP flavor simultaneously with the targeted NP(s) during imaging experiments. By calculating the ratio of the concentration of targeted NP(s) to the untargeted control NP, the effects of nonspecific accumulation may be normalized away. We have shown

that these NP ratios provide a linear and quantitative readout that correlates with biomarker expression levels [92, 93, 83, 85].

Despite the strengths of such a ratiometric imaging approach, nonspecific accumulation and passive retention of NPs is often quite high, which can limit the sensitivity and accuracy of biomarker detection/quantification. In order to better understand and quantify the specific vs. nonspecific accumulation of our NPs, here we developed a method to investigate the diffusion and accumulation of targeted and untargeted NPs as a function of depth in fresh tissues at the microscopic scale. In short, we stained fresh tissues with a paired-agent approach using fluorophore-labeled NPs, and then snap-froze the tissues at various time points to immobilize the NPs within the tissues. We then performed fluorescence microscopy of thin frozen sections of these tissues (cross-sectional views of the tissue) and quantified the penetration and binding of the targeted and untargeted NPs as a function of depth. The findings from these studies led us to hypothesize that the use of larger NPs could reduce the diffusion of the NPs, and therefore reduce the nonspecific accumulation of the NPs in tissue. We show that this allows for molecular imaging of fresh tissue surfaces with higher NP ratios (targeted vs. untargeted) compared with our original NPs, and that the staining can be achieved more rapidly than before (6-min topical application). It should be noted that the work presented in this chapter has been published in [**?**].

4.1 Additional materials and methods

The following subsections provide additional materials and methods to those provided in Chapter 2.

4.1.1 Staining, rinsing, and snap-freezing of fresh tissue specimens (micro-REMI)

The collection of fresh tissue specimens (tumor xenografts and normal tissue) and the functionalization of NPs were prepared according to the methods described in Chapter 2, with the exception that the NPs were not reacted with the fluorophore DyLight-650. Instead, the NP flavor S420 conjugated with an anti-EGFR mAb was first reacted with the fluorophore DyLight 650-4×PEG Maleimide (Thermo Scientific, Product No.

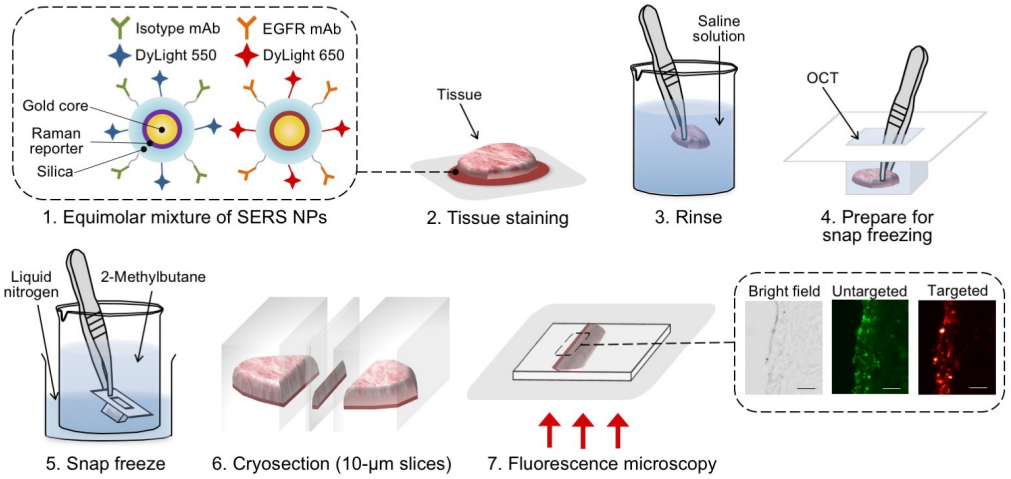

FIGURE 4.1: **Micro-REMI method.** (**1**) One SERS NP flavor was reacted with DyLight 550 and conjugated to IgG1 isotype control antibodies (mAbs), while a different SERS NP flavor was reacted with DyLight 650 and conjugated to anti-EGFR mAbs. (**2**) Fresh tissues were stained with an equimolar mixture of EGFR-targeted and untargeted (isotype-control) NPs, followed by (**3**) a brief rinse in PBS to wash away excess NP solution from the surface of the tissues. (**4**) The tissues were then placed in a cryomold containing OCT (freezing media). (**5**) The cryomold was snap-frozen in 2-methylbutane chilled in liquid nitrogen ($<$ 10 sec) and (**6**) cryosectioned into 10-μm-thick sections. These sections were then placed on a glass slide, fixed in formalin, and coverslipped. (**7**) A Leica DMi8 widefield fluorescence microscope was used to obtain bright field images of the tissue sections, as well as fluorescence images of the untargeted NPs (conjugated to DyLight 550) and the targeted NPs (conjugated to DyLight 650). Scale bars represent 25 μm.

62294), while the NP flavor S440 conjugated with an IgG1 isotype control mAb was first reacted with the fluorophore DyLight 550-2×PEG Maleimide (thermos Scientific, Product No. 62292). The motivation for this is to have brighter fluorophores that can be multiplexed in fluorescence microscopy (described in the next sub-section).

The staining and rinsing of fresh tissue specimens were performed according to methods described in Chapter 2 (15-min staining with an equimolar 150 pM mixture of targeted and untargeted NPs followed by a brief rinse step in PBS). Following this step, the specimens were then placed in a 10×10×5 mm^3 cryomold containing Tissue-Tek optimal cutting temperature (OCT) compound (Sakura Finetek USA Inc.). The cryomold was quickly frozen ($<$ 10 sec) in 2-methylbutane (Sigma Aldrich), chilled in liquid nitrogen, and cryosectioned into 10-μm-thick sections. These sections were then placed on a glass slide, fixed in formalin, and covered with a cover slip. This procedure is illustrated in Figure 4.1, and is hereafter referred to as "micro-REMI."

4.1.2 Fluorescence microscopy

Fluorescence microscope images were acquired on a Leica DMi8 widefield microscope with a 20× Plan Apochromat 0.70 numerical aperture (NA) lens. The ET555 emission filter was used for imaging untargeted NPs and the ET645 emission filter was used for imaging targeted NPs. A DFC9000 sCMOS camera was used for fluorescence detection. Images were collected using the Leica Application Suite and processed in MATLAB. The effective pixel size (Nyquist sampling) was 0.46 μm.

4.1.3 Image processing

The image processing method is shown in Figure 4.2 for a tissue section from a single A431 tumor xenograft stained for 15 minutes with an equimolar NP mixture. Bright field and fluorescence images are shown on the left. The average of all raw line profiles oriented perpendicular to the tissue surface is shown for the targeted NPs (top row) and untargeted NPs (bottom row). The fluorescence intensity was calibrated using fluorescence images of the staining mixture at a known concentration (here, the staining concentration was 150 pM). The tissue autofluorescence background was measured from the average intensity of the unlabeled tissue, and was subtracted from the NP profiles ("Background subtraction"). The maximum intensity of the NP intensity profiles was assumed to correspond to the tissue surface, which defines the zero depth on the x axes in Figure 4.2 ("Crop to surface"). Finally, the depth-integrated NP concentrations (area under the curve) were evaluated to verify that the micro-REMI results agreed with the signals obtained with the wide-area REMI technique ("Depth-integrated NP concentration"). Note that this assumes that the penetration depth of the NPs is small enough that the wide-area REMI technique collects the depth-integrated signal from all NPs at each point (pixel) on the tissue that is probed during raster-scanned spectral imaging (*i.e.*, the effects of tissue scattering/absorption are negligible at such short tissue depths of < 20 μm). All image processing was carried out in MATLAB R2015a.

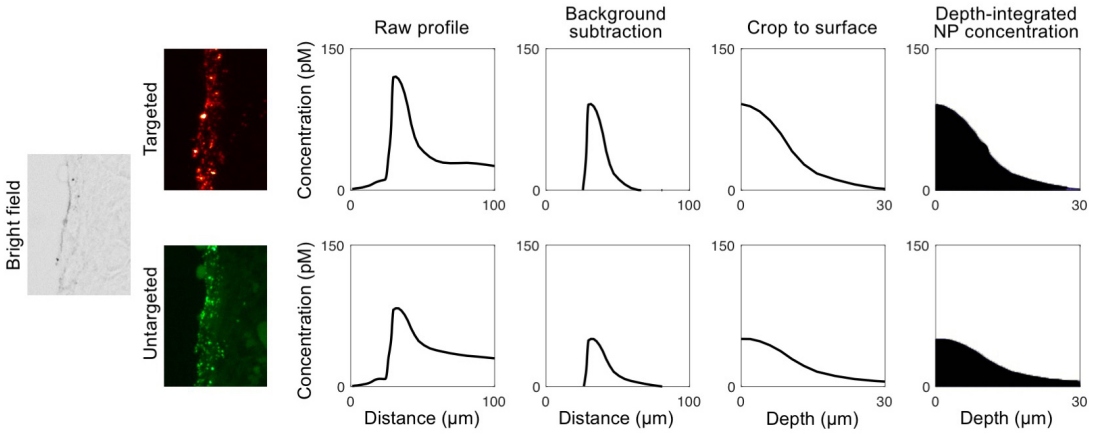

FIGURE 4.2: **Image processing.** Bright field and fluorescence images of a tissue section from a tumor xenograft stained for 15 min with an equimolar NP mixture are shown on the left. The average of all line profiles oriented perpendicular to the tissue surface is shown for the fluorescence images of targeted NPs (top row) and untargeted NPs (bottom row). The tissue autofluorescence background was measured as the average intensity in the unlabeled tissue, and was subtracted from the NP profiles ("Background subtraction"). The maximum intensity of the NP intensity profiles was assumed to correspond to the tissue surface, which defines the zero depth on the x axes in "Crop to surface." Finally, the depth-integrated NP concentrations (area under the curve) were evaluated to verify that the micro-REMI results ("Depth-integrated NP concentration") agree with the signals obtained with the wide-area REMI technique. See text for more details.

4.1.4 Silica NP thiolation and conjugation

To investigate the impact of NP diameter on tissue diffusion and molecular imaging contrast, silica NPs (SiNPs) with diameters of 200 nm and 300 nm were purchased from Nano-Composix (SISN200-10M and SISN300-10M) and conjugated to fluorescent dyes and antibodies in a similar manner to our SERS NPs. SiNPs were used due to the lack of commercial SERS NPs available in different sizes. Note that since the SERS NPs are encapsulated in a silica shell, the behavior of these NPs (SERS NPs and SiNPs) is similar in terms of diffusion and chemical binding (both specific and nonspecific) when functionalized in a similar manner. To enable PEGylation and conjugations comparable to that of our SERS NPs, sulfhydryl groups were introduced on the SiNP surfaces by heating the SiNPs for 1 hr at 72-deg C in ethanol containing 1% vol/vol (3-mercaptopropyl) trimethoxysilane (Sigma Aldrich) according to a protocol described previously [69]. The surface-modified SiNPs were thoroughly washed with ethanol and water to remove the surface modifier and were then redispersed in the reaction buffer (10 mM MOPS, pH 7.25). PEGylated SiNPs were then functionalized in the same manner as the SERS NPs

– each NP size was subjected to 2 different sets of conjugation reactions: (1) DyLight 650-4×PEG Maleimide and an anti-EGFR mAb or (2) DyLight 550-2×PEG Maleimide and an IgG1 isotype-control mAb. UV-Vis spectrophotometry (Agilent 8453) was then used to measure the concentration of the SiNP conjugates.

4.2 Results

We first verified that the signals obtained with micro-REMI agree with our standard wide-area REMI approach for imaging fresh tissue surfaces (Figure 4.3). Fresh tumor xenografts and benign tissue specimens (*ex vivo*) were stained with an equimolar NP mixture (150 pM for each NP flavor) and rinsed briefly. Wide-area REMI images were obtained according to the protocol described in Chapter 2. Ratiometric images of EGFR-targeted vs untargeted NP concentrations showed elevated ratios (1.60 ± 0.18) for A431 tumor xenografts (which overexpress EGFR) and a ratio of unity (1.08 ± 0.05; negligible differential binding of the targeted NP) for benign tissues (Figure 4.3A). An identical tissue-staining protocol was used with identical tissues, which were then snap-frozen after various staining time points and processed with the micro-REMI technique illustrated in Figures 4.1 and 4.2. Figure 4.3B illustrates the concentrations of targeted and untargeted NPs as a function of depth in the red curve (C_{tar}) and blue curve (C_{untar}), respectively. Depth-integrated NP concentrations ($\int C_{tar}dz$ and $\int C_{untar}dz$) were calculated for the areas shaded in red and blue, respectively. As described in section 4.1.3 (Image processing) the depth-integrated concentrations of targeted and untargeted NPs obtained with micro-REMI are directly proportional to the signals that would be collected with conventional wide-area REMI of an identical tissue specimen stained with an identical protocol. This is attributable to the fact that the NPs only accumulate within the first 20 μm to 30 μm beneath the tissue surface (see Figure 4.2), and surface imaging with a 785-nm light source (or other visible light source) would excite and detect all of these superficially located NPs with minimal tissue attenuation: the transport mean free path of tissue at visible wavelengths is typically $1/\mu s' \sim 1$ mm, and it is even longer at near-infrared wavelengths. In Figure 4.3 C, we demonstrate that the ratio of the depth-integrated concentrations (targeted vs. untargeted) agrees (within $< 5\%$ error) with the ratio obtained from wide-area REMI for various staining times (3–15 minutes), for both the tumor xenografts and benign tissues. We observe that for tumor xenografts, ratios

increase with staining time and plateau at an average ratio of 1.59 ± 0.24, whereas for benign tissue the ratios remain near unity for all staining times (0.90-1.09).

Figure 4.4 shows the average of thousands of concentration curves (*i.e.*, thousands of line profiles) of targeted and untargeted NPs as a function of depth from the tissue surface after staining 15 min. The preferential binding of targeted NPs in tumor xenografts can be seen in Figure 4.4A, whereas a similar behavior for both the targeted and untargeted NPs is observed in the benign tissues (Figure 4.4B). As in previous studies, a higher level of diffusion is observed in the benign tissue, presumably owing to the greater porosity of benign tissue compared to the dense tumor xenografts. Figures 4.4C-D show the concentration ratios of targeted vs. untargeted NPs as a function of depth for tumor xenografts and benign tissues, respectively. Figure 4.4C shows an elevated ratio of nearly 2 at the tissue surface, which diminishes as NPs diffuse deeper into the tissue. This suggests that by limiting the diffusion of NPs into tissue, it could be possible to obtain higher ratios in conventional wide-area REMI and increase the contrast between tumor and benign tissue for improved margin assessment. Note that the ratio of the targeted vs. untargeted NPs appears to dip below unity at greater tissue depths. We hypothesize that this could be attributable to a "binding-site barrier" effect that has been previously reported by others, and which will be discussed in the next section [115, 116, 117, 118].

From the results of our micro-REMI experiments, we reasoned that minimizing diffusion would allow for higher binding ratios. In order to achieve reduced diffusion, we chose to utilize larger NPs, which would physically limit the diffusion of NPs into tissue. This is based on the generalized Stokes-Einstein equation in which the diffusion coefficient of a spherical particle in porous media scales inversely with particle size [119]. Since larger SERS NPs are not commercially available, we used silica NPs (SiNPs) that are 200-nm and 300-nm in diameter that were then PEG-ylated and functionalized with EGFR or isotype-control mAbs in order to compare their staining behavior with our standard 120-nm silica-coated SERS NPs. As described in section 4.1.4 (Silica NP thiolation and conjugation), the SERS NPs are encapsulated in a silica shell and the behavior of these NPs (SERS NPs and SiNPs) is therefore similar in terms of diffusion and chemical binding (both specific and nonspecific) when functionalized in a similar manner. To ensure that the brightness of the fluorescence from each of the NP sizes was relatively well-matched, the NP concentrations used in the conjugation reactions were

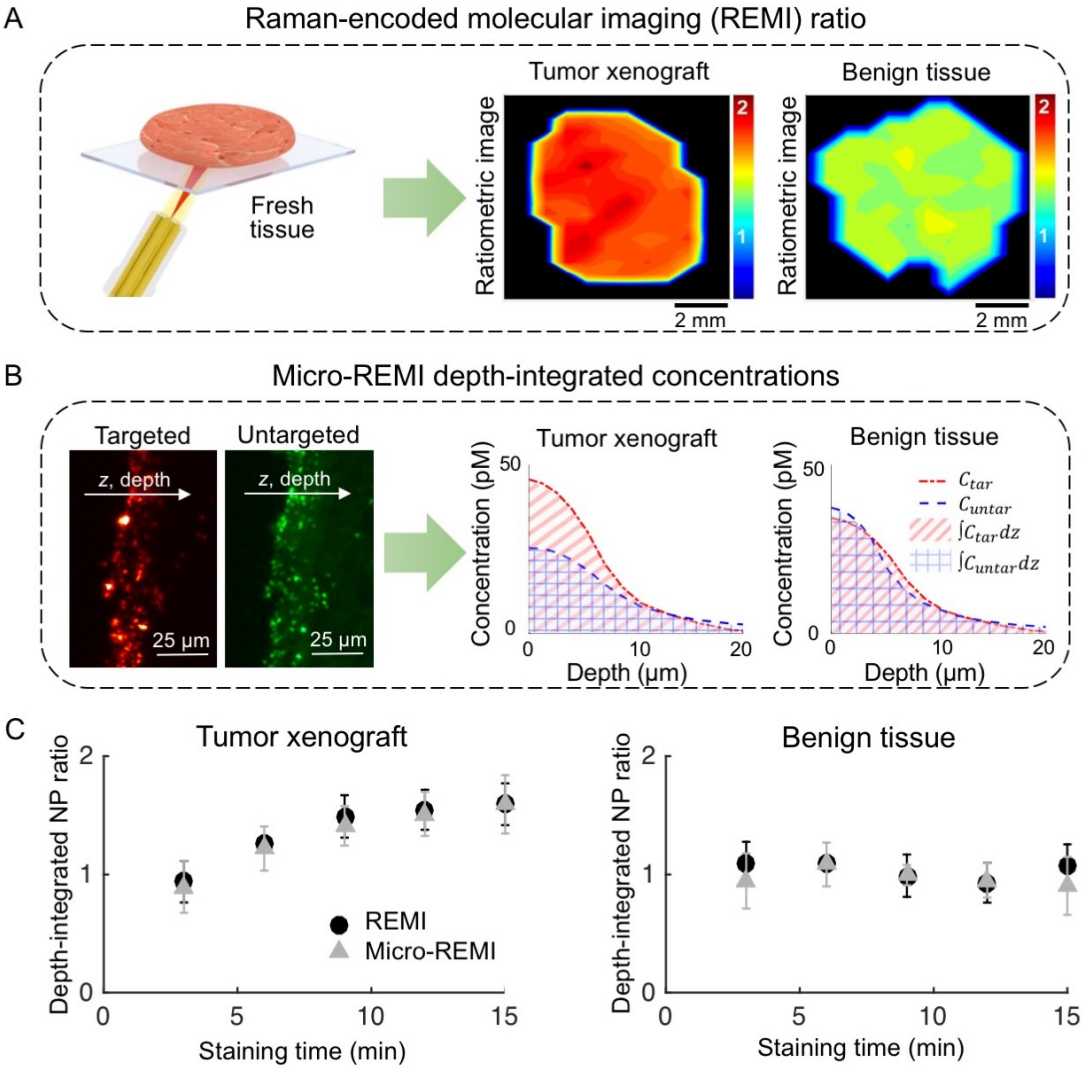

FIGURE 4.3: **Conventional wide-area REMI is used to verify the accuracy of the depth-integrated ratios calculated from micro-REMI.** The ratio of the depth-integrated concentrations of the targeted and untargeted NPs are calculated because they provide a reliable estimate of biomarker expression levels that are much less sensitive to nonspecific effects such as uneven illumination, variable staining concentrations, and heterogeneous tissue properties (*e.g.*, diffusion constants). (**A**) A fresh tissue specimen is stained with an equimolar mixture of targeted and untargeted NPs, rinsed briefly to remove excess NPs from the surface, and imaged with a customized wide-area REMI device that produces a raster-scanned image of the tissue surface. A ratiometric image of EGFR-targeted vs. untargeted NPs shows elevated ratios for the A431 tumor xenograft (which overexpresses EGFR) and a ratio of unity (no differential binding of the targeted NP) for the benign tissue. (**B**) Depth-integrated concentrations (area under the curve) of targeted and untargeted NPs (plotted as a function of depth from the tissue surface) from the micro-REMI experiments are shown for tumor xenografts (left) and for benign tissues (right). Concentrations of targeted and untargeted NPs as a function of depth are shown in the red curve (C_{tar}) and blue curve (C_{untar}), respectively. Depth-integrated NP concentrations are calculated for the regions shaded in red and blue as $\int C_{tar} dz$ and $\int C_{untar} dz$, respectively. (**C**) Ratios are plotted as a function of staining time for both REMI (black circles) and micro-REMI (grey triangles), showing good agreement ($< 5\%$ error). Error bars show the standard deviation from n = 5 experiments for each staining time.

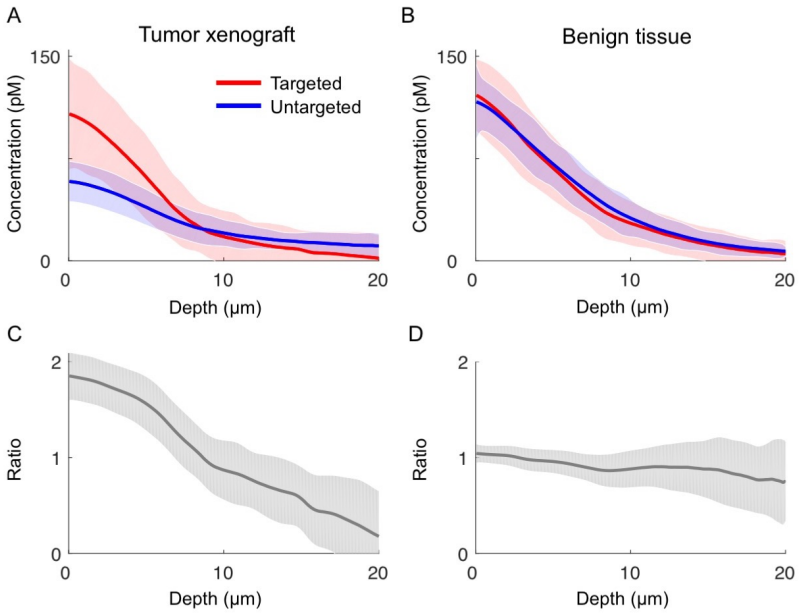

FIGURE 4.4: The average of approximately 1000 curves showing the concentration of targeted (red) and untargeted (blue) NPs as a function of depth from the tissue surface after the tumor xenografts (**A**) or benign tissues (**B**) were stained for 15 min. Shaded regions represent the standard deviation for approximately 1000 curves collected from n = 3 specimens of each tissue type. The concentration ratios of targeted vs. untargeted NPs as a function of depth are shown in (**C-D**) for tumor xenografts and benign tissues, respectively. Shaded regions represent the propagation of error from the shaded regions in A-B, respectively.

tuned such that total surface area of the NPs (total sum of the mixture) was identical to that of the 120-nm SERS NPs used in previous experiments (and reacted with the same concentration of fluorophores). To verify that this as true, we used a spectrofluorometer (Perkin Elmer, LS-50B) to show that the different NP sizes exhibited comparable levels of fluorescence for aliquots with identical total NP surface areas (Figure 4.5). Flow cytometry experiments were performed to verify that the binding of the targeted NPs to EGFR-positive cell lines was also comparable in magnitude for all NP sizes when staining cells with NP concentrations that were matched in terms of total NP surface area (Figure 4.6).

In order to improve their utility for time-constrained clinical applications (*e.g.*, surgical guidance), we endeavored to develop NPs that could yield adequate tumor-to-benign tissue contrast in less than 10 min (staining plus imaging time). Therefore, for these final sets of experiments, tumor xenografts were stained for just 6 min. We tuned the staining concentration, C_0, for each NP size to ensure that the total NP surface area (and binding avidity, see Figure 4.6) was relatively well-matched between all sets of experiments (C_0 = 150, 54, and 24 pM, respectively, for the 120-, 200-, and 300-nm

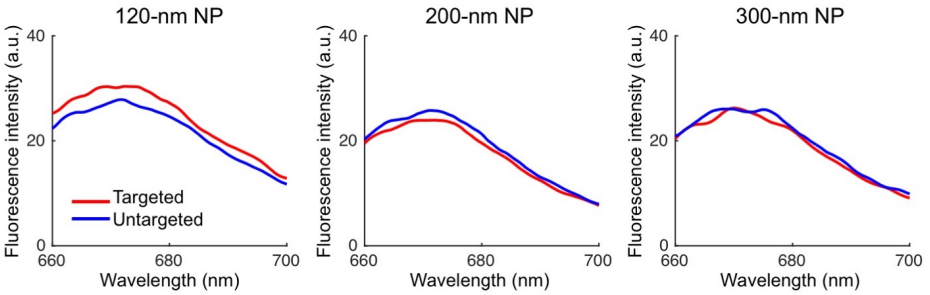

FIGURE 4.5: In order to ensure that the relative brightness of the fluorescence from each of the NP sizes was well-matched, the NP concentrations used in the conjugation reactions were tuned such that the total surface area of the NPs was identical to that of the 120-nm NPs used in previous experiments. Here, a spectrofluorometer was used to show that the different NP sizes exhibit comparable levels of fluorescence for aliquots with identical total NP surface areas. Background subtraction was applied using the fluorescence intensity of stock NPs that have not been reacted with fluorophores.

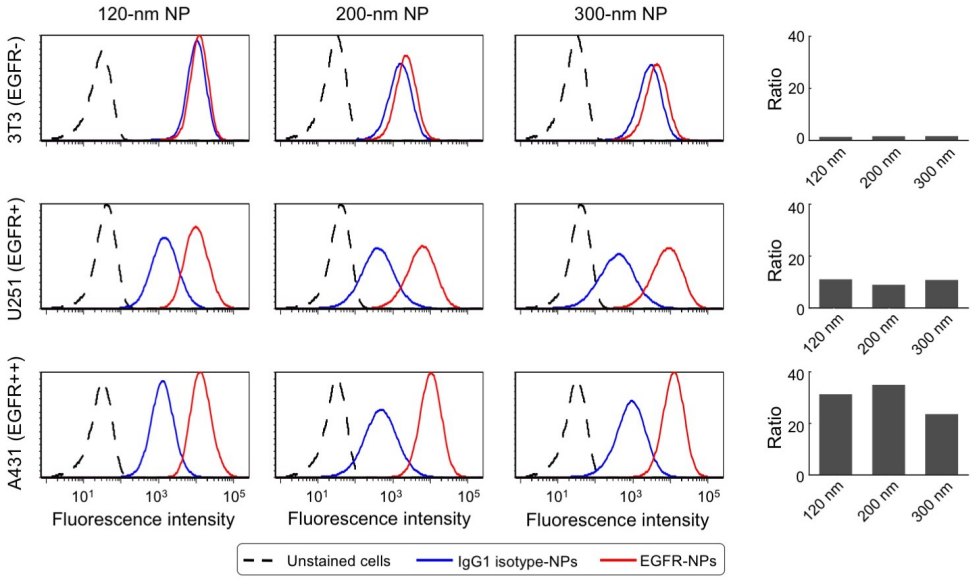

FIGURE 4.6: Flow cytometry validation of conjugated NPs of various sizes with cell lines of varying biomarker (EGFR) expression levels. Flow cytometry experiments were performed to verify that the binding of the EGFR-targeted NPs to EGFR-positive cell lines was comparable in magnitude for various NP sizes when staining cells with NP concentrations that were matched in terms of total NP surface areas. EGFR-NPs and isotype-NPs of various sizes were individually used to stain 3T3 (top row, EGFR-), U251 (middle row, EGFR+), or A431 (bottom row, EGFR++). The columns are separated by NP size (120-nm, 200-nm, and 300-nm in diameter). The fourth column shows the mean fluorescence intensity between the EGFR-targeted NP vs. untargeted NP to compare binding levels of the various NP sizes.

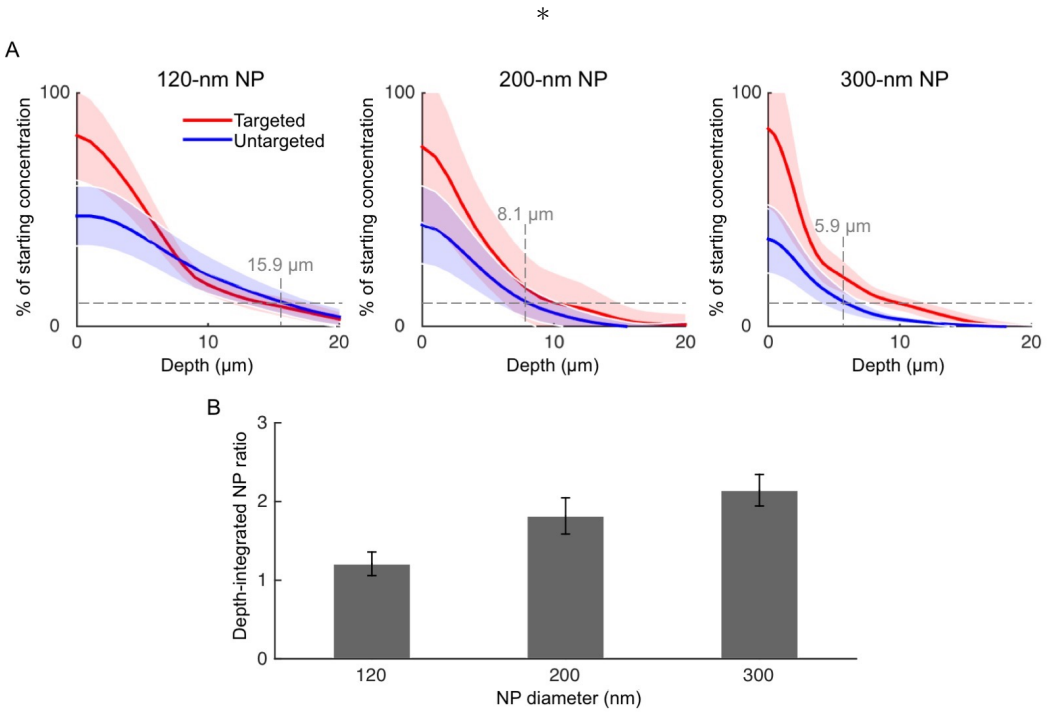

FIGURE 4.7: **Comparing micro-REMI for 3 different NP sizes.** Three different NP sizes were functionalized with either EGFR or isotype control mAbs. Tumor xenografts were stained with an equimolar mixture of targeted and untargeted NPs for 6 min, using either the 120-nm, 200-nm, or 300-nm diameter NPs. After staining, the specimens were rinsed briefly and snap-frozen for examination with the micro-REMI method. (**A**) The average of ∼1000 concentration curves are shown for the targeted NPs (red line) and untargeted NPs (blue line) as a function of depth for each NP size and are normalized to the initial staining concentration. The initial staining concentrations are different for each NP size to account for differences in the total surface area of the NPs (see text for details). Shaded regions represent the standard deviation for approximately 1000 curves collected from n = 5 specimens for each NP size. The grey dashed lines and grey text indicate the depth at which the concentration of the untargeted NP diminishes to 10% of the initial staining (starting) concentration. (**B**) The depth-integrated ratios (targeted vs. untargeted NPs) for each NP size. Error bars are based on n = 5 experiments for each NP size.

NPs). After staining, the specimens were rinsed briefly and snap-frozen according to the micro-REMI method illustrated in Figures 4.1 and 4.2. Figure 4.7 shows the average and standard deviation of ∼1000 micro-REMI concentration curves as a function of depth for each NP size. The depth at which the concentration of the untargeted NP diminished to 10% of the initial staining (starting) concentration is indicated in gray in Figure 4.7A. Figure 4.7B shows the depth-integrated ratio (the ratio of the integrated area under the 2 curves) for each NP size.

4.3 Discussion

This study explored the diffusion and chemical binding of NPs targeted to cell-surface proteins that were topically applied onto the surfaces of fresh tissues. With the REMI technology described in Chapter 2, fresh surgical specimens are topically stained with a panel of NPs and imaged after a brief rinse step to rapidly identify/quantify the presence of tumor-related biomarkers. Owing to uneven NP delivery/retention/rinse removal at different tissue locations, which often generates misleading image contrast, we utilize a control NP flavor that is co-administered with the targeted NP flavor(s) in an equimolar mixture during imaging experiments to normalize for nonspecific effects. While this NP ratio has been shown in previous studies to provide an accurate representation of biomarker expression levels, nonspecific accumulation and passive retention of NPs is often quite high, which reduces the sensitivity and accuracy of detection (*i.e.*, the ratios are lower than we would like).

Here, we have investigated the topical application of NPs on fresh tissue specimens at the microscopic level. We have developed a method to investigate the diffusion and accumulation of NPs near the tissue surface, a method we refer to as micro-REMI. We performed well-controlled "proof-of-concept" experiments using tumor xenografts with known biomarker receptor expression levels and uniform, reproducible tissue properties. We stained and rinsed these fresh tissue specimens with a paired-agent approach identical to that of our standard wide-area REMI approach, in which the targeted and untargeted NPs were labeled with different fluorescent dyes to allow thin frozen tissue sections to be imaged with a fluorescence microscope [110, 84, 93, 86, 85]. An image processing method was developed for analyzing the NP distributions (Figure 4.2). We verified that the depth-integrated concentrations (area under the curve) agreed with wide-area REMI signals by comparing ratios of targeted vs. untargeted NPs obtained with both methods (Figure 4.3). Analysis of NP concentration ratios as a function of depth (Figure 4.4) led us to hypothesize that by limiting the diffusion of NPs into tissue, higher NP ratios could be obtained with REMI, thereby improving tumor-to-benign tissue contrast and detection sensitivity. We tested this hypothesis using 200-nm and 300-nm silica NPs functionalized with the same concentration of mAbs (per NP surface area) as our standard 120-nm NPs. Figure 4.7 shows that larger NPs diffuse less into

tissue (Figure 4.7A), resulting in higher overall targeted vs. untargeted NP ratios (Figure 4.7B). Furthermore, we were able to achieve such high NP ratios in less time (6 min of staining) compared with our previous experiments that required 10 min or more of staining when utilizing our standard 120-nm NPs.

Previous studies on NP delivery have suggested that a "binding-site barrier", in which NP binding can impede NP penetration in tissue, may be preventing our targeted NPs from penetrating as deeply into tissues as our untargeted (control) NPs, which penetrate passively (unobstructed by a binding-site barrier) into the tissue [116, 120, 121, 122, 123]. This theory is supported by our experimental data in Figures 4.4A and 4.4C, where the ratio of the targeted vs. untargeted NPs dip below unity at the furthest depths within the tumor tissue. This suggests that our targeted and untargeted NPs are not being delivered identically, resulting in ratios that are less than ideal. Further studies are needed to verify that our experimental results are in fact attributable to a binding-site barrier effect. Results shown in Figure 4.7 indicate that the effects of this presumed "binding-site barrier" are mitigated with the use of larger NPs, in which both the targeted and untargeted NPs remain closer to the tissue surface. These results are consistent with the excellent staining performance of larger NPs witnessed by other investigators in the past [124].

In summary, the results of this study are significant in showing that larger NPs may be used in REMI to improve the ratio of targeted vs. untargeted NPs after a rapid staining protocol on fresh tissues. We note that while studies shown here employed the use of xenografts, further studies are needed to validate that higher ratios can be achieved with larger NPs on human tissues. This could potentially allow for better differentiation of tumor and benign tissues for clinical applications such as early detection and intraoperative assessments of surgical margins. Future clinical studies are also needed, with large numbers of patient specimens, to validate that these improvements are consistent across clinical cohorts. Note that we have already shown, in a recent clinical study, that REMI with 5 multiplexed SERS NP flavors (to target 4 cancer biomarkers) enables the detection of breast carcinoma with high sensitivity and specificity [125]. However, as we add more biomarker targets into our multiplexed panel, higher detection SNR and sensitivity will be needed (as well as faster staining times). We have shown through this study that it is possible to optimize the specific vs. nonspecific accumulation

of our targeted NPs, as well as staining speeds, based on an improved understanding of their behavior at the microscopic scale (micro-REMI).

Chapter 5

Mathematical modeling of NPs topically applied on fresh tissues to optimize staining and rinsing protocols

The optimization of staining, rinsing, imaging, and analysis protocols for REMI is costly in terms of time and resources. To help establish optimized protocols, we developed a compartmental model with binding and non-specific retention compartments that accurately represents the experimentally measured distribution of NPs topically applied on fresh tissue specimens. This model can be used to simulate realistic tumor contrast during defined tissue staining and rinsing protocols, which can help optimize a wide array of topical staining protocols. The complexity of such mathematical modeling approaches – which are affected by staining method, rinsing method, imaging frequency/timing, and data analysis algorithm – are nearly intractable to optimize experimentally. With sparse experimental feedback, an accurate data simulation model, as described here, can significantly enhance molecular imaging protocol optimization in REMI and contribute to the clinical translation of REMI to the intraoperative lumpectomy setting.

The mathematical model developed here is based on a system of partial and ordinary differential equations based on Fick's second law of diffusion and first-order binding kinetics, and includes both specific binding and nonspecific binding, as described in detail

the Methods section (5.1.1). To determine rate constants describing the binding and unbinding of NPs to cell surfaces, *in vitro* experiments were performed using confluent A431 cell monolayers stained with an equimolar mixture of targeted and untargeted NPs and imaged with the REMI system. The compartmental model was fit to concentration profiles obtained with micro-REMI, as described in Chapter 4. The predictive value of the model was demonstrated by simulating the concentration profiles of larger NPs, and was validated with micro-REMI data for larger NPs, as shown in Chapter 4. The work presented in this chapter has been developed with collaborators at the Illinois Institute of Technology (Professor Kenneth M. Tichaer and Xiaochun "Clover" Xu) and is to be submitted for publication with Xiaochun "Clover" Xu as a co-first-author.

5.1 Additional materials and methods

5.1.1 Model development

The characteristics of NP binding and diffusion were modeled based on a previous study describing drug penetration and binding in tumor spheroids that combined Fick's second law of diffusion with first-order kinetic binding [126]. The behavior of biomarker-targeted NPs topically applied on fresh tissues was modeled with three compartments, shown in Figure 5.1A. These include: 1) a specifically "bound" compartment, C_b, a "free" compartment, C_f, and a "nonspecific retention" compartment, C_{NS}, representing the concentration of NPs 1) bound to the targeted receptor, 2) unbound, free in the interstitial space, and 3) nonspecifically retained in the tissue, respectively. The untargeted (control) NP was model similarly with two compartments, and excluded the "bound" compartment. The equations representing targeted NPs were then written as:

$$\frac{\partial C_f}{\partial_t} = D\frac{\partial C_f}{\partial z^2} - k_3 C_f + k_4 C_b - k_5 C_f + k_6 C_{NS} \tag{5.1}$$

$$\frac{\partial C_{NS}}{\partial_t} = k_5 C_f - k_6 C_N S \tag{5.2}$$

$$\frac{\partial C_b}{\partial_t} = k_3 C_f - k_4 C_b \tag{5.3}$$

and the control imaging agent can be written as:

$$\frac{\partial C_f}{\partial_t} = D\frac{\partial C_f}{\partial z^2} - k_5 C_f + k_6 C_{NS} \tag{5.4}$$

$$\frac{\partial C_{NS}}{\partial_t} = k_5 C_f - k_6 C_N S \tag{5.5}$$

where the parameter, D, represents the diffusion coefficient; the rate constants, k_3 and k_4, govern association and disassociation of the targeted NP to the targeted receptor, respectively; and k_5 and k_6 govern nonspecific association and disassociation of both NPs, respectively. These equations are represented as compartment models in Figure 5.1 with diffusion connecting each layer of a conventional compartmental model indicating layers of tissues in depth. The solution to these equations provides concentration profiles of targeted and untargeted NPs for various staining/rinsing/imaging conditions.

Equations 5.1-5.5 were solved using a numerical solver for parabolic partial differential equation systems based on a Crank-Nicholson approach, which discretizes space and time in a grid. This Crank-Nicholson method is an implicit finite difference method, which is considered conditionally stable under the condition:

$$\frac{Dt_{stain}n_z^2}{n_t L^2} < 0.5 \tag{5.6}$$

where t_{stain} is the duration of the staining (or rinsing), n_z is the number of elements in depth, L is the tissue thickness (maximum depth) in the simulation, and n_t is the number of time points the solution is evaluated at. In this way, the tissue was modeled as a 1-dimensional vector in depth (Figure 5.2A) that changes as a function of staining duration (Figure 5.2B). Even though the NP diffusion is strictly 3-dimensional, spatially, a one-dimensional assumption was assumed for computational efficiency since the penetration depth (<20 μm) of the NPs used for testing was far smaller than the interface between the tissue and the staining solution (>5 mm). The boundary condition of the unbound NP concentration at the tissue surface was set to be Dirichlet, 1^{st}-kind, equal to the concentration of imaging agents in the staining or rinsing solution. The boundary condition at large depths (*e.g.* 100 μm, which far exceeds the depth reached by the NPs

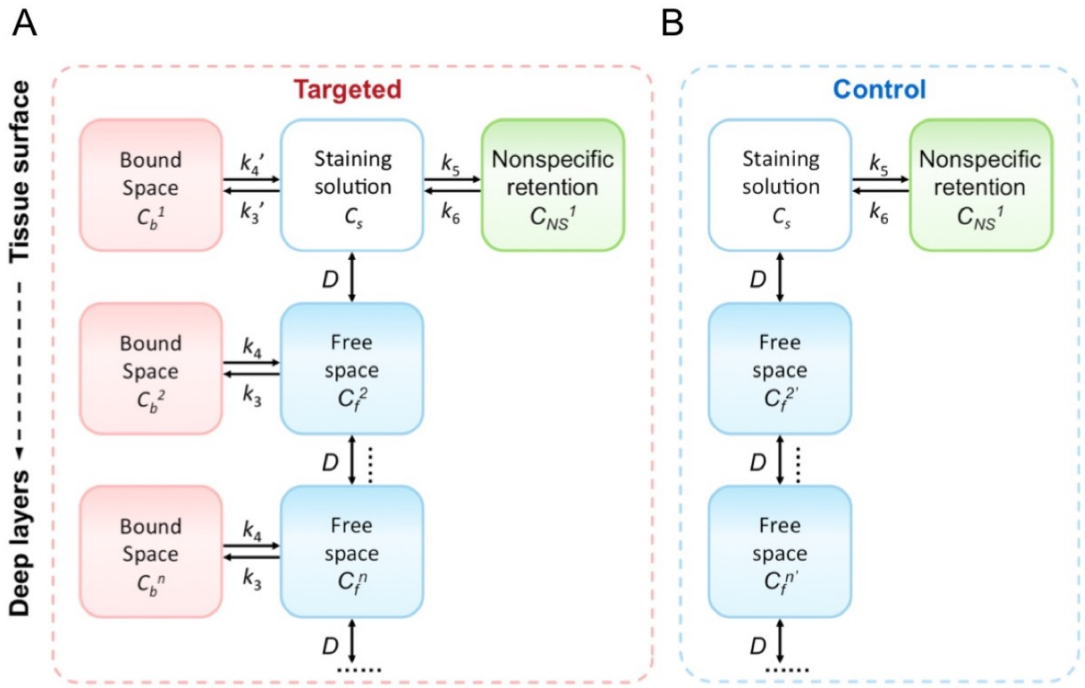

FIGURE 5.1: **A three-compartment model with diffusion representing the distribution of a targeted imaging agent (A) and a two-compartment model representing a control imaging agent (B) in each layer of thick tissue.** Each level consists of the "free" space concentration of both agents (unbound NPs in the tissue/medium), C_f, the "nonspecific" retention concentration of both NPs, C_{NS}, and the "bound" space concentration (concentration of targeted NPs bound to the targeted receptor), C_b, of the targeted NP. The rate constants, k_3 and k_4, govern association and dissociation of the targeted NP to/from the target, respectively; the rate constants, k_5 and k_6, govern transport between the free and nonspecific compartment for both NPs, respectively; and D represents the diffusion coefficient, and the bidirectional arrows are not strictly representative of first order kinetics.

experimentally) was set to be Cauchy, 2^{nd}-kind, with the spatial derivative of the free NP concentration set to zero.

5.1.2 *In vitro* experiments

For *in vitro* experiments, a previously published protocol was used [127]. Briefly, a 96-well plate with a 200 μm-thick glass bottom was used to culture cells into monolayers. Cells were counted and seeded into wells (1×10^5 A431 cells in 200 μL of media per well). After incubation for 24 hours, confluent cell monolayers were observed in all wells. For Raman measurements, one of the wells was used to acquire a background measurement in the absence of NPs. For the remaining wells, an equimolar mixture of EGFR-targeted and isotype-control untargeted NPs was added for staining the confluent monolayers. Concentrations and staining times varied depending on the experiment condition. The

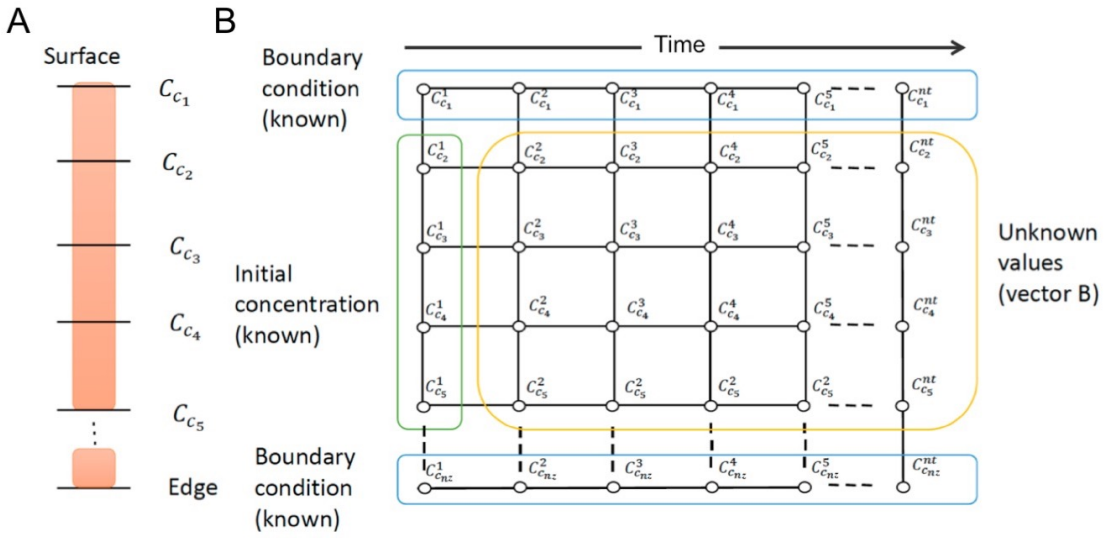

FIGURE 5.2: **Illustration of the Crank-Nicholson implementation for tissue staining.** (**A**) Illustration of tissue vector and its values C_{C_n} at each point. The surface value C_{C_1} is set to be constant, staining solution concentration. The spatial derivative at the lower boundary condition is set to be equal to zero. (**B**) Illustration of the discretized space and time in matrix. The blue boxes indicate the boundary condition, same as the definition in (A). The green box indicates the initial condition of tissue, defined as zeros before staining. The yellow box indicates the unknown values to be calculated.

staining procedure was followed by 3 rounds of rinsing with PBS. Spectral measurements were collected after the final rinse step using the REMI system.

5.1.3 Determination of rate constants

In order to determine rate constants from the *in vitro* experiments, an approximate model for a single cell that binds and internalizes particles was applied [128]. In this study, we assumed that the NPs are too large (120-nm in diameter) to be internalized by the cell for short staining durations (<1 hr), so we excluded the internalization component to the model. The approximate model equations representing single cell interactions with NPs were then written as:

$$\frac{dN_b}{d_t} = k_a C_0 N_{bs} - k_d N_b \tag{5.7}$$

$$N_{bs} = B - N_b \tag{5.8}$$

where $N_b(t)$ is the number of NPs bound at the cell surface as a function of time, t; $N_{bs}(t)$ and B are the current and initial numbers of available binding sites, respectively; k_a is the association (binding) rate constant; k_d is the dissociation rate constant; and C_0 is the initial staining concentration. Solving these equations gave the number of bound particles as a function of time and initial staining concentration, which were then used to determine the rate coefficients and the binding site number from experimental data:

$$N_b = \frac{k_a C_0 B}{k_a C_0 + k_d} \left(1 - e^{-(k_a C_0 + k_d)t}\right) \tag{5.9}$$

With confluent monolayers it was assumed that the exposed surface area of cell membrane was equal to the area of the well, allowing calculation of the number of NPs bound per unit cell membrane area. The average surface area per cell (assumed to be 2800 μm^2 for A431 cells based on [129, 130]) was used to convert the number of NPs bound per unit cell area to the number of NPs bound per cell. The equation solving for N_b was fit to the data of NPs bound as a function of staining concentration to derive an estimate for the parameter B. For this solution, t was assumed to be infinite since binding had reached saturation and the unknown rate constants (k_a and k_d) were considered in terms of an equilibrium constant, $K = k_a/k_d$, allowing for a nonlinear least squares fit to the data. The association and dissociation rate constants were then determined by exposing confluent monolayers to an equimolar mixture of targeted and untargeted NPs (150 pM) and measuring the number of NPs bound per cell as a function of time. Using the number of binding sites per cell, B, the analytical solution of N_b (Equation 5.9) was fit to these data points (measured NPs bound per cell as a function of time) using nonlinear least squares fitting.

5.2 Results

To solve for the parameters, k_3, k_4, k_5, and k_6, of the compartmental model we first solved Equation 5.9 for B, k_a, and k_d. We considered the *specific* binding and dissociation of targeted NPs to biomarker targets, k_3 and k_4, respectively, to be representative of the k_a and k_d determined with *in vitro* experiments for the targeted NP. Similarly, the *nonspecific* accumulation and removal of NPs from tissue, k_5 and k_6, respectively, were representative of the k_a and k_d determined with *in vitro* experiments for the untargeted

NP. Proceeding with the solution to Equation 5.9, we first determined the total number of nonspecific binding sites per A431 cell, B, by exposing a confluent monolayer of A431 cells to untargeted NPs of various concentrations for 1 hr. The average cell surface area, used to determine the number of NPs bound per cell, was calculated using an average surface area of 2800 μm^2 [129, 130] per cell based on measurements obtained with the Raman imaging device. The experimental method is illustrated in Figure 5.3A, and the results are shown in Figure 5.3B, where the number of NPs bound per cell is shown as a function of the NP staining concentration. A nonlinear least squares fit of Equation 5.9 to the data showed that binding reached a maximum of approximately $85 \times 10^3 \pm 30 \times 10^3$ NPs/cell, which results in an effective cell surface coverage of ~40%. The association and dissociation rate constants of NPs binding to A431 cells specifically (k_3 and k_4, respectively) and nonspecifically (k_5 and k_6, respectively) were determined by calculating the number of NPs bound per cell as a function of time (cell monolayers were stained with a fixed concentration of 150 pM per NP flavor). Equation 5.9 was again fit to data from the time course study using a nonlinear least squares algorithm in order to obtain a range for estimating the association and dissociation constants for NPs binding specifically and nonspecifically to cell receptors. The estimated range of k_3 was 1.7 to 7.5 μM-s^{-1}, k_4 was 3.4×10^{-4} to 9.0×10^{-4} s^{-1}, k_5 was 1.6 to 7.4 μM-s^{-1}, and k_6 was 6.2×10^{-4} to 14.0×10^{-4} s^{-1}. These results suggest that both targeted and untargeted NPs bind at similar rates, and any differences in the ratio of targeted vs. untargeted NPs are due differences in the dissociation rate constants, k_4 and k_6. That is, the untargeted NPs dissociate from the cell surface at a faster rate than the targeted NP.

To demonstrate the accuracy of the mathematical model developed in Section 5.1.1, we compared this latest model with a simpler version described previously [127], in which binding and diffusion were included but not nonspecific retention. Here on out, Model 1 refers to the older, simpler model without the nonspecific retention compartment, while Model 2 refers to the latest model as described in Section 5.1.1 and shown in Figure 5.1. The parameter estimates determined from Figure 5.3 were used to fit Model 1 and Model 2 to concentration profiles obtained experimentally from A431 tumor xenografts stained for 6-min with targeted and untargeted NPs. In running the least-squares fitting algorithm, the parameters were allowed to vary within an order of magnitude around the best-fit value from Figure 5.3. Figure 5.4A shows a brief illustration of the micro-REMI

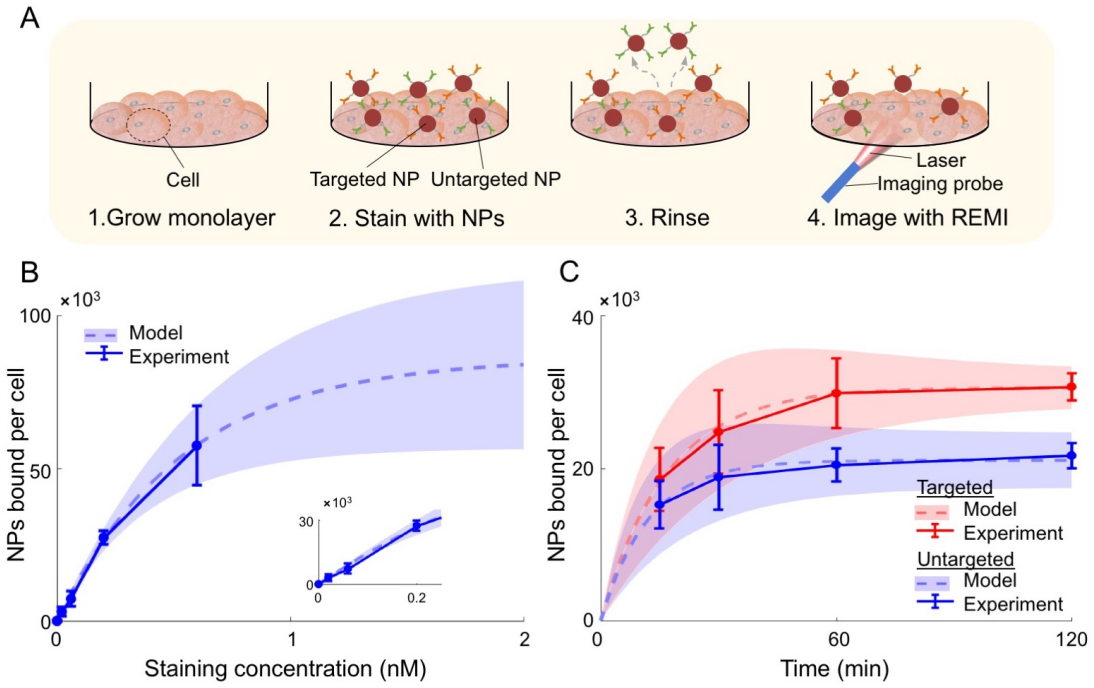

FIGURE 5.3: ***In vitro* experiments for experimentally determining model parameters.** (**A**) An illustration of the experimental method for a single well in a 96-well plate with a 200 μm-thick glass bottom. For each well, A431 cells were (1) grown to a confluent monolayer (∼24 hr), (2) the cell monolayer was stained with NPs, (3) the cell monolayer was rinsed three times to wash away unbound NPs, and (4) spectral measurements were collected with REMI. The measured SERS signals were converted to NPs bound per cell using the calculations described in the Methods section. Note that the figure is not to scale. (**B-C**) Experimental data (dots with error bars based on n = 3 repeated experiments) and fitted curves (dashed lines) for determination of (**B**) the available number of nonspecific binding sites, B, and (**C**) the association and dissociation rate constants for targeted (red) and untargeted (blue) NPs. The shaded regions indicate the propagation of uncertainty in the fitted model based on the error in the experimental data. The fitted curves for determination of final values were obtained using Equation 5.9. The staining time for (B) was 1 hr and the staining concentration for (C) was 150 pM. Note that the available number of nonspecific binding sites (B) was only determined using untargeted NPs.

method described in Chapter 3 (the depth-resolved microscopic imaging of sectioned tissues), which was used to fit the models. First, an equimolar mixture of targeted and untargeted NPs, each reacted with a different fluorophore, was used to stain a fresh tissue specimen. The tissue was then frozen and cryosectioned into 10-μm sections for fluorescence microscopy. The concentration profiles of the experimental data are shown in Figures 5.4B-C in solid lines for targeted (red) and untargeted (blue) NPs. The fitted curves for Model 1 and Model 2 are shown in dashed lines in Figures 5.4B-C, respectively. Figure 5.4D shows that the percent error in concentration profiles is increasing as a function of depth for both models, with Model 1 showing greater percent error altogether compared to Model 2.

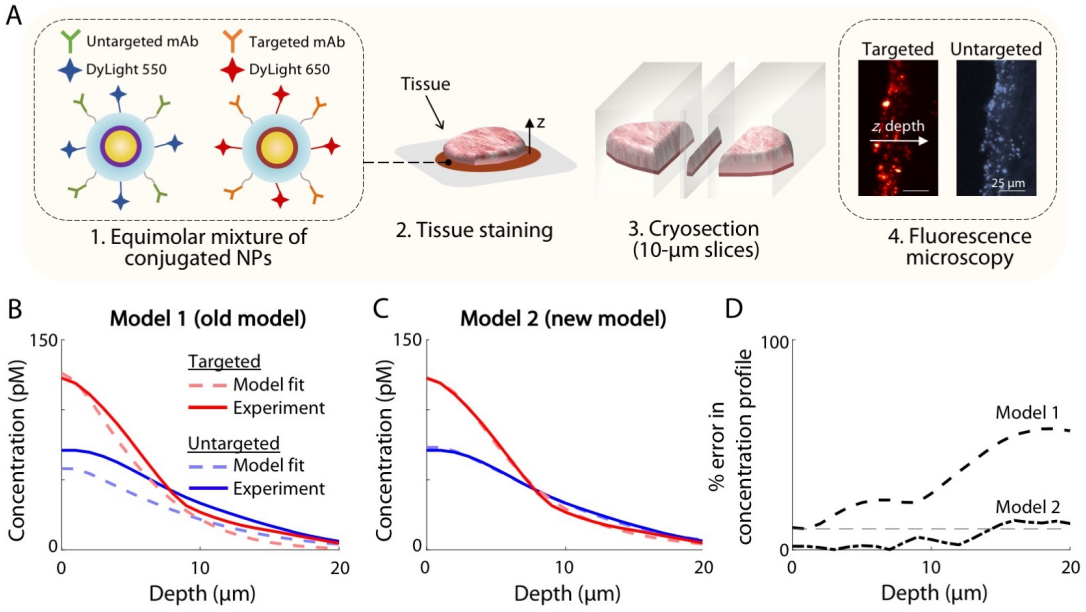

FIGURE 5.4: **Fitting Model 1 and Model 2 to depth-resolved microscopic images of sectioned tissues (micro-REMI).** (**A**) A brief illustration of the experimental method used to fit Model 1 and Model 2. (1) Targeted and untargeted NPs were prepared by conjugating NPs to monoclonal antibodies and different fluorophores. (2) Fresh tissue specimens were stained for 6-min with an equimolar NP mixture, rinsed and snap-frozen. (3) The specimens were then cryosectioned into 10 μm-thick slices and (4) imaged with fluorescence microscopy using two different channels to collect the signals from targeted and untargeted NPs. Images were analyzed for obtaining concentration profiles of both NPs as a function of depth, z, as NPs diffuse into tissue. (**B-C**) Experimental results of NP concentration profiles are shown in solid lines for targeted (red) and untargeted (blue) NPs, which were used to fit model parameters from (B) the simpler Model 1 (no nonspecific retention compartment) and (C) the more complex Model 2 based on the parameter ranges determined experimentally in Figure 5.3. (**D**) The percent error in concentration profile is shown increasing as a function of depth for both models, with Model 1 showing greater percent error altogether compared to Model 2.

We further demonstrated the value of Model 2 by simulating the concentration profiles of larger NPs by modifying the diffusion coefficient, D, according to the Stokes-Einstein generalized equation (in which D scales inversely with the radius of the NP) while fixing all other model parameters to the same values as determined in previous experiments for the 120-nm NPs. To verify the accuracy of model simulations for larger NPs, 200-nm and 300-nm NPs were prepared in an identical manner as the 120-nm NPs used in previous studies, according to a previously published protocol [127], and concentration profiles were obtained for A431 tumor xenografts stained 6-min with these larger NPs. Figure 5.5 shows model predictions in dashed lines and experimental results in solid lines for targeted (red) and untargeted (blue) NPs for (A) 200-nm and (B) 300-nm NPs. The percent errors between model predictions and experimental data are shown in

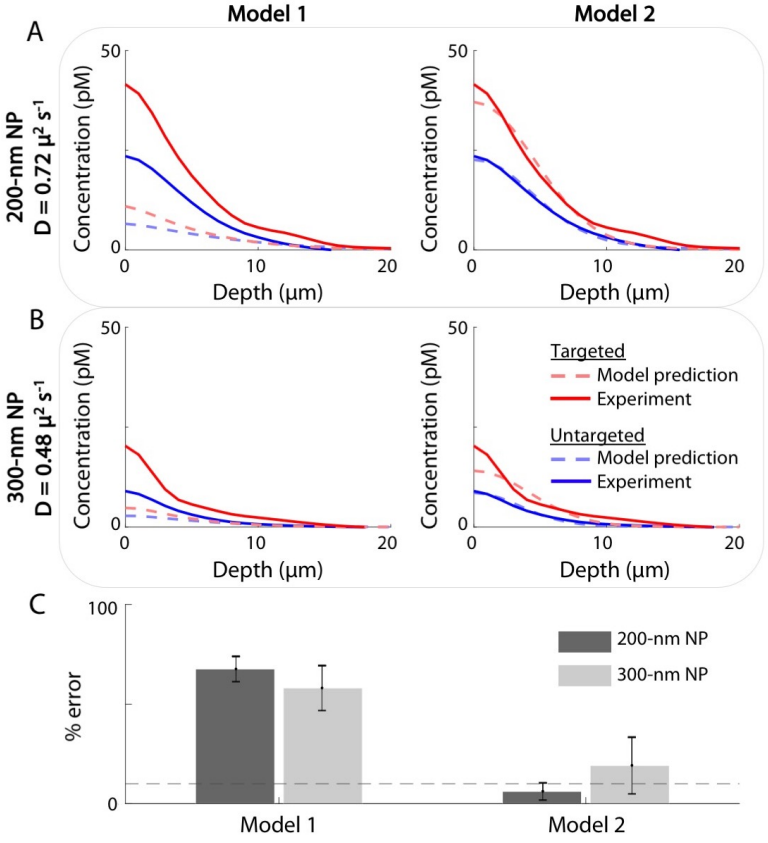

FIGURE 5.5: **Simulations of Model 1 (left) and Model 2 (right) predicting the concentration profiles of (A) 200-nm and (B) 300-nm NPs.** The models were executed with all identical parameters as those fitted in Figure 5.4, with the exception of the diffusion coefficient, D, which was modified according to the Stokes-Einstein generalized equation (in which D scales inversely with the radius of the NP). Model predictions are shown in dashed lines for targeted (red) and untargeted (blue) NPs. Experimental data is shown in solid lines and was obtained from A431 tumor xenograft tissue stained for 6-min with NPs of varying sizes. The percent errors between model predictions and experimental data are shown in (C). The dashed grey line indicates 10% error.

Figure 5.5C, where Model 1 shows ∼70% error and Model 2 shows ∼15% error, thereby demonstrating the predictive power of Model 2 in simulating experimental conditions for topically applied biomarker-targeted NPs on fresh tissue specimens.

5.3 Discussion

This study aimed to develop a compartmental model with binding and nonspecific retention compartments to accurately simulate concentration profiles of topically-applied NPs to fresh tissue surfaces. (Figure 5.1). The model was based on a system of partial and ordinary differential equations based on Fick's second law of diffusion and first-order

binding kinetics (Figure 5.1), and was solved using the Crank-Nicholson method, a conditionally stable finite difference method (Figure 5.2). Rate constants were estimated with *in vitro* experiments using confluent monolayers of A431 cells stained with an equimolar mixture of targeted and untargeted NPs (Figure 5.3). We note that while experimentation with cell monolayers is not representative of true tissue micro-environment (*e.g.* due to differences in access to cell-surface targets, nonspecific accumulation in tissues, etc.), this method allows us to narrow the range of parameter limits that can be used in the fitting of the compartmental model to experimental micro-REMI data. This parameter range was first used to show that the more complex Model 2, which includes a nonspecific retention compartment at the surface, accurately represents the binding and diffusion of 120-nm NPs topically applied on fresh tissues (Figure 5.4). Model 2 was further validated experimentally by showing that it can predict the behavior of different sizes of NPs (200 and 300 nm in diameter) used to stain EGFR-positive tumor xenografts (Figure 5.5). By accurately simulating the behavior of topically-applied NPs to fresh tissue surfaces, the model can be used to guide the selection of contrast agent and protocols to perform topical staining, that would optimize cancer detection.

One noteworthy finding from this study was that both targeted and untargeted NPs bind to receptors specifically and nonspecifically at similar rates, and any contrast in targeted vs. untargeted NP ratios is due to differences in the dissociation rate constants. That is, untargeted NPs that have attached nonspecifically to cell surface receptors dissociate from cell surfaces at a faster rate than that of targeted NPs. We note that the compartmental model developed in this chapter is highly simplified and does not include such complexities as NP trapping in fresh tissue and heterogeneities in tissue structure (*i.e.* due to microvasculature and tissue cutting artifacts). Incorporating such complexities into the model would add a large number of parameters to the fitting procedure, ultimately leading to challenges in converging to a solution. Regardless, the work shown in this chapter demonstrated that this mathetmatical model that incorporates multi-layer diffusion, in addition to binding and nonspecific retention compartments, accurately simulates the contrast provided by targeted and untargeted NPs topically applied on tissues. As an accurate "forward" model to generate concentration profiles of targeted and untargeted NPs, this will be of value in developing and optimizing various NP-based imaging methods, for the ultimate goal of enabling quantitative and reproducible imaging of biomarker expression levels. This, in turn, will be of value for many

clinical applications, such as patient stratification to guide personalized therapies or to monitor treatment outcomes.

Chapter 6

Conclusion and future work

The work presented in this thesis offers strategies for improving a previously-described Raman-encoded molecular imaging (REMI) technique, which utilizes the topical application of multiplexed SERS NPs for rapid visualization of multiple cell-surface biomarkers at the surfaces of fresh tissues. While it has been demonstrated that REMI may potentially be used to guide tumor-resection procedures [93, 83, 86, 125, 85, 110], there are clear opportunities to further improve the strategy for clinical translation (*e.g.*, speed, accuracy, imaging contrast, biomarker detection sensitivity, and quantitative analysis).

In Chapter 3, a feasibility study using channel-compressed spectrometry was presented as a means to potentially improve the speed and/or sensitivity of REMI. Results showed that a very high degree of channel compression (nearly two orders of magnitude reduced from the original 1024 channels) can still allow for accurate and highly multiplexed ratiometric imaging of biomarkers with targeted SERS NPs. This opened up the possibility to use advanced detector arrays, such as 16-channel or 32-channel PMT or APD arrays, which are much more sensitive and fast compared to a 1024-channel spectroscopic CCD array. Future studies will develop and assess the ability of a high-speed and high-resolution REMI system for a variety of clinical applications including intraoperative guidance of tumor resection and multiplexed molecular endoscopy of the gastrointestinal tract [106, 84, 93, 85, 114], in which imaging speed and imaging resolution are of importance.

In Chapter 4, a method to investigate the binding and diffusion of topically applied NPs at the microscopic level was developed (a method termed "micro-REMI") and

validated with time-resolved wide-area REMI experiments using topically applied SERS NPs on fresh tissue specimens stained for various durations. Analysis of targeted vs. untargeted NP concentration ratios as a function of depth led us to hypothesize that by limiting the diffusion of NPs into tissue, higher NP ratios could be obtained with REMI, thereby improving tumor-to-benign tissue contrast and detection sensitivity. We tested this hypothesis using 200-nm and 300-nm silica NPs functionalized with the same concentration of mAbs (per NP surface area) as our standard 120-nm NPs in which the larger NPs diffuse less into tissue, resulting in higher overall targeted vs. untargeted NP ratios, and in less time (6-min of staining) compared with our previous experiments that required 10-min or more of staining when utilizing our standard 120-nm NPs. The results of this study are significant in showing that larger NPs may be used in REMI to improve the ratio of targeted vs. untargeted NPs after a rapid staining protocol on fresh tissues. We note that while studies shown here employed the use of xenografts, further studies are needed to validate that higher ratios can be achieved with larger NPs on human tissues. This could potentially allow for better differentiation of tumor and benign tissues for clinical applications, such as early detection and intraoperative assessments of surgical margins.

In Chapter 5, we developed a mathematical model to simulate the binding and diffusion of NPs topically applied on fresh tissue surfaces. The model parameters (NP diffusion coefficient and the rate constants for binding and unbinding of targeted and untargeted NPs to targeted and nonspecific binding sites) were determined by *in vitro* experiments. We showed with this model accurately represents the binding and diffusion of 120-nm NPs topically applied on fresh tissues. We further demonstrated the predictive power of this model by simulating the behavior of larger NPs (200-nm and 300-nm) as they are topically applied to fresh tisues and validating this experimentally with EGFR-positive tumor xenografts. As an accurate "forward" model to generate concentration profiles of targeted and untargeted NPs, this will be of value in developing and optimizing various NP-based imaging methods, for the ultimate goal of enabling quantitative and reproducible imaging of biomarker expression levels. This, in turn, will be of value for many clinical applications, such as patient stratification to guide personalized therapies or to monitor treatment outcomes.

6.1 Future work

We note that additional work is neccesssary to further promote REMI for surgical guidance. This section presents some of these directions.

Brighter NPs would help to improve contrast (signal to background ratios), detection sensitivities, spatial resolution, and imaging speeds. The relative weakness of SERS NP signals limits spectral acquisition rates and scanning speeds, which in turn limits the ability to scan large areas with high spatial resolution (*i.e.* imaging with large pixel counts. Recently, surface-enhanced resonance Raman scattering (SERRS) nanostars have been reported to exhibit significantly enhanced brightness (compared to non-resonant SERS NPs) by using Raman dyes with absorption maxima matched with NIR light sources and a high affinity for gold surfaces [69, 131], which enabled the detection of small cancer-cell clusters with microscopic resolution [89, 69, 132]. Further work is necessary, however, to characterize and improve the stability of SERRS NPs for biomarker-targeted clinical imaging applications.

Another potential challenge is that cauterization of tissues may denature proteins, including the biomarkers targeted by SERS NPs. Note that cautery, used by many but not all surgeons, is also a challenge for conventional pathology, where it has been observed that certain protein targets and epitopes are more adversely affected than others. A major advantage of SERS NPs is their potential to simultaneously image a large panel of biomarkers (potentially 5 to 10 [79]), which may mitigate the effects of cautery since certain biomarkers have been shown to be less affected by cauterization damage [133]. Future studies will examine the effects of surgical cautery on the performance of intraoperative REMI.

Ensuring high specificity of tumor detection is of primary importance (to avoid over-excision) while sensitivity is secondary (since post-operative pathology will still be employed). The five candidate biomarkers used in previous REMI studies (HER2, EGFR, CD44, CD24, mER) [125] are expressed in >85% of breast cancers (on average, assuming independent statistics) [134, 135, 136, 137, 138, 139, 140, 141]. Nevertheless, future studies will aim to improve the detection sensitivity by enabling targeting of additional cancer biomarkers, such as integrins [142, 143, 144], cell-surface growth-factor receptors (*e.g.* VEGFR1, VEGFR2 [145, 146, 147], PDGFRα, and PDGFRβ [148, 149, 150],

MUC1 [151, 152], EpCAM, [153, 154, 155], and Ki67 [156, 157]). Thus, future work is needed to demonstrate the ability to quantify a larger panel of biomarkers with targeted SERS NPs, which will require additional optimization of the targeted SERS NPs themselves, as well as the detection hardware and tissue-staining, rinsing, and imaging protocols.

In summary, multiplexed molecular imaging, as enabled by REMI, has value for the rapid imaging of large, excised specimens (4 cm^2) under time-constrained intraoperative conditions with sub-millimeter resolution for the detection of small residual tumors. The studies presented in this dissertation contribute to the clinical translation of REMI to intraoperative settings. With improvements in speed, accuracy, imaging contrast, biomarker detection sensitivity, and quantitative analysis, there is potential for REMI to accurately detect residual tumors at surgical margins, with an ultimate goal of improving patient care by reducing the rate of re-excision surgeries associated with breast-cancer lumpectomy.

Bibliography

[1] C. Desantis, J. Ma, L. Bryan, and A. Jemal, "Breast Cancer Statistics, 2013," *CA: A Cancer Journal for Clinicians*, vol. 64, pp. 52–62, 2014.

[2] L. Jacobs, "Positive margins: the challenge continues for breast surgeons.," *Annals of Surgical Oncology*, vol. 15, no. 5, pp. 1271–1272, 2008.

[3] M. S. Moran, S. J. Schnitt, A. E. Giuliano, J. R. Harris, S. A. Khan, J. Horton, S. Klimberg, M. Chavez-macgregor, G. Freedman, N. Houssami, and P. L. Johnson, "Society of Surgical Oncology – American Society for Radiation Oncology Consensus Guideline on Margins for Breast-Conserving Surgery With Whole-Breast Irradiation in Stages I and II Invasive Breast Cancer," *Journal of Clinical Oncology*, vol. 32, no. 14, pp. 0–9, 2014.

[4] J. C. Cendán, D. Coco, and E. M. C. Iii, "Accuracy of Intraoperative Frozen-Section Analysis of Breast Cancer Lumpectomy-Bed Margins," *Journal of the American College of Surgeons*, vol. 201, no. 2, pp. 194–198, 2005.

[5] J. M. Jorns, D. Visscher, M. Sabel, T. Breslin, P. Healy, S. Daignaut, J. L. Myers, and A. Wu, "Intraoperative frozen section analysis of margins in breast conserving surgery significantly decreases reoperative rates: one year experience at an ambulatory surgical center," *American journal of clinical pathology*, vol. 138, no. 5, pp. 657–669, 2012.

[6] J. A. Ferreiro, J. J. Gisvold, and D. G. Bostwick, "Accuracy of frozen-section diagnosis of mammographically directed breast biopsies," *American Journal of Surgical Pathology*, vol. 19, no. 11, pp. 1267–1271, 1995.

[7] T. S. Menes, P. I. Tartter, H. Mizrachi, S. R. Smith, and A. Estabrook, "Touch Preparation or Frozen Section for Intraoperative Detection of Sentinel Lymph

Node Metastases From Breast Cancer," *Journal of Surgical Oncology*, vol. 10, no. 10, pp. 1166–1170, 2003.

[8] F. D'Halluin, P. Tas, S. Rouquette, C. Bendavid, F. Foucher, H. Meshba, J. Blanchot, O. Coue, and J. Leveque, "Intra-operative touch preparation cytology following lumpectomy for breast cancer : A series of 400 procedures," *The Breast*, vol. 18, pp. 248–253, 2009.

[9] C. E. Cox, N. N. Ku, D. S. Reintgen, M. Harvey, S. V. Nicosia, and S. Wangensteen, "Touch Preparation Cytology of Breast Lumpectomy Margins With Histologic Correlation," *Arch Surg*, vol. 126, no. 4, pp. 490–493, 1991.

[10] V. S. Klimberg, K. C. Westbrook, and S. Korourian, "Use of Touch Preps for Diagnosis and Evaluation of Surgical Margins in Breast Cancer," *Annals of surgical oncology*, vol. 5, no. 3, pp. 220–226, 1998.

[11] A. O. Saarela, T. K. Paloneva, T. J. Rissanen, and H. O. Kiviniemi, "Determinants of positive histologic margins and residual tumor after lumpectomy for early breast cancer: A prospective study with special reference to touch preparation cytology," *Journal of Surgical Oncology*, vol. 66, no. 4, pp. 248–253, 1997.

[12] E. K. Valdes, S. K. Boolbol, J. M. Cohen, and S. M. Feldman, "Intra-operative touch preparation cytology; does it have a role in re-excision lumpectomy?," *Annals of surgical oncology*, vol. 14, no. 3, pp. 1045–1050, 2007.

[13] A. B. Chagpar, M. Butler, B. K. Killelea, N. R. Horowitz, K. Stavris, and D. R. Lannin, "Does three-dimensional intraoperative specimen imaging reduce the need for re-excision in breast cancer patients ? A prospective cohort study," *The American Journal of Surgery*, vol. 210, no. 5, pp. 886–890, 2015.

[14] M. Lange, T. Reimer, S. Hartmann, A. Glass, and A. Stachs, "The role of specimen radiography in breast-conserving therapy of ductal carcinoma in situ," *The Breast*, vol. 26, pp. 73–79, 2016.

[15] T. M. Allweis, Z. Kaufman, S. Lelcuk, I. Pappo, T. Karni, S. Schneebaum, R. Spector, A. Schindel, D. Hershko, M. Zilberman, J. Sayfan, Y. Berlin, A. Hadary, O. Olsha, H. Paran, M. Gutman, and M. Carmon, "A prospective , randomized , controlled , multicenter study of a real-time , intraoperative probe for positive

margin detection in breast-conserving surgery," *The American Journal of Surgery*, vol. 196, pp. 483–489, 2008.

[16] T. Karni, I. Pappo, J. Sandbank, O. Lavon, V. Kent, R. Spector, S. Morgenstern, and S. Lelcuk, "A device for real-time , intraoperative margin assessment in breast-conservation surgery," *The American Journal of Surgery*, vol. 194, pp. 467–473, 2007.

[17] F. Schnabel, S. K. Boolbol, M. Gittleman, T. Karni, L. Tafra, S. Feldman, A. Police, N. B. Friedman, S. Karlan, D. Holmes, S. C. Willey, M. Carmon, K. Fernandez, S. Akbari, J. Harness, L. Guerra, T. Frazier, K. Lane, R. M. Simmons, A. Estabrook, and T. Allweis, "A Randomized Prospective Study of Lumpectomy Margin Assessment with Use of MarginProbe in Patients with Nonpalpable Breast Malignancies," *Annals of surgical oncology*, vol. 21, pp. 1589–1595, 2014.

[18] B. K. Chan, J. A. Wiseberg-Firtell, R. H. Jois, K. Jensen, and R. A. Audisio, "Localization techniques for guided surgical excision of non- palpable breast lesions (Review)," *Cochrane Database of Systematic Reviews*, vol. 12, 2015.

[19] T. Ihrai, D. Quaranta, Y. Fouche, J. Machiavello, I. Raoust, C. Chapellier, C. Maestro, M. Marcy, J.-M. Ferrero, and B. Flipo, "Intraoperative radiological margin assessment in breast-conserving surgery," *European Journal of Surgical Oncology*, vol. 40, pp. 449–453, 2014.

[20] S. Abeytunge, B. Larson, G. Peterson, M. Morrow, M. Rajadhyaksha, and M. P. Murray, "Evaluation of breast tissue with confocal strip-mosaicking microscopy : a test approach emulating pathology- like examination strip-mosaicking microscopy : a test approach," *Journal of biomedical optics*, vol. 22, no. 3, pp. 034002–1–11, 2017.

[21] J. L. Dobbs, H. Ding, A. P. Benveniste, H. M. Kuerer, S. Krishnamurthy, W. Yang, and R. Richards-Kortum, "Feasibility of confocal fluorescence microscopy for real-time evaluation of neoplasia in fresh human breast tissue," *Journal of Biomedical Optics*, vol. 18, no. 10, p. 106016, 2013.

[22] E. F. Brachtel, N. B. Johnson, A. E. Huck, T. L. Rice-stitt, G. Mark, B. L. Smith, G. J. Tearney, and D. Kang, "Spectrally encoded confocal microscopy (SECM)

for diagnosing of breast cancer in excision and margin specimens," *Lab Invest.*, vol. 96, no. 4, pp. 459–467, 2016.

[23] Y. K. Tao, D. Shen, Y. Sheikine, O. O. Ahsen, H. H. Wang, D. B. Schmolze, N. B. Johnson, J. S. Brooker, A. E. Cable, J. L. Connolly, and J. G. Fujimoto, "Assessment of breast pathologies using nonlinear microscopy," *Proceedings of the National Academy of Sciences*, vol. 111, no. 43, pp. 15304–15309, 2014.

[24] V. Sharma, S. Shivalingaiah, Y. Peng, D. Euhus, Z. Gryczynski, and H. Liu, "Autofluorescence lifetime and light reflectance spectroscopy for breast cancer diagnosis : potential tools for intraoperative margin detection," *Biomedical Optics Express*, vol. 3, no. 8, pp. 221–228, 2012.

[25] H. Tu, Y. Liu, D. Turchinovich, M. Marjanovic, J. Lyngsø, J. Lægsgaard, E. J. Chaney, Y. Zhao, S. You, W. L. Wilson, B. Xu, M. Dantus, and S. A. Boppart, "Stain-free histopathology by programmable supercontinuum pulses," *Nature Photonics*, vol. 10, no. 8, pp. 534–540, 2016.

[26] D. S. Gareau, Y. Li, B. Huang, Z. Eastman, K. S. Nehal, and M. Rajadhyaksha, "Confocal mosaicing microscopy in Mohs skin excisions: feasibility of rapid surgical pathology," *Journal of Biomedical Optics*, vol. 13, no. 5, pp. 1–21, 2009.

[27] S. Abeytunge, Y. Li, B. Larson, R. Toledo-crow, and M. Rajadhyaksha, "Rapid confocal imaging of large areas of excised tissue with strip mosaicing," *Journal of Biomedical Optics*, vol. 16, no. 5, pp. 050504–1–3, 2011.

[28] S. Abeytunge, Y. Li, B. Larson, G. Peterson, Emily Seltzer, R. Toledo-crow, and M. Rajadhyaksha, "Confocal microscopy with strip mosaicing for rapid imaging over large areas of excised tissue," *Journal of Biomedical Optics*, vol. 8, no. 6, pp. 061227–1–13, 2013.

[29] J. L. Cutter, N. T. Cohen, J. Wang, A. E. Sloan, A. R. Cohen, A. Panneerselvam, M. Schluchter, G. Blum, M. Bogyo, and J. P. Basilion, "Topical Application of Activity-based Probes for Visualization of Brain Tumor Tissue," *PLoS ONE*, vol. 7, no. 3, p. e33060, 2012.

[30] M. Snuderl, D. Wirth, S. A. Sheth, S. K. Bourne, C.-s. Kwon, M. Ancukiewicz, W. T. Curry, M. P. Frosch, and A. N. Yaroslavsky, "Dye-Enhanced Multimodal

Confocal Imaging as a Novel Approach to Intraoperative Diagnosis of Brain Tumors," *Brain Pathology*, vol. 23, pp. 73–81, 2013.

[31] D. Wang, Y. Chen, S. Y. Leigh, H. Haeberle, C. H. Contag, and J. T. C. Liu, "Microscopic Delineation of Medulloblastoma Margins in a Transgenic Mouse Model Using a Topically Applied VEGFR-1 Probe1," *Translational Oncology*, vol. 5, no. 6, pp. 408–414, 2012.

[32] D. Wirth, M. Snuderl, S. Sheth, C.-s. Kwon, M. P. Frosch, W. Curry, and A. N. Yaroslavsky, "Identifying brain neoplasms using dye- enhanced multimodal confocal imaging," *Journal of Biomedical Optics*, vol. 17, no. 2, p. 026012, 2012.

[33] W. Denk, J. H. Strickler, and W. W. Webb, "Two-Photon Laser Scanning Fluorescence Microscopy," *Science*, vol. 248, pp. 73–76, 1990.

[34] F. Helmchen and W. Denk, "Deep tissue two-photon microscopy," *Nature Methods*, vol. 2, no. 12, pp. 932–940, 2005.

[35] W. R. Zipfel, R. M. Williams, and W. W. Webb, "Nonlinear magic : multiphoton microscopy in the biosciences," *Nature biotechnology*, vol. 21, no. 11, pp. 1369–1377, 2003.

[36] D. M. Mcclatchy, V. Krishnaswamy, S. C. Kanick, J. T. Elliott, W. A. Wells, R. J. Barth, K. D. Paulsen, and B. W. Pogue, "Molecular dyes used for surgical specimen margin orientation allow for intraoperative optical assessment during breast conserving surgery," *Journal of biomedical optics*, vol. 20, no. 4, pp. 040504–1–3, 2015.

[37] D. M. Mcclatchy, B. W. Maloney, E. J. Rizzo, K. D. Paulsen, W. A. Wells, and B. W. Pogue, "Spatial and Spectral Analysis of in-Situ Tumor-Normal Interfaces in Freshly Resected Lumpectomy Slices using Multispectral Structured Light Imaging," in *Biophotonics Congress: Biomedical Optics Congress 2018 (Microscopy/-Translational/Brain/OTS)*, (Washington, D.C.), p. CTu4B.3, OSA, apr 2018.

[38] T. C. Schlichenmeyer, M. Wang, K. N. Elfer, and J. Quincy Brown, "Video-rate structured illumination microscopy for high-throughput imaging of large tissue areas," *Biomedical Optics Express*, vol. 5, no. 2, 2014.

[39] M. Wang, D. B. Tulman, A. B. Sholl, H. Z. Kimbrell, S. H. Mandava, K. N. Elfer, S. Luethy, M. M. Maddox, W. Lai, B. R. Lee, and J. Q. Brown, "Gigapixel surface imaging of radical prostatectomy specimens for comprehensive detection of cancer-positive surgical margins using structured illumination microscopy," *Scientific Reports*, vol. 6, p. 27419, jul 2016.

[40] F. Fereidouni, Z. T. Harmany, M. Tian, A. Todd, J. A. Kintner, J. D. McPherson, A. D. Borowsky, J. Bishop, M. Lechpammer, S. G. Demos, and R. Levenson, "Microscopy with ultraviolet surface excitation for rapid slide-free histology," *Nature Biomedical Engineering*, vol. 1, pp. 957–966, 2017.

[41] T. Yoshitake, M. G. Giacomelli, L. M. Quintana, H. Vardeh, L. C. Cahill, B. E. Faulkner-Jones, J. L. Connolly, D. Do, and J. G. Fujimoto, "Rapid histopathological imaging of skin and breast cancer surgical specimens using immersion microscopy with ultraviolet surface excitation," *Scientific Reports*, vol. 8, no. 1, pp. 1–12, 2018.

[42] J. Mertz, "Optical sectioning microscopy with planar or structured illumination," *Nature Methods*, vol. 8, pp. 811–819, oct 2011.

[43] J. Jonkman and C. M. Brown, "Any Way You Slice It—A Comparison of Confocal Microscopy Techniques," *Journal of Biomolecular Techniques : JBT*, vol. 26, pp. jbt.15–2602–003, jul 2015.

[44] J. Huisken, J. Swoger, F. Del Bene, J. Wittbrodt, and E. H. K. Stelzer, "Optical sectioning deep inside live embryos by selective plane illumination microscopy.," *Science*, vol. 305, pp. 1007–9, aug 2004.

[45] A. K. Glaser, Y. Wang, and J. T. C. Liu, "Assessing the imaging performance of light sheet microscopies in highly scattering tissues," *Biomedical Optics Express*, vol. 7, no. 2, 2016.

[46] A. K. Glaser, N. P. Reder, Y. Chen, E. F. Mccarty, C. Yin, L. Wei, Y. Wang, L. D. True, and J. T. C. Liu, "Light-sheet microsopy for slide-free non-destructive pathology of large clinical specimens," *Nature Biomedical Engineering*, vol. 1, pp. 1–10, 2017.

[47] S. Hu, K. Maslov, and L. V. Wang, "Second-generation optical-resolution photoacoustic microscopy with improved sensitivity and speed," *Optics Letters*, vol. 36, p. 1134, apr 2011.

[48] S. Hu and L. V. Wang, "Optical-Resolution Photoacoustic Microscopy: Auscultation of Biological Systems at the Cellular Level," *Biophysical Journal*, vol. 105, pp. 841–847, 2013.

[49] J. Yao, L. Wang, J.-M. Yang, K. I. Maslov, T. T. W. Wong, L. Li, C.-H. Huang, J. Zou, and L. V. Wang, "High-speed label-free functional photoacoustic microscopy of mouse brain in action," *Nature Methods*, vol. 12, no. 5, 2015.

[50] T. T. W. Wong, R. Zhang, P. Hai, C. Zhang, M. A. Pleitez, R. L. Aft, D. V. Novack, and L. V. Wang, "Fast label-free multilayered histology-like imaging of human breast cancer by photoacoustic microscopy," *Science Advances*, vol. 3, p. e1602168, 2017.

[51] W. M. Allen, L. Chin, P. Wijesinghe, R. W. Kirk, B. Latham, D. D. Sampson, C. M. Saunders, and B. F. Kennedy, "Wide-field optical coherence micro- elastography for intraoperative assessment of human breast cancer margins," *Biomedical optics express*, vol. 7, no. 10, pp. 4139–4153, 2016.

[52] A. M. Zysk and S. A. Boppart, "Computational methods for analysis of human breast tumor tissue in optical coherence tomography images," *Journal of Biomedical Optics*, vol. 11, no. 5, p. 054015, 2006.

[53] O. Assayag, M. Antoine, B. Sigal-Zafrani, M. Riben, F. Harms, A. Burcheri, K. Grieve, E. Dalmier, B. L. C. de Poly, and C. Boccara, "Large Field , High Resolution Full-Field Optical Coherence Tomography : A Pre-clinical Study of Human Breast Tissue and Cancer Assessment," *Technology in Cancer Research and Treatment*, vol. 13, no. 5, pp. 455–468, 2014.

[54] F. T. Nguyen, A. M. Zysk, E. J. Chaney, J. G. Kotynek, J. Uretz, F. J. Bellafiore, K. M. Rowland, P. A. Johnson, and S. A. Boppart, "Intraoperative evaluation of breast tumor margins with optical coherence tomography," *Cancer Research*, vol. 69, no. 22, pp. 8790–8796, 2009.

[55] P.-L. Hsiung, D. R. Phatak, Y. Chen, A. D. Aguirre, J. G. Fujimoto, and J. L. Connolly, "Benign and Malignant Lesions in the Human Breast Depicted with Ultrahigh Resolution and Three-dimensional Optical Coherence Tomography," *Radiology*, vol. 244, pp. 865–874, sep 2007.

[56] M. D. Keller, E. Vargis, N. D. M. Granja, R. H. Wilson, M.-a. Mycek, M. C. Kelley, and A. Mahadevan-jansen, "Development of a spatially offset Raman spectroscopy probe for breast tumor surgical margin evaluation," *Journal of Biomedical Optics*, vol. 16, no. 7, pp. 077006–1–8, 2011.

[57] S. You, H. Tu, Y. Zhao, Y. Liu, E. J. Chaney, M. Marjanovic, and S. A. Boppart, "Raman Spectroscopic Analysis Reveals Abnormal Fatty Acid Composition in Tumor Micro- and Macroenvironments in Human Breast and Rat Mammary Cancer," *Scientific Reports*, vol. 6, p. 32922, dec 2016.

[58] C. Liu, Y. Zhou, Y. Sun, J. Li, L. Zhou, S. Boydston-White, V. Masilamani, K. Zhu, Y. Pu, and R. R. Alfano, "Resonance Raman and Raman Spectroscopy for Breast Cancer Detection," *Technology in Cancer Research and Treatment*, vol. 12, no. 4, pp. 371–382, 2013.

[59] J. Q. Brown, T. M. Bydlon, S. A. Kennedy, M. L. Caldwell, J. E. Gallagher, M. Junker, L. G. Wilke, W. T. Barry, and J. Geradts, "Optical Spectral Surveillance of Breast Tissue Landscapes for Detection of Residual Disease in Breast Tumor Margins," *PloS one*, vol. 8, no. 7, pp. 8–12, 2013.

[60] L. G. Wilke, J. Q. Brown, T. M. Bydlon, S. A. Kennedy, L. M. Richards, M. K. Junker, J. Gallagher, W. T. Barry, J. Geradts, and N. Ramanujam, "Rapid noninvasive optical imaging of tissue composition in breast tumor margins," *The American Journal of Surgery*, vol. 198, pp. 566–574, oct 2009.

[61] T. M. Bydlon, W. T. Barry, S. A. Kennedy, J. Q. Brown, J. E. Gallagher, L. G. Wilke, J. Geradts, and N. Ramanujam, "Advancing optical imaging for breast margin assessment: an analysis of excisional time, cautery, and patent blue dye on underlying sources of contrast.," *PloS one*, vol. 7, p. e51418, jan 2012.

[62] K. Kong, C. J. Rowlands, S. Varma, W. Perkins, I. H. Leach, A. A. Koloydenko, H. C. Williams, and I. Notingher, "Diagnosis of tumors during tissue-conserving

surgery with integrated auto fl uorescence and Raman scattering microscopy," *PNAS*, vol. 110, no. 38, pp. 15189–15194, 2013.

[63] G. Thomas, T. Nguyen, I. J. Pence, B. Caldwell, M. E. O. Connor, and J. Giltnane, "Evaluating feasibility of an automated 3-dimensional scanner using Raman spectroscopy for intraoperative breast margin assessment," *Scientific Reports*, vol. 7, pp. 1–14, 2017.

[64] F. S. Collins and H. Varmus, "A new initiative on precision medicine," *New England Journal of Medicine*, vol. 372, no. 9, pp. 793–795, 2015.

[65] N. Sadeghipour, S. C. Davis, and K. M. Tichauer, "Generalized paired-agent kinetic model for in vivo quantification of cancer cell-surface receptors under receptor saturation conditions," *Physics in Medicine and Biology*, vol. 62, pp. 394–414, 2017.

[66] R. Weissleder, B. D. Ross, A. Rehemtulla, and S. S. Gambhir, *Molecular imaging: principles and practice*. People's Medical Publishing House, 2010.

[67] A. Marusyk and K. Polyak, "Tumor heterogeneity: causes and consequences," *Biochimica et biophysica acta*, vol. 1805, pp. 105–117, 2010.

[68] D. Zardavas, A. Irrthum, C. Swanton, and M. Piccart, "Clinical management of breast cancer heterogeneity," *Nat Rev Clin Oncol*, vol. 12, no. 7, pp. 381–394, 2015.

[69] S. Harmsen, R. Huang, M. A. Wall, H. Karabeber, J. M. Samii, M. Spaliviero, J. R. White, S. Monette, R. O. Connor, K. L. Pitter, S. A. Sastra, M. Saborowski, E. C. Holland, S. Singer, K. P. Olive, S. W. Lowe, R. G. Blasberg, and M. F. Kircher, "Surface-enhanced resonance Raman scattering nanostars for high-precision cancer imaging," *Cancer Imaging*, vol. 7, no. 271, pp. 1–12, 2015.

[70] A. Hellebust and R. Richards-Kortum, "Advances in molecular imaging: targeted optical contrast agents for cancer diagnostics," *Nanomedicine*, vol. 7, no. 3, pp. 429–445, 2012.

[71] E. A. Rodriguez, R. E. Campbell, J. Y. Lin, M. Z. Lin, A. Miyawaki, A. E. Palmer, X. Shu, J. Zhang, and R. Y. Tsien, "The Growing and Glowing Toolbox

of Fluorescent and Photoactive Proteins," *Trends in Biochemical Sciences*, vol. 42, no. 2, pp. 111–129, 2017.

[72] Y. Wang, B. Yan, and L. Chen, "SERS tags: novel optical nanoprobes for bioanalysis.," *Chemical reviews*, vol. 113, pp. 1391–428, mar 2013.

[73] S. Zhu, Q. Yang, A. L. Antaris, J. Yue, Z. Ma, H. Wang, W. Huang, H. Wan, J. Wang, S. Diao, B. Zhang, X. Li, Y. Zhong, K. Yu, G. Hong, J. Luo, Y. Liang, and H. Dai, "Molecular imaging of biological systems with a clickable dye in the broad 800- to 1 , 700-nm near-infrared window," *PNAS*, pp. 1–6, 2017.

[74] V. Ntziachristos, "Going deeper than microscopy : the optical imaging frontier in biology," *Nature Methods*, vol. 7, pp. 603–614, 2010.

[75] K. C. Weng, C. O. Noble, B. Papahadjopoulos-sternberg, F. F. Chen, D. C. Drummond, D. B. Kirpotin, D. Wang, Y. K. Hom, B. Hann, and J. W. Park, "Targeted Tumor Cell Internalization and Imaging of Multifunctional Quantum Dot-Conjugated Immunoliposomes in Vitro and in Vivo," *Nano Letters*, vol. 8, no. 9, pp. 2851–2857, 2008.

[76] B. M. V. Yezhelyev, A. Al-hajj, C. Morris, A. I. Marcus, T. Liu, M. Lewis, C. Cohen, P. Zrazhevskiy, J. W. Simons, A. Rogatko, S. Nie, X. Gao, and R. M. O. Regan, "In Situ Molecular Profiling of Breast Cancer Biomarkers with Multicolor Quantum Dots," *Advanced Materials*, vol. 19, pp. 3146–3151, 2007.

[77] D. M. McClatchy, V. Krishnaswamy, S. C. Kanick, J. T. Elliott, W. A. Wells, R. J. Barth, K. D. Paulsen, and B. W. Pogue, "Molecular dyes used for surgical specimen margin orientation allow for intraoperative optical assessment during breast conserving surgery," *Journal of Biomedical Optics*, vol. 20, no. 4, p. 040504, 2015.

[78] S. E. Bohndiek, A. Wagadarikar, C. L. Zavaleta, D. V. D. Sompel, E. Garai, J. V. Jokerst, S. Yazdanfar, and S. S. Gambhir, "A small animal Raman instrument for rapid , wide-area , spectroscopic imaging," *PNAS*, vol. 110, no. 30, pp. 12408–12413, 2013.

[79] C. L. Zavaleta, E. Garai, J. T. C. Liu, S. Sensarn, M. J. Mandella, D. Van de Sompel, S. Friedland, J. Van Dam, C. H. Contag, and S. S. Gambhir, "A Raman-based endoscopic strategy for multiplexed molecular imaging.," *Proceedings of the*

National Academy of Sciences of the United States of America, vol. 110, pp. E2288–97, jun 2013.

[80] L. Fabris, "SERS Tags : The Next Promising Tool for Personalized Cancer Detection ?," *ChemNanoMat*, vol. 2, pp. 249–258, 2016.

[81] J. V. Jokerst and S. S. Gambhir, "Molecular Imaging with Theranostic Nanoparticles," *Accounts of Chemical Research*, vol. 44, no. 10, pp. 1050–1060, 2011.

[82] J. V. Jokerst, T. Lobovkina, R. N. Zare, and S. S. Gambhir, "Nanoparticle PEGylation for imaging and therapy," *Nanomedicine*, vol. 6, no. 4, pp. 715–728, 2011.

[83] Y. W. Wang, J. D. Doerksen, S. Kang, D. Walsh, Q. Yang, D. Hong, and J. T. C. Liu, "Multiplexed Molecular Imaging of Fresh Tissue Surfaces Enabled by Convection-Enhanced Topical Staining with SERS-Coded Nanoparticles," *Small*, vol. 12, no. 40, pp. 5612–5621, 2016.

[84] Y. W. Wang, S. Kang, A. Khan, P. Q. Bao, and J. T. C. Liu, "In vivo multiplexed molecular imaging of esophageal cancer via spectral endoscopy of topically applied SERS nanoparticles," *Biomedical optics express*, vol. 6, no. 10, pp. 3714–23, 2015.

[85] Y. Wang, S. Kang, A. Khan, G. Ruttner, S. Y. Leigh, M. Murray, S. Abeytunge, G. Peterson, M. Rajadhyaksha, S. Dintzis, S. Javid, and J. T. Liu, "Quantitative molecular phenotyping with topically applied SERS nanoparticles for intraoperative guidance of breast cancer lumpectomy," *Scientific Reports*, vol. 6, no. February, p. 21242, 2016.

[86] Y. Wang, S. Kang, J. D. Doerksen, A. K. Glaser, and J. T. C. Liu, "Surgical guidance via multiplexed molecular imaging of fresh tissues labeed with SERS-coded nanoparticles," *IEEE Journal of quantum electronics*, vol. 22, no. 4, 2016.

[87] J. T. C. Liu, M. W. Helms, M. J. Mandella, J. M. Crawford, G. S. Kino, and C. H. Contag, "Quantifying cell-surface biomarker expression in thick tissues with ratiometric three-dimensional microscopy," *Biophysical Journal*, vol. 96, no. 6, pp. 2405–2414, 2009.

[88] P. Z. McVeigh, R. J. Mallia, I. Veilleux, and B. C. Wilson, "Widefield quantitative multiplex surface enhanced Raman scattering imaging in vivo.," *Journal of biomedical optics*, vol. 18, no. 4, p. 046011, 2013.

[89] A. Oseledchyk, C. Andreou, M. A. Wall, and M. F. Kircher, "Folate-targeted surface-enhanced resonance Raman scattering nanoprobe ratiometry for detection of microscopic ovarian cancer," *ACS Nano*, vol. 11, pp. 1488–1497, 2017.

[90] K. M. Tichauer, K. S. Samkoe, J. R. Gunn, S. C. Kanick, P. J. Hoopes, R. J. Barth, P. a. Kaufman, T. Hasan, and B. W. Pogue, "Microscopic lymph node tumor burden quantified by macroscopic dual-tracer molecular imaging," *Nature Medicine*, vol. 20, oct 2014.

[91] K. M. Tichauer, Y. Wang, B. W. Pogue, and J. T. C. Liu, "Quantitative in vivo cell-surface receptor imaging in oncology: kinetic modeling and paired-agent principles from nuclear medicine and optical imaging," *Physics in Medicine and Biology*, vol. 60, no. 14, pp. R239–R269, 2015.

[92] Y. W. Wang, A. Khan, S. Y. Leigh, D. Wang, Y. Chen, D. Meza, and J. T. C. Liu, "Comprehensive spectral endoscopy of topically applied SERS nanoparticles in the rat esophagus.," *Biomedical optics express*, vol. 5, pp. 2883–95, sep 2014.

[93] Y. W. Wang, A. Khan, M. Som, D. Wang, Y. Chen, S. Y. Leigh, D. Meza, P. Z. McVeigh, B. C. Wilson, and J. T. C. Liu, "Rapid ratiometric biomarker detection with topically applied SERS nanoparticles.," *Technology*, vol. 2, pp. 118–132, jun 2014.

[94] M. Fleischmann, P. J. Hendra, and A. J. McQuillan, "Raman spectra of pyridine adsorbed at a silver electrode," *Chemical Physics Letters*, vol. 26, no. 2, pp. 163–166, 1974.

[95] B. Sharma, R. R. Frontiera, A. I. Henry, E. Ringe, and R. P. V. Duyne, "SERS : Materials , applications , and the future Surface enhanced Raman spectroscopy (SERS) is a powerful vibrational," *Materials Today*, vol. 15, no. 1-2, pp. 16–25, 2012.

[96] Y. C. Cao, R. Jin, J.-m. Nam, C. S. Thaxton, and C. A. Mirkin, "Raman Dye-Labeled Nanoparticle Probes for Proteins," *Journal of the American Chemical Society*, vol. 125, pp. 14676–14677, 2003.

[97] Y. C. Cao, R. Jin, and C. A. Mirkin, "Nanoparticles with Raman Spectroscopic Fingerprints for DNA and RNA Detection," *Science*, vol. 297, pp. 1536–1541, 2002.

[98] D. Graham, B. J. Mallinder, and W. E. Smith, "Detection and Identification of Labeled DNA by Surface Enhanced Resonance Raman Scattering," *Biopolymers*, vol. 57, pp. 85–91, 1999.

[99] D. S. Grubisha, R. J. Lipert, H.-y. Park, J. Driskell, and M. D. Porter, "Femtomolar Detection of Prostate-Specific Antigen : An Immunoassay Based on Surface-Enhanced Raman Scattering and Immunogold Labels," *Analytical Chemistry*, vol. 75, pp. 5936–5943, 2003.

[100] B. Küstner, M. Gellner, M. Schütz, F. Schöppler, A. Marx, P. Ströbel, P. Adam, C. Schmuck, and S. Schlücker, "SERS Labels for Red Laser Excitation: Silica-Encapsulated SAMs on Tunable Gold/Silver Nanoshells," *Angewandte Chemie*, vol. 48, pp. 1950–1953, 2009.

[101] J. Ni, R. J. Lipert, G. B. Dawson, and M. D. Porter, "Immunoassay Readout Method Using Extrinsic Raman Labels Adsorbed on Immunogold Colloids," *Analytical Chemistry*, vol. 71, pp. 4903–4908, 1999.

[102] X. Su, J. Zhang, L. Sun, T.-w. Koo, S. Chan, N. Sundararajan, M. Yamakawa, and A. A. Berlin, "Composite Organic-Inorganic Nanoparticles (COINs) with Chemically Encoded Optical Signatures," *Nano Letters*, vol. 5, no. 1, pp. 1–6, 2005.

[103] B. C. Wang, Y. Chen, T. Wang, Z. Ma, and Z. Su, "Monodispersed Gold Nanorod-Embedded Silica Particles as Novel Raman Labels for Biosensing," *Advanced Functional Materials*, vol. 18, pp. 355–361, 2008.

[104] J. Jokerst, A. J. Cole, D. Van de Sompel, and S. S. Gambhir, "Gold nanorods for ovarian cancer detection with photoacoustic imaging and resection guidance via Raman imaging in living mice," *ACS Nano*, vol. 6, no. 11, pp. 10366–10377, 2012.

[105] X. Qian, X. H. Peng, D. O. Ansari, Q. Y. Goen, G. Z. Chen, D. M. Shin, L. Yang, A. N. Young, M. D. Wang, and S. Nie, "In vivo tumor targeting and spectroscopic detection with surface-enhanced Raman nanoparticle tags.," *Nature biotechnology*, vol. 26, pp. 83–90, jan 2008.

[106] E. Garai, S. Sensarn, C. L. Zavaleta, D. Van de Sompel, N. O. Loewke, M. J. Mandella, S. S. Gambhir, and C. H. Contag, "High-sensitivity, real-time, ratiometric imaging of surface-enhanced Raman scattering nanoparticles with a clinically translatable Raman endoscope device.," *Journal of biomedical optics*, vol. 18, p. 096008, sep 2013.

[107] L. Sinha, Y. Wang, C. Yang, A. Khan, J. G. Brankov, J. T. C. Liu, and K. M. Tichauer, "Quantification of the binding potential of cell-surface receptors in fresh excised specimens via dual-probe modeling of SERS nanoparticles," *Scientific Reports*, vol. 5, pp. 1–8, 2014.

[108] C. L. Zavaleta, K. B. Hartman, Z. Miao, M. L. James, P. Kempen, A. S. Thakor, C. H. Nielsen, R. Sinclair, Z. Cheng, and S. S. Gambhir, "Preclinical evaluation of Raman nanoparticle biodistribution for their potential use in clinical endoscopy imaging.," *Small (Weinheim an der Bergstrasse, Germany)*, vol. 7, pp. 2232–40, aug 2011.

[109] A. M. Mohs, M. C. Mancini, S. Singhal, J. M. Provenzale, B. Leyland-Jones, M. D. Wang, and S. Nie, "Hand-held spectroscopic device for in vivo and intraoperative tumor detection: Contrast enhancement, detection sensitivity, and tissue penetration," *Analytical Chemistry*, vol. 82, no. 21, pp. 9058–9065, 2010.

[110] S. Kang, Y. Wang, N. P. Reder, and J. T. C. Liu, "Multiplexed molecular imaging of biomarker-targeted SERS nanoparticles on fresh tissue specimens with channel-compressed spectrometry," *PLoS ONE*, vol. 11, no. 9, pp. 1–13, 2016.

[111] Andor, "Newton CCD," 2009.

[112] L. Mather, "Linear array PMT modules by Hamamatsu," 2011.

[113] F. Sensor, "First Sensor APD Array Data Sheet," 2002.

[114] C. L. Zavaleta, B. R. Smith, I. Walton, W. Doering, G. Davis, B. Shojaei, M. J. Natan, and S. S. Gambhir, "Multiplexed imaging of surface enhanced Raman scattering nanotags in living mice using noninvasive Raman spectroscopy.," *Proceedings of the National Academy of Sciences of the United States of America*, vol. 106, pp. 13511–6, aug 2009.

[115] K. Fujimori, D. G. Covell, J. E. Fletcher, and J. N. Weinstein, "A modeling analysis of monoclonal antibody percolation through tumors: a binding-site barrier.," *Journal of nuclear medicine : official publication, Society of Nuclear Medicine*, vol. 31, no. 7, pp. 1191–1198, 1990.

[116] T. T. Goodman, J. Chen, K. Matveev, and S. H. Pun, "Spatio-temporal modeling of nanoparticle delivery to multicellular tumor spheroids," *Biotechnol. Bioeng.*, vol. 101, no. 2, pp. 388–399, 2008.

[117] L. Miao, J. M. Newby, C. M. Lin, L. Zhang, F. Xu, W. Y. Kim, M. G. Forest, S. K. Lai, M. I. Milowsky, S. E. Wobker, and L. Huang, "The Binding Site Barrier Elicited by Tumor-Associated Fibroblasts Interferes Disposition of Nanoparticles in Stroma-Vessel Type Tumors," *ACS Nano*, vol. 10, no. 10, pp. 9243–9258, 2016.

[118] G. M. Thurber and R. Weissleder, "A systems approach for tumor pharmacokinetics," *PLoS ONE*, vol. 6, no. 9, pp. 1–10, 2011.

[119] A. L. Kholodenko and J. F. Doughlas, "Generalized Stokes-Einstein equation for spherical particle suspensions," *Physical Review E*, vol. 51, no. 2, pp. 1081–1090, 1995.

[120] T. T. Goodman, P. L. Olive, and S. H. Pun, "Increased nanoparticle penetration in collagenase- treated multicellular spheroids," *International Journal of Nanomedicine*, vol. 2, no. 2, pp. 265–274, 2007.

[121] H. Lee, H. Fonge, B. Hoang, R. M. Reilly, and C. Allen, "The Effects of Particle Size and Molecular Targeting on the Intratumoral and Subcellular Distribution of Polymeric Nanoparticles," *Molecular Pharmaceutics*, vol. 7, no. 4, pp. 1195–1208, 2010.

[122] S. D. Perrault, C. Walkey, T. Jennings, H. C. Fischer, and W. C. W. Chan, "Mediating Tumor Targeting Efficiency of Nanoparticles Through Design 2009," *Nano Letters*, vol. 9, no. 5, pp. 1909–1915, 2009.

[123] C. Wong, T. Stylianopoulos, J. Cui, J. Martin, V. P. Chauhan, W. Jiang, Z. Popović, R. K. Jain, M. G. Bawendi, and D. Fukumura, "Multistage nanoparticle delivery system for deep penetraiton into tumor tissue," *PNAS*, vol. 108, no. 6, pp. 2426–2431, 2011.

[124] J. Cheng, B. A. Teply, I. Sherifi, J. Sung, G. Luther, F. X. Gu, E. Levy-nissenbaum, A. F. Radovic-moreno, R. Langer, and O. C. Farokhzad, "Formulation of functionalized PLGA – PEG nanoparticles for in vivo targeted drug delivery," *Biomaterials*, vol. 28, pp. 869–876, 2007.

[125] Y. W. Wang, N. P. Reder, S. Kang, A. K. Glaser, Q. Yang, M. A. Wall, S. H. Javid, S. M. Dintzis, and J. T. Liu, "Raman - encoded molecular imaging (REMI) with topically applied SERS nanoparticles for intraoperative guidance of lumpectomy," *Cancer Research*, 2017.

[126] C. P. Graff and K. D. Wittrup, "Theoretical Analysis of Antibody Targeting of Tumor Spheroids: Importance of Dosage for Penetration, and Affinity for Retention," *Cancer Research*, vol. 63, pp. 1288–1296, 2003.

[127] S. Kang, Y. W. Wang, X. Xu, E. Navarro, K. M. Tichauer, and J. T. Liu, "Microscopic investigation of topically applied nanoparticles for molecular imaging of fresh tissue surfaces," *Journal of Biophotonics*, vol. 11, pp. 1–10, 2018.

[128] C. Wilhelm, F. Gazeau, J. Roger, J. N. Pons, J. Bacri, and M. Curie, "Interaction of Anionic Superparamagnetic Nanoparticles with Cells : Kinetic Analyses of Membrane Adsorption and Subsequent Internalization," *Langmuir*, vol. 18, pp. 8148–8155, 2002.

[129] H. T. Haigler, J. A. McKanna, and S. Cohen, "Direct visualization of the binding and internalization of a ferritin conjugate of epidermal growth factor in human carcinoma cells A-431," *Journal of Cell Biology*, vol. 81, pp. 382–395, 1979.

[130] P. R. St-pierre and N. Petersen, "Average Density and Size of Microclusters of Epidermal Growth Factor Receptors on A431 Cellst," *American Chemical Society*, vol. 31, no. 9, pp. 2459–2463, 1992.

[131] Y. W. Wang, Q. Yang, S. Kang, M. A. Wall, and J. T. C. Liu, "High-speed Raman-encoded molecular imaging of freshly excised tissue surfaces with topically applied SERRS nanoparticles," *Journal of Biomedical Optics*, vol. 23, pp. 1–8, apr 2018.

[132] M. Spaliviero, S. Harmsen, R. Huang, M. A. Wall, C. Andreou, J. A. Eastham, K. A. Touijer, P. T. Scardino, and M. F. Kircher, "Detection of Lymph Node Metastases with SERRS Nanoparticles," *Mol Imaging Biol*, vol. 18, no. 5, pp. 677–685, 2016.

[133] A. Nayak and T. A. Bhuiya, "Utility of cytokeratin 5/6 and high-molecular-weight keratin in evaluation of cauterized surgical margins in excised specimens of breast ductal carcinoma in situ," *Annals of Diagnostic Pathology*, vol. 15, no. 4, pp. 243–249, 2011.

[134] G. Kristiansen, K.-J. Winzer, E. Mayordomo, J. Bellach, K. Schlüns, C. Denkert, E. Dahl, C. Pilarsky, P. Altevogt, H. Guski, and M. Dietel, "CD24 expression is a new prognostic marker in breast cancer.," *Clinical cancer research : an official journal of the American Association for Cancer Research*, vol. 9, pp. 4906–13, oct 2003.

[135] R. Bhargava, W. L. Gerald, A. R. Li, Q. Pan, P. Lal, M. Ladanyi, and B. Chen, "EGFR gene amplification in breast cancer: correlation with epidermal growth factor receptor mRNA and protein expression and HER-2 status and absence of EGFR-activating mutations," *Modern Pathology*, vol. 18, pp. 1027–1033, aug 2005.

[136] R. H. Engel and V. G. Kaklamani, "HER2-positive breast cancer: current and future treatment strategies.," *Drugs*, vol. 67, no. 9, pp. 1329–41, 2007.

[137] S. McFarlane, J. A. Coulter, P. Tibbits, A. O'Grady, C. McFarlane, N. Montgomery, A. Hill, H. O. McCarthy, L. S. Young, E. W. Kay, C. M. Isacke, D. J. Waugh, S. McFarlane, J. A. Coulter, P. Tibbits, A. O'Grady, C. McFarlane, N. Montgomery, A. Hill, H. O. McCarthy, L. S. Young, E. W. Kay, C. M. Isacke, and D. J. Waugh, "CD44 increases the efficiency of distant metastasis of breast cancer," *Oncotarget*, vol. 6, pp. 11465–11476, may 2015.

[138] J. S. Nielsen, E. Jakobsen, B. Holund, K. Bertelsen, and A. Jakobsen, "Prognostic significance of p53, Her-2, and Egfr overexpression in borderline and epithelial ovarian cancer," *International Journal of Gynecological Cancer*, vol. 14, pp. 1086–1096, nov 2004.

[139] S. Paik, J. Bryant, E. Tan-Chiu, G. Yothers, C. Park, D. L. Wickerham, and N. Wolmark, "HER2 and choice of adjuvant chemotherapy for invasive breast cancer: National Surgical Adjuvant Breast and Bowel Project Protocol B-15.," *Journal of the National Cancer Institute*, vol. 92, pp. 1991–8, dec 2000.

[140] M. Murohashi, K. Hinohara, M. Kuroda, T. Isagawa, S. Tsuji, S. Kobayashi, K. Umezawa, A. Tojo, H. Aburatani, and N. Gotoh, "Gene set enrichment analysis

provides insight into novel signalling pathways in breast cancer stem cells.," *British journal of cancer*, vol. 102, pp. 206–12, jan 2010.

[141] G. Honeth, P.-O. Bendahl, M. Ringnér, L. H. Saal, S. K. Gruvberger-Saal, K. Lövgren, D. Grabau, M. Fernö, Å. Borg, and C. Hegardt, "The CD44 + /CD24 -phenotype is enriched in basal-like breast tumors," *Breast Cancer Research*, vol. 10, 2008.

[142] J. S. Desgrosellier and D. A. Cheresh, "Integrins in cancer: biological implications and therapeutic opportunities.," *Nature reviews. Cancer*, vol. 10, pp. 9–22, jan 2010.

[143] P. dos Santos, J. S. Zanetti, A. Ribeiro-Silva, and E. I. Beltrão, "Beta 1 integrin predicts survival in breast cancer: a clinicopathological and immunohistochemical study," *Diagnostic Pathology*, vol. 7, p. 104, aug 2012.

[144] B. Felding-Habermann, T. E. O'Toole, J. W. Smith, E. Fransvea, Z. M. Ruggeri, M. H. Ginsberg, P. E. Hughes, N. Pampori, S. J. Shattil, A. Saven, and B. M. Mueller, "Integrin activation controls metastasis in human breast cancer.," *Proceedings of the National Academy of Sciences of the United States of America*, vol. 98, pp. 1853–8, feb 2001.

[145] S. Ghosh, C. A. Sullivan, M. P. Zerkowski, A. M. Molinaro, D. L. Rimm, R. L. Camp, and G. G. Chung, "High levels of vascular endothelial growth factor and its receptors (VEGFR-1, VEGFR-2, neuropilin-1) are associated with worse outcome in breast cancer," *Human Pathology*, vol. 39, pp. 1835–1843, dec 2008.

[146] J. D. Schwartz, E. K. Rowinsky, H. Youssoufian, B. Pytowski, and Y. Wu, "Vascular endothelial growth factor receptor-1 in human cancer," *Cancer*, vol. 116, pp. 1027–1032, feb 2010.

[147] J.-D. Yan, Y. Liu, Z.-Y. Zhang, G.-Y. Liu, J.-H. Xu, L.-Y. Liu, and Y.-M. Hu, "Expression and prognostic significance of VEGFR-2 in breast cancer," *Pathology - Research and Practice*, vol. 211, pp. 539–543, jul 2015.

[148] I. Carvalho, F. Milanezi, A. Martins, R. M. Reis, and F. Schmitt, "Overexpression of platelet-derived growth factor receptor alpha in breast cancer is associated with tumour progression.," *Breast cancer research : BCR*, vol. 7, no. 5, pp. R788–95, 2005.

[149] S. R. Hubbard, "Juxtamembrane autoinhibition in receptor tyrosine kinases," *Nature Reviews Molecular Cell Biology*, vol. 5, pp. 464–471, jun 2004.

[150] M. T. Weigel, S. Banerjee, M. Arnedos, J. Salter, R. A'Hern, M. Dowsett, and L. A. Martin, "Enhanced expression of the PDGFR/Abl signaling pathway in aromatase inhibitor-resistant breast cancer," *Annals of Oncology*, vol. 24, pp. 126–133, jan 2013.

[151] D. W. Kufe, "MUC1-C oncoprotein as a target in breast cancer: activation of signaling pathways and therapeutic approaches," *Oncogene*, vol. 32, pp. 1073–1081, feb 2013.

[152] J. Z. Zaretsky, I. Barnea, Y. Aylon, M. Gorivodsky, D. H. Wreschner, and I. Keydar, "MUC1 gene overexpressed in breast cancer: structure and transcriptional activity of the MUC1 promoter and role of estrogen receptor alpha (ERα) in regulation of the MUC1 gene expression," *Molecular Cancer*, vol. 5, p. 57, nov 2006.

[153] W. A. Osta, Y. Chen, K. Mikhitarian, M. Mitas, M. Salem, Y. A. Hannun, D. J. Cole, and W. E. Gillanders, "EpCAM Is Overexpressed in Breast Cancer and Is a Potential Target for Breast Cancer Gene Therapy," *Cancer Research*, vol. 64, pp. 5818–5824, aug 2004.

[154] S. D. Soysal, S. Muenst, T. Barbie, T. Fleming, F. Gao, G. Spizzo, D. Oertli, C. T. Viehl, E. C. Obermann, and W. E. Gillanders, "EpCAM expression varies significantly and is differentially associated with prognosis in the luminal B HER2(+), basal-like, and HER2 intrinsic subtypes of breast cancer.," *British journal of cancer*, vol. 108, pp. 1480–7, apr 2013.

[155] J. M. Gostner, D. Fong, O. A. Wrulich, F. Lehne, M. Zitt, M. Hermann, S. Krobitsch, A. Martowicz, G. Gastl, and G. Spizzo, "Effects of EpCAM overexpression on human breast cancer cell lines," *BMC Cancer*, vol. 11, p. 45, dec 2011.

[156] E. C. Inwald, M. Klinkhammer-Schalke, F. Hofstädter, F. Zeman, M. Koller, M. Gerstenhauer, and O. Ortmann, "Ki-67 is a prognostic parameter in breast cancer patients: results of a large population-based cohort of a cancer registry.," *Breast cancer research and treatment*, vol. 139, pp. 539–52, jun 2013.

[157] N. A. Soliman and S. M. Yussif, "Ki-67 as a prognostic marker according to breast cancer molecular subtype.," *Cancer biology & medicine*, vol. 13, pp. 496–504, dec 2016.